Characterisation of an experiment for sympathetic cooling and coupling of ions in a cryogenic Penning trap

Von der Fakultät für Mathematik und Physik

der Gottfried Wilhelm Leibniz Universität Hannover

zur Erlangung des akademischen Grades

Doktor der Naturwissenschaften
- Dr. rer. nat. -

genehmigte Dissertation von

MSc Teresa Meiners

2021

1. Gutachter:	Prof. Dr. Christian Ospelkaus Institut für Quantenoptik Leibniz Universität Hannover
2. Gutachter:	Prof. Dr. Piet Oliver Schmidt Institut für Quantenoptik Leibniz Universität Hannover
3. Gutachter:	Prof. Richard Charles Thompson MA DPhil Imperial College London
Tag der Disputation:	01.06.2021

Abstract

The comparison of the g-factors of the proton and the antiproton is a stringent test of CPT invariance. The state-of-the-art method for the determination of the (anti-)proton's g-factor is the application of the continuous Stern-Gerlach effect. With this method, precisions in the low parts per billion regime could be achieved. However, preparation times for cold enough particles are on the order of minutes to hours. The implementation of sympathetic cooling using a co-trapped atomic ion could lead to preparation times in the milliseconds regime. Furthermore, the applicability of sympathetic cooling would enable an alternative readout scheme using quantum logic methods.

This thesis presents a Penning trap system that is designed for ground state cooling, adiabatic transport, and motional coupling of single $^9Be^+$ ions. It has been built in a modular manner, giving the option of adapting it for motional coupling and sympathetic cooling of single (anti-)protons.

In the course of this work, the prerequisites for motional coupling of $^9Be^+$ ions have been fulfilled: A cloud of $^9Be^+$ ions was cooled to a temperature of 1.7 mK applying Doppler cooling. The achieved temperature is about three times the Doppler limit which is 0.5 mK for beryllium ions. Furthermore, a scheme for reproducible loading of the trap and reducing the particle number was developed. Finally, first transport in our apparatus was demonstrated with clouds of beryllium ions. The method used for that is directly applicable to single ions.

The results of this work pave the way towards adiabatic transport of single $^9Be^+$ ions, which is crucial for sympathetic cooling of (anti-)protons in a double-well potential as well as for implementing quantum logic spectroscopy with single (anti-)protons.

Keywords: Penning traps, laser cooling, ion transport

Contents

Abbreviations and Acronyms

AOM	acousto-optic modulator
AR	anti-reflection
AWG	arbitrary waveform generator
BASE	Baryon Antibaryon Symmetry Experiment
CAD	Computer-Aided Design
CPT	charge-parity-time
DAC	digital-to-analog converter
DC	direct current
DDS	direct digital synthesis
EMCCD	electron-multiplying charge-coupled device
FPGA	field programmable gate array
LED	light-emitting diode
OFHC	oxygen free high conductivity
PID	proportional-integral-derivative
PMT	photon multiplier tube
ppb	parts per billion
PTB	Physikalisch-Technische Bundesanstalt
QLS	quantum logic spectroscopy
RF	radio frequency
S&H	sample and hold
SM	standard model of particle physics
TR	tuning ratio
TTL	transistor-transistor logic
UV	ultraviolet

Chapter 1 Introduction

The standard model of particle physics (SM) embodies three out of four fundamental interaction forces, namely the weak interaction, the strong interaction, and the electromagnetic interaction. However, it does not include gravitation and it cannot explain known phenomena such as dark matter and dark energy as well as the baryon asymmetry [Quint14]. Therefore, it is interesting to experimentally test the SM with the hope of discovering effects that lead to physics beyond the SM. It has been proved that the SM is invariant to the simultaneous reversal of charge, parity, and time [Lüders57]. Therefore, one way of testing the SM are tests of this charge-parity-time (CPT) invariance. Symmetry breaking was experimentally shown for C and P [Wu57], T [Lees12], and CP [Christenson64], but CPT symmetry still holds up until today. A consequence of the CPT theorem is that a particle and its antiparticle have the same mass, lifetime, charge (except for the sign), and magnetic moment (except for the sign). Therefore, comparisons of these quantities are stringent tests of CPT symmetry. In the past, substantial particle-antiparticle comparisons for testing CPT symmetry have been performed, e.g. the comparison of the electron and positron g-factors with a precision of $2 \cdot 10^{-12}$ [Van Dyck87], the comparison of the kaon and antikaon mass with a precision of $7 \cdot 10^{-4}$ [Schwingenheuer95], and the comparison of the charge-to-mass ratios of the proton and the antiproton with a precision of $1 \cdot 10^{-12}$ [Ulmer15].

A Penning trap is a well suited environment for precision measurements with charged particles such as g-factor comparisons, since a particle in a Penning trap is a well isolated system with long storage times. For example, antiprotons have been stored in a Penning trap for more than one year [Sellner17]. The most precise g-factor comparison of electrons and positrons was performed in a Penning trap [Van Dyck87]. The most precise measurements of the proton's and antiproton's magnetic moments in a Penning trap have been achieved within the Baryon Antibaryon Symmetry Experiment (BASE) collaboration. The proton's magnetic moment was determined with a precision of 0.3 parts per billion (ppb) [Schneider17] and the antiproton's

magnetic moment at a precision of 1.5 ppb [Smorra18]. The magnetic moment of the (anti-)proton can be expressed by

$$\mu_{\bar{p}/p} = \frac{g}{2}\mu_N, \tag{1.1}$$

where g is the g-factor and μ_N the nuclear magneton. In a Penning trap, the g-factor can be determined from the relation

$$g = 2\frac{\nu_L}{\nu_c}, \tag{1.2}$$

where ν_L is the Larmor frequency and ν_c the free cyclotron frequency of the particle. The free cyclotron frequency can be determined by measuring the trap frequencies. A common method for that is the detection of the image current induced in the trap electrodes by the particle, using an LC circuit [Wineland73]. The determination of the Larmor frequency, which is the spin precession frequency around the magnetic field axis, is more sophisticated. The state-of-the-art method is the application of the continuous Stern-Gerlach effect as proposed by [Dehmelt73]. A magnetic bottle is implemented in the trap, often realised by a ferromagnetic ring, that couples to the particle's spin resulting in a measurable change of the axial trap frequency [Dehmelt86].

These methods have enabled seminal achievements in the experimental determination of g-factors. However, the continuous Stern-Gerlach effect is delicate: changes of the axial trap frequency on the order of those induced by flipping the spin of the (anti-)proton can also be induced by a change of the motional energy in the modified cyclotron or magnetron mode. In the BASE experiment at Mainz, which is dedicated to proton g-factor measurements, flipping the proton's spin causes a shift of the axial trap frequency of 172 mHz [Schneider17], whereas a change of the modified cyclotron state by one quantum of motion already causes a frequency shift of 70 mHz [Quint14]. With decreasing temperature of the modified cyclotron mode, these energy changes of the modified cyclotron mode become less probable since they scale with the motional quantum number of the modified cyclotron motion [Ulmer14]. Therefore, it is crucial to prepare the (anti-)proton in a motional state as low as possible - for the BASE experiment in Mainz it must be below 1.7 K for the modified cyclotron mode [Smorra15a]. This is currently realised by resistive cooling and applying statistical methods [Schneider17]. With these techniques one measurement cycle has a typical duration of about 90 minutes, but several hundred repetitions are necessary to determine the Larmor frequency [Schneider17]. The application of techniques that allow faster cooling and achieve even lower temperatures are desirable.

In atomic physics, laser cooling is a common technique to reach particle temperatures in the millikelvin regime and the motional ground state within milliseconds. Ground state cooling has become a standard method in Paul traps and was reported many times, first in [Diedrich89]. In Penning traps it was shown for the first time on a single $^{40}Ca^{+}$ ion in [Goodwin16]. However, (anti-)protons do not have an electronic

structure due to the absence of electrons and are therefore not applicable to laser cooling. This issue can be handled by using sympathetic cooling. For this, an atomic ion that can be laser cooled is needed that exchanges its motional energy with the (anti-)proton. Several concepts to realise the required coupling between the ion's and the (anti-)proton's motion have been proposed and investigated: The most natural approach would be to store the particles in a **common potential well** to achieve direct coupling. This requires negatively charged particles for cooling an antiproton, especially, to avoid annihilation. However, even though there are candidates, laser cooling of anions has not become a standard method yet but is still a research field itself. So far, it was shown by spectroscopy that La^- has transitions possibly suited for laser cooling [Kellerbauer15]. Furthermore, laser-assisted cooling of Os^- was reported in [Cerchiari19]. Another approach is sympathetic cooling via a **shared endcap electrode** which is pursued in [Cornejo16] and [Bohman18]. Starting from this approach, sympathetic cooling of a proton with a cloud of $^9Be^+$ ions via an **LC circuit** was recently demonstrated [Bohman20]. A further alternative approach is the motional coupling of two particles in a **double-well potential** via Coulomb interaction as was proposed by [Wineland98]. Motional coupling using a double-well potential was already demonstrated in Paul traps by [Brown11] and [Harlander11] but has not been demonstrated in Penning traps yet. Cooling the (anti-)proton to its motional ground state would offer the additional possibility to determine the (anti-)proton's spin state using quantum logic spectroscopy following the approach of [Heinzen90]. The spin state information of the (anti-)proton is transferred to an atomic ion via a shared mode of both particles and subsequently detected via laser-ion interaction.

1.1. Experiment concept

As part of the BASE collaboration, our experiment aims for developing and implementing techniques for improving (anti-)proton g-factor measurements. For sympathetic cooling of an (anti-)proton, we pursue the approach of coupling the motional modes of the (anti-)proton and the atomic ion via the Coulomb interaction in a double-well potential. As the atomic ion for the interaction with protons, $^9Be^+$ was chosen since it is the lightest ion species for which laser cooling has been demonstrated to date. Low or no differences in mass are crucial for motional coupling in a double-well potential since the motional frequencies of both particles must be almost equal [Brown11]. For motional coupling of a positively charged ion and an antiproton, one well of the double-well potential must be inverted to maintain trapping of both particles.

The (anti-)proton's spin state information will first be transferred to the particle's motional mode and from there to the co-trapped $^9Be^+$ ion via motional coupling. Subsequently, the information from the motional mode is transferred to an electronic state that is accessible by laser radiation. This technique is called quantum logic spectroscopy (QLS) and was first demonstrated with an $^{27}Al^+$ ion as "spectroscopy"

ion and a $^9Be^+$ ion as "logic" ion [Schmidt05]. In our case the (anti-)proton is referred to as "spectroscopy" ion and the beryllium ion as "logic" ion. The motional coupling will be realised via Coulomb coupling in the double-well potential. The coupling of the motional state and the spin state can be realised by sideband coupling using a Raman process for the $^9Be^+$ ion as has been experimentally demonstrated in [Monroe95] and by implementing a static magnetic field gradient as has been theoretically shown in [Nitzschke20].

The implementation of QLS with single (anti-)protons as well as motional coupling of a $^9Be^+$ ion and an (anti-)proton involve many technical challenges. Therefore, we will tackle them step by step. Our approach is to first concentrate on beryllium and show motional coupling between two single beryllium ions, before protons are involved. For this, we have built an apparatus for production, cooling, and motional coupling of two single beryllium ions. It consists of several Penning traps where single traps can be exchanged for the implementation of proton coupling.

1.2. Outline

This thesis begins with an overview over the theoretical background of the concepts and methods of the current experiment. **Chapter 2** comprises a description of the Penning trap as well as sections on laser cooling of a beryllium ion in a Penning trap and Coulomb coupling of two beryllium ions, which are key elements for achieving the experimental goal of sympathetically cooling a single beryllium ion. **Chapter 3** describes the apparatus with a focus on the recent developments with respect to our former experimental setup [Niemann19a]. **Chapter 4** is dedicated to the imaging optics. It discusses their design and implementation. **Chapter 5** focuses on particle preparation. It guides through the steps that are taken to produce cold beryllium ions and presents the measurements that were conducted to characterise our apparatus. **Chapter 6** concentrates on adiabatic transport of single beryllium ions. It describes and discusses simulations of adiabatic transport in our trap system as well as the experimental implementation and measurement results that show evidence of transport. **Chapter 7** concludes this thesis and shows and discusses prospects and further steps that will be taken to reach the aim of sympathetically cooling a single proton and finally implementing QLS.

Chapter 2
Theoretical background

This chapter gives an overview over the theoretical background of the concepts, aims, and measurements described in the further course of this thesis. It starts with a description of the Penning trap as a basis (section 2.1) followed by section 2.2 on laser cooling of a $^9Be^+$ ion in a Penning trap, which treats Doppler cooling that was applied within the scope of this thesis (see section 5.3) as well as sideband cooling and axialisation that will be implemented in the near future (see section 7.1). Furthermore, the level scheme for a $^9Be^+$ ion at a magnetic field of 5 T with the transitions referenced in this thesis is shown. Finally, Coulomb coupling will be introduced which is the mechanism behind sympathetic cooling of single ions in a double well potential.

2.1. Penning trap

A charged particle can be confined using electromagnetic fields. However, Earnshaw's theorem states that it cannot be confined by purely electrostatic fields [Earnshaw42]. For the confinement of charged particles either a radio frequency (RF) field (Paul trap) or a magnetostatic field (Penning trap) is needed additionally to an electrostatic field.

2.1.1. Ideal Penning trap

The calculations for an ideal Penning trap can be found in many textbooks and articles e.g. in [Ghosh95]. This section gives a brief overview.

In an ideal Penning trap a quadrupolar electric field is superimposed with a homogeneous magnetic field. The electric field is produced by two endcaps and a ring electrode, as shown in figure 2.1, which are infinite hyperboloids of revolution.

The geometry obeys the equation

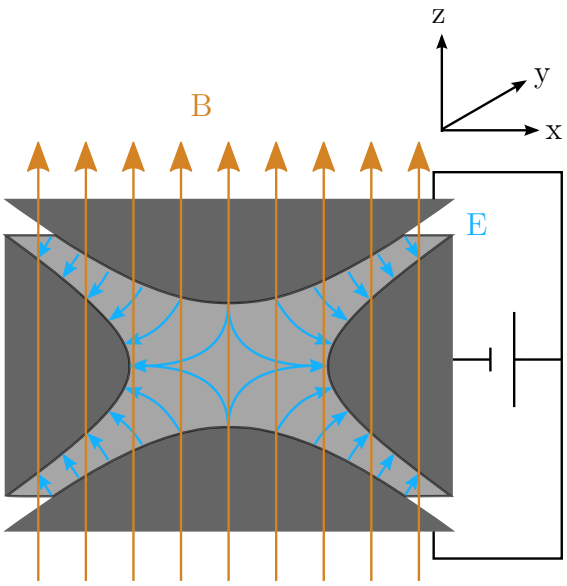

Figure 2.1: Sketch of an ideal Penning trap. Cut section view. The electric quadrupole field (blue) is produced by a hyperboloid ring and two hyperboloid endcaps. The magnetic field is shown in brown. Figure taken from [Feld15].

$$\frac{r^2}{r_0^2} - \frac{z^2}{z_0^2} = \pm 1, \tag{2.1}$$

where $r = \sqrt{x^2 + y^2}$ and z are the coordinates as indicated in figure 2.1. z_0 and r_0 indicated the distance from the trap centre to the nearest point of the endcaps and ring electrode, respectively. The endcaps exhibit a voltage difference of U with respect to the ring electrode. This leads to an electric potential of

$$\phi = \frac{U}{2z_0^2 + r_0^2}(2z^2 - x^2 - y^2). \tag{2.2}$$

The electric potential confines the particle in axial direction (along the z-axis). The voltage applied to the ring electrode must be negative with respect to the endcaps to confine positively charged particles. To confine the particle in the radial direction, the magnetic field is necessary, which is given by

$$\vec{B} = B\vec{e}_z. \tag{2.3}$$

A particle with charge q experiences the Lorentz force

$$\vec{F} = q\vec{v} \times \vec{B} - q\nabla\phi, \tag{2.4}$$

which leads to the equations of motion for a particle in an ideal Penning trap:

$$\ddot{x} = \omega_c \dot{y} + \frac{1}{2}\omega_z^2 x \tag{2.5}$$

$$\ddot{y} = -\omega_c \dot{x} + \frac{1}{2}\omega_z^2 y \tag{2.6}$$

$$\ddot{z} = -\omega_z^2 z \tag{2.7}$$

with

$$\omega_c = \frac{q}{m} B, \tag{2.8}$$

where m is the mass of the particle and ω_C the free cyclotron frequency. Choosing an exponential ansatz leads to the solutions

$$\omega_z = \sqrt{\frac{4qU}{m(2z_0^2 + r_0^2)}}, \tag{2.9}$$

$$\omega_+ = \frac{1}{2}(\omega_c + \sqrt{\omega_c^2 - 2\omega_z^2}), \tag{2.10}$$

and

$$\omega_- = \frac{1}{2}(\omega_c - \sqrt{\omega_c^2 - 2\omega_z^2}) \tag{2.11}$$

where ω_z is the axial frequency, ω_+ the modified cyclotron frequency, and ω_- the magnetron frequency.

2.1.2. Real Penning trap

The ideal Penning trap has perfectly hyperboloid electrodes of infinite extent. The potential of a real Penning trap deviates from the quadrupole potential due to the finite size of the electrodes, machining imperfections, and inhomogeneities and tilting of the magnetic field with respect to the z-axis. Ellipticities in the electric potential and a tilt of the magnetic field lead to a modification of the trap frequencies such that the relation between the free cyclotron frequency and the trap frequencies becomes

$$\omega_c^2 = \omega_+^2 + \omega_-^2 + \omega_z^2 \tag{2.12}$$

instead of

$$\omega_c = \omega_+ + \omega_- \tag{2.13}$$

as for the ideal Penning trap. Equation 2.12 is called the *invariance theorem* and has been derived by [Brown82].

Trap imperfections also lead to an energy dependence of the axial frequency due to anharmonicities. To compensate these imperfections, guard or compensation electrodes were inserted between the ring and endcaps [Van Dyck76]. These additional electrodes allow, if suitably formed, to make the trap *compensated* and *orthogonal* [Gabrielse83]. In a compensated trap anharmonicities can be tuned out by carefully adjusting the compensation voltages. The trap is orthogonal if tuning the correction voltages does not change the axial trap frequency.

2.1.3. Cylindrical Penning trap

Instead of using hyperboloid electrodes, a Penning trap can be built from cylindrical rings to allow easier machining as well as optical access [Gabrielse89]. The potential of a cylindrical Penning trap can be derived starting from Laplace's equation in cylindrical coordinates

$$\frac{\partial^2\Phi}{\partial\rho^2}+\frac{1}{\rho}\frac{\partial\Phi}{\partial\rho}+\frac{1}{\partial^2}\frac{\partial^2\Phi}{\partial\phi^2}+\frac{\partial^2\Phi}{\partial z^2}=0. \tag{2.14}$$

Its general solution is derived in textbooks on electrostatics e.g. in [Jackson99]. Below, the potential for a five-pole Penning trap consisting of five stacked ring electrodes, as shown in figure 2.2, is given. Its derivation can be found in [Ulmer11]. The potential reads

$$\begin{aligned}\Phi(\rho,z,V_i)=\frac{2}{\Lambda}\sum_{n=1}^{\infty}[&\frac{V_1\cos(k_nz_0)-V_5\cos(k_n\Lambda)}{k_n}\\&+\sum_{i=2}^{5}\frac{V_i-V_{i-1}}{k_n^2d}(\sin(k_nz_{2i})-\sin(k_nz_{2i-1}))]\\&\times\frac{I_0(k_n\rho)}{I_0(k_nr_0)}\sin(k_n(z+\frac{\Lambda}{2})),\end{aligned} \tag{2.15}$$

where $k_n=n\pi/\Lambda$ with the total trap length Λ, d is the spacing between adjacent electrodes, z_{2i} the start coordinate of the i-th electrode, z_{2i-1} the stop coordinate of the $i-1$-th electrode, and I_0 the modified Bessel function of zeroeth order. Expanding in z and normalising to the voltage applied to the ring electrode V_R, the potential becomes

$$\Phi(0,z)=V_R\sum_{j=0}^{n}C_jz^j \tag{2.16}$$

with

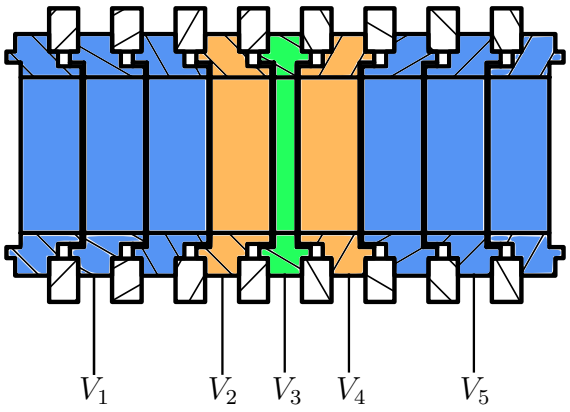

Figure 2.2: Five-pole cylindrical Penning trap. Cut section view. The ring electrode is shown in green, correction electrodes in orange, and endcaps in blue. V_i are the voltages applied to the respective electrodes. Sapphire spacers for electrically isolating the electrodes against each other are shown in white. The endcaps are divided in three electrodes, each, all held at the same potential in static operation. This is necessary for transporting the ions (see chapter 6).

$$C_j = \frac{1}{j!\Lambda V_R}\sum_{n=1}^{\infty}[\frac{V_1\cos(k_n z_0) - V_5\cos(k_n\Lambda)}{k_n} + \sum_{i=2}^{5}\frac{V_i - V_{i-1}}{k_n^2 d}(\sin(k_n z_{2i}) - \sin(k_n z_{2i-1}))] \times(\frac{n\pi}{\lambda})^j\frac{1}{I_0(k_n r_0)}\sin(\frac{\pi}{2}(n+j)). \tag{2.17}$$

The voltages are usually set as follows:

- endcaps: $V_{EC} = V_1 = V_5 = 0$
- ring electrode: $V_R = V_3$
- correction electrodes: $V_{CE} = V_2 = V_4$

The ratio V_{CE}/V_R is called tuning ratio. For the voltage settings given above, C_j can be expressed as

$$C_j = E_j + \frac{V_{CE}}{V_R}D_j, \tag{2.18}$$

where E_j and D_j are parameters given by the electrode sizes. The trap geometry can be chosen in a way that $D_2 = 0$, i.e. the trap is orthogonal, and that $C_4 = C_6 = 0$ can be obtained by chosing an adequate tuning ratio, i.e. the trap is compensated.

The axial frequency is, to lowest order, given by [Gabrielse89]

$$\omega_z = \sqrt{\frac{2qV_R}{m}C_2}. \tag{2.19}$$

2.2. Cooling a $^9Be^+$ ion in a Penning trap

There are several methods to cool a particle in a Penning trap such as buffer gas cooling, resistive cooling, and laser cooling. An overview over these methods is given in e.g. [Segal14]. This section will concentrate on laser cooling, which is the cooling method of choice in our experiment due to the capability of achieving temperatures in the sub-mK regime within short timescales on the order of seconds.

2.2.1. Doppler cooling

For laser cooling in Penning traps, two cases are distinguished: the *weak binding regime* where the natural linewidth of the cooling transition is much larger than any of the trap frequencies and the *strong binding regime* where the natural linewidth is much smaller than any of the trap frequencies [Wineland79]. In the case of weak binding, the ion can be approximated as a free particle and Doppler cooling can be applied.

For a closed transition the atom can be approximated as a two-level system. If the atom moves with velocity v in the opposite direction of a light field, it is resonant with a photon that has a freuqency of $\omega = \omega_0 + kv$, where k is the wave number of the photon. The atom absorbs the photon which leads to a velocity reduction of $\frac{\hbar k}{m}$ due to the transmission of the photon's momentum. The absorbed photon is re-emitted by spontaneous emission, which causes a momentum kick on the atom in a random direction. For hot particles this so-called *random walk* averages to zero for a large number of cycles and can therefore be neglected.

The scattering force, which is proportional to the scattering rate, is given by [Foot05]

$$F_{\text{scatt}} = \hbar k \frac{\Gamma}{2} \frac{\frac{I}{I_{\text{sat}}}}{1 + \frac{I}{I_{\text{sat}}} + \frac{4(\delta + kv)^2}{\Gamma^2}}, \tag{2.20}$$

where $\delta = \omega_0 - \omega$ is the detuning of the laser from the atomic transition, I is the intensity of the laser, and I_{sat} is the saturation intensity given by

$$I_{sat} = \frac{\pi}{3}\frac{hc}{\lambda^3 \tau} \tag{2.21}$$

with λ being the transition wavelength and τ the lifetime of the transition.

The fundamental limit that can be reached with Doppler cooling is the *Doppler cooling limit* given by

$$k_B T_D = \frac{\hbar\Gamma}{2}. \tag{2.22}$$

For beryllium, this gives a temperature of 0.5 mK. In a Penning trap, the total energy of a particle is given by [Itano82]

$$E = \frac{1}{2} m r_z^2 \omega_z^2 + m\frac{1}{2}(\omega_+ - \omega_-)(\omega_+ r_+^2 - \omega_- r_-^2). \tag{2.23}$$

It can be seen that for cooling, i.e. reducing the motional amplitudes r_i, energy must be added to cool the magnetron mode. To achieve this, the cooling beam must be displaced from the trap centre in the radial plane in such a way that the ion experiences a higher intensity when the magnetron motion is co-propagating with the cooling beam than when it is contra-propagating. For cooling the condition

$$\omega_- < \frac{(\frac{\Gamma}{2})^2 + \delta^2}{2ky_0\delta} < \omega_+ \tag{2.24}$$

must hold where a gaussian laser beam with a wavevector $k\vec{e}_x$ that is displaced by y_0 along the y-axis is assumed [Itano82].

2.2.2. Sideband cooling

In the strong-binding regime, sideband cooling can be applied to cool the ion to its motional ground state. Since in this regime, the natural linewidth of the transition is much smaller than the trap frequencies, sidebands appear at distances of $n\omega_i$ from the transition in frequency space, where n is an integer and ω_i the trap frequency of the respective mode. By exciting these sideband transitions with radiation at the frequency $\omega_0 \pm n\omega_i$, motional energy can be added or removed from the system. This is possible, since the radiation couples the ion's internal state to its motion. Assuming a two-level system in its electronic ground state: when radiation at the first red sideband is applied, the ion is excited and one quantum of motion is removed. For the first blue sideband, the ion is excited and one quantum of motion is added. The excited state then decays to the ground state on a carrier transition, i.e. leaving the motional state unaffected. This leads to a net change of the motional energy. The scheme is graphically shown in figure 2.3.

The favoured transitions for sideband cooling are not always optical transitions as e.g. for $^{40}Ca^+$ [Mavadia14]. In beryllium the qubit transition $S_{\frac{1}{2}} |m_J = -\frac{1}{2}, m_I = \frac{3}{2}\rangle \rightarrow S_{\frac{1}{2}} |m_J = \frac{1}{2}, m_I = \frac{3}{2}\rangle$ is used, which is in the microwave regime. Therefore, for driving this transition either microwaves [Ospelkaus11] or a Raman process [Monroe95] needs to be used. Using Raman transitions, the k vector difference of the two beams involved needs to have a sizeable overlap with the direction of the normal mode to be cooled. In our case, their k vector difference needs to be along the axial direction, since the axial motion shall be cooled using the

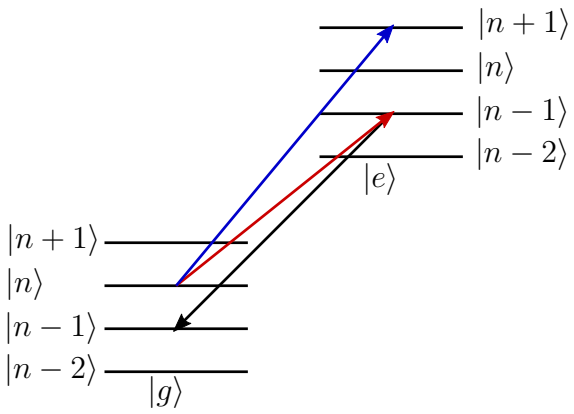

Figure 2.3: Sideband excitation. Driving a blue sideband (shown in blue) adds one quantum of motion, a red sideband (red) removes one. Decaying on a carrier transition (black) leads to a net change of the motional energy. The ground and excited state of the two-level system are denoted as $|g\rangle$ and $|e\rangle$. Motional states are depicted as $|n \pm i\rangle$.

first red sideband. For a more detailed description of sideband cooling, see e.g. [Wineland79].

2.2.3. Axialisation

Axialisation is the coupling of two modes in the Penning trap using an inhomogeneous RF field that was first suggested by [Wineland75] for detecting the radial modes via the axial mode.

For coupling the axial mode to one of the radial modes, an RF drive is applied to a two-segmented correction electrode which yields an electric field at the trap centre of [Cornell90]

$$\vec{E} = \Re(Ee^{i\Omega t})(x\vec{e}_z + z\vec{e}_x), \tag{2.25}$$

where E is a complex amplitude and $\Omega = |\omega_\pm \mp \omega_z|$ for coupling between the axial mode and the modified cyclotron mode and magnetron mode, respectively.

For coupling the modified cyclotron mode with the magnetron mode, a RF is applied to a four-segmented ring electrode which leads a quadrupolar potential and an electric field [Hrmo19]

$$\vec{E} = \frac{U}{2r_0^2}(2x\vec{e}_x + 2y\vec{e}_y)\sin(\Omega t) \tag{2.26}$$

at the trap centre. In this case $\Omega = \omega_+ + \omega_- = \omega_c$.

When axialisation is applied in the presence of laser cooling, the radius of the metastable magnetron mode can be reduced by efficient cooling of the axial or modified cyclotron mode, respectively. For coupling of the radial modes, the rate

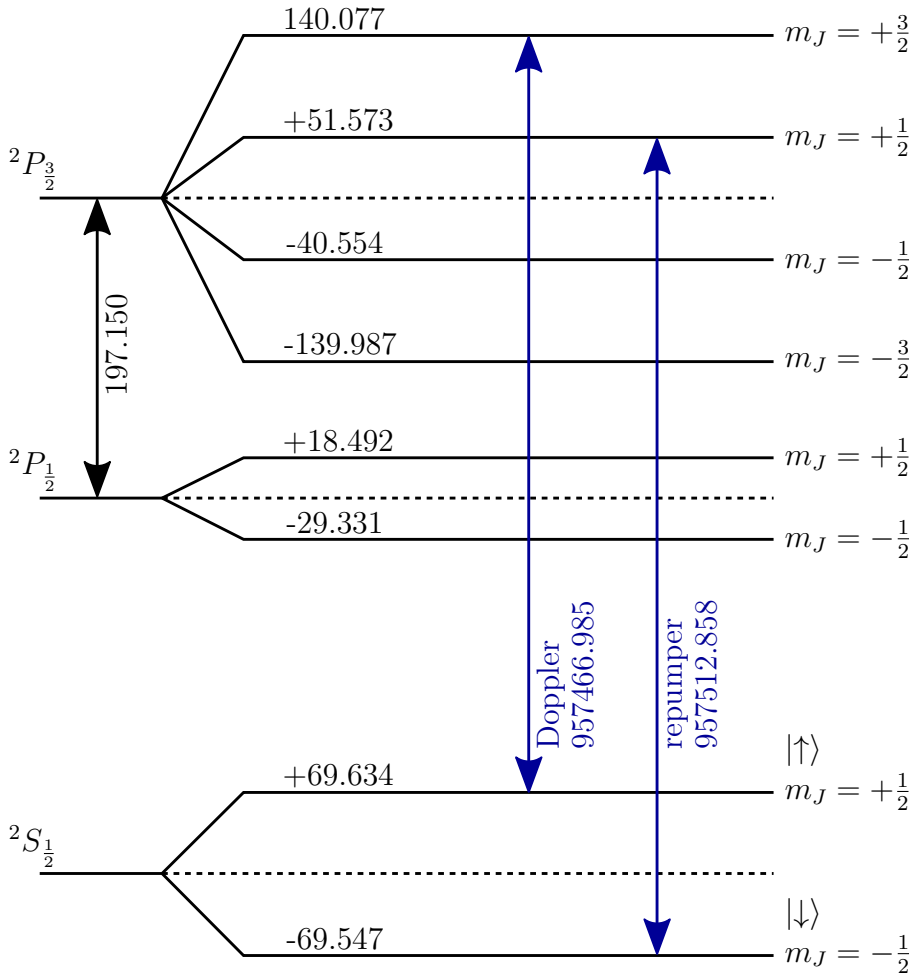

Figure 2.4: $^9Be^+$ level scheme at 4.9997 T. All splittings are given in GHz.

equations describing the radii of the modified cyclotron and magnetron modes are given by [Powell02]

$$\dot{r}_+ = \zeta r_- - \gamma_+ r_+ \tag{2.27}$$

$$\dot{r}_- = -\zeta r_+ - \gamma_- r_-, \tag{2.28}$$

where γ_+ and γ_- are the cooling rates for the modified cyclotron mode and the magnetron mode and ζ is the coupling rate due to the RF field. For $\zeta^2 > -\gamma_+\gamma_-$ the radii of the two modes shrink. If this condition is not met, the particle either stays on a stable orbit or its orbit extends until it becomes stable [Powell02].

2.2.4. $^9Be^+$ level structure

Figure 2.4 depicts the level structure of a $^9Be^+$ ion at a magnetic field of 4.9997 T. This level scheme is based on the calculations described in [Paschke17]. It was used as a starting point for the experiment and all frequencies given in this thesis are given with respect to the frequencies shown in the figure.

The $m_I = \frac{3}{2}$ manifold is used. For Doppler cooling, the closed cycle transition $S_{\frac{1}{2}} |m_J = \frac{1}{2}, m_I = \frac{3}{2}\rangle \rightarrow P_{\frac{3}{2}} |m_J = \frac{3}{2}, m_I = \frac{3}{2}\rangle$ is used. Eventually, the ion can be non-resonantly pumped into the $S_{\frac{1}{2}} |m_J = -\frac{1}{2}, m_I = \frac{3}{2}\rangle$ state. From there, it can be repumped via the transition $S_{\frac{1}{2}} |m_J = -\frac{1}{2}, m_I = \frac{3}{2}\rangle \rightarrow P_{\frac{1}{2}} |m_J = \frac{1}{2}, m_I = \frac{3}{2}\rangle$. The substates of the $S_{\frac{1}{2}}$ state are used as qubit states.

2.3. Coulomb coupling of two $^9Be^+$ ions

Motional energy can be exchanged between two ions in a double-well potential by coupling their (axial) motional modes, which allows sympathetic cooling of the shared mode. This section follows [Brown11]. The Coulomb potential of particles 1 and 2 is given by

$$\Phi(x_1, x_2) = \frac{1}{4\pi\epsilon_0} \frac{q_1 q_2}{s_0 - x_1 + x_2}, \tag{2.29}$$

where ϵ_0 is the permittivity of free space, s_0 the distance of the potential wells, q_i the charge and x_i the distance from the equilibrium position of particle i. The potential can be expanded to

$$\Phi(x_1, x_2) \approx \frac{1}{4\pi\epsilon_0} \frac{q_1 q_2}{s_0} (1 + \frac{x_1 - x_2}{s_0} + \frac{x_1^2 + x_2^2}{s_0^2} - \frac{2x_1 x_2}{s_0^2}), \tag{2.30}$$

where the last term describes the Coulomb coupling between the ions in lowest order. For small deviations of the particles from their equilibrium position, it becomes

$$\frac{1}{4\pi\epsilon_0} \frac{q_1 q_2}{s_0} \frac{2x_1 x_2}{s_0^2} \approx -\hbar\Omega_{ex}(a_1 a_2^\dagger + a_1^\dagger a_2), \tag{2.31}$$

where a_i and $a_i^\dagger$ are the lowering and raising operators of the harmonic oscillator. Ω_{ex} is the rate at which the ions exchange their motional energy and is given by

$$\Omega_{ex} = \frac{q_1 q_2}{4\pi\epsilon_0 s_0^3 \sqrt{m_1 m_2} \sqrt{\omega_1 \omega_2}}, \tag{2.32}$$

where m_i and ω_i are the mass and charge of the respective particles.

For two identical $^9Be^+$ ions at a distance of $s_0 = 1.24\,\text{mm}$ and an axial frequency of 129 kHz, the beryllium ions exchange their motional energy at a

rate of $\Omega_{ex} = 10\,\mathrm{s}^{-1}$ which leads to an exchange time of $\tau_{ex} = \frac{\pi}{2\Omega_{ex}} = 157\,\mathrm{ms}$ [Meiners18].

Chapter 3
Apparatus

This chapter describes the apparatus and infrastructure of the experiment. Figure 3.1 shows a simplified sketch of the apparatus. The heart of the experiment is the Penning trap stack (section 3.1) that is located in an inner vacuum chamber, the so-called trap can (section 3.2). This chamber is cooled to 4 K by an ultra-low vibration cryo-cooler to decrease the pressure inside the trap can. This is necessary to prevent antiprotons, which shall be used in the future, from annihilating. Thermal contact between the cryo-cooler and the trap can is given by a cylindrical support structure, the cold stage, that is located inside another cylindrical structure at 40 K to thermally isolate the system from room temperature. The cold stage is attached to a superconducting magnet in a way that the trap stack is located at the centre of the magnet's room-temperature bore. The whole structure is surrounded by an outer vacuum chamber.

The cryogenic support structure, the cryostat, and the superconducting magnet are not described in this thesis, since this has been done extensively in [Niemann19a].

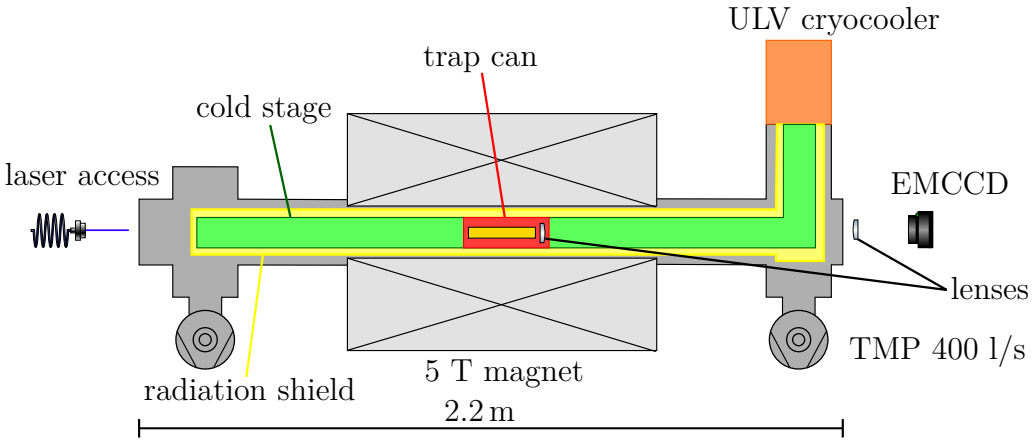

Figure 3.1: Simplified sketch of the apparatus. The trap stack is shown in yellow and the trap can in red. The support structure that is cooled by the ultra-low vibration cryocooler (orange) consists of an inner structure at 4 K (green) and an outer structure at 40 K (yellow). The outer vacuum chamber is shown in grey and the superconducting magnet in light grey. Drawing not to scale. The figure was taken from [Niemann19b].

3.1. Penning trap stack

The current Penning trap stack is an intermediate step towards the experimental goals described in section 1.1 and an extension of the setup used in [Niemann19a]. It has been designed and built for the demonstration of the following applications:

- Adiabatic transport of single $^{9}Be^{+}$ ions.
- Sympathetic cooling of a $^{9}Be^{+}$ ion with another ion of the same species via Coulomb coupling of their motional modes.
- Cooling of a $^{9}Be^{+}$ ion to its motional ground state via sideband cooling.
- Creation of protons with a self-built proton source.

All trap electrodes are made of oxygen free high conductivity (OFHC) copper plated with hard gold and a diffusion barrier of nickel. They are electrically isolated from one another by sapphire rings and sapphire balls for segmented electrodes. The trap dimensions result from a trade-off between manufacturing capabilities, feasible trap voltages, image charges and currents, as well as heating rates. For details see [Niemann19a].

The trap stack is shown in figure 3.2. The **beryllium trap** (marked in green) has an inner diameter of 9 mm and is designed for the production, preparation, and detection of single beryllium ions. Beryllium ions are produced via laser ablation

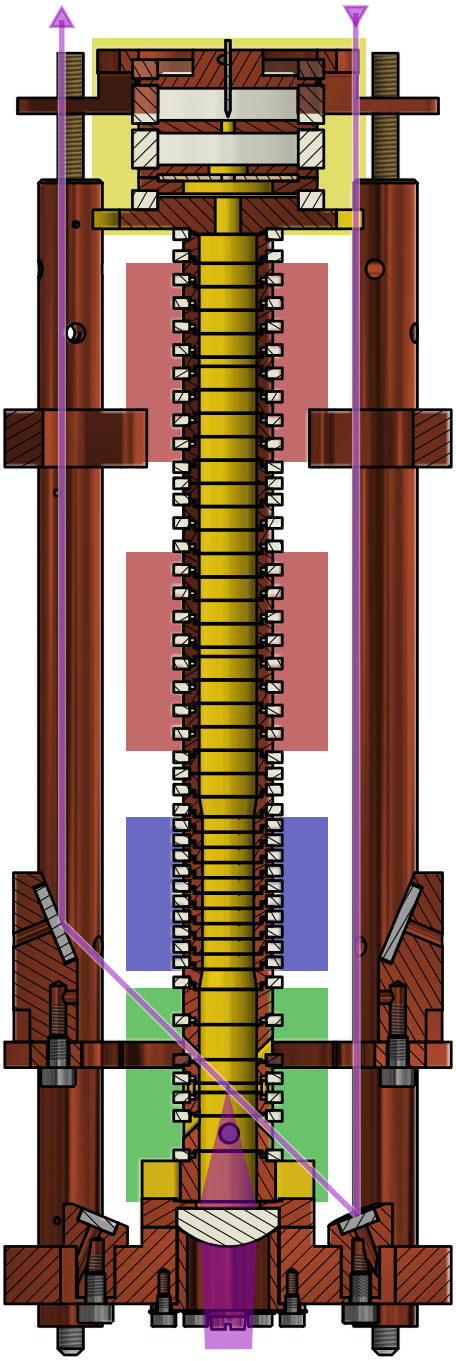

Figure 3.2: Cut view sketch of the Penning trap stack. The different colours in the background mark the different traps; yellow: proton source, red: precision traps, blue: coupling trap, green: beryllium trap. The cooling laser beam and fluorescence light are depicted in purple. A second laser beam can be sent through the trap centre perpendicularly to the depicted beam with respect to the magnetic field passing through the second pair of holes and using the second pair of mirrors. The dark purple disk in one of the endcaps is the beryllium ablation target. The ablation beam is fed into the system similarly to the cooling laser beams, but in the plane perpendicular to the paper plane.

from a solid beryllium disk implemented in one of the endcaps. The ablation light is sent into the system parallel to the trap stack onto a curved mirror that deflects the beam by 90° and focuses it through a hole in the endcap onto the beryllium target [Niemann19a]. In terms of preparation, Doppler cooling as well as sideband cooling can be implemented in the beryllium trap. For this purpose, holes with a diameter of 1.5 mm have been drilled in the endcaps that allow sending laser beams through the trap centre at an angle of 45° with respect to the magnetic field, which is oriented parallel to the trap stack. Laser beams are sent into and out of the system parallely to the trap stack. Two pairs of mirrors are attached to the stack's support structure to deflect the laser beams at an angle of 45° (*Laseroptik*, coating:*B-02250-01*) and 135° (*Edmund Optics, #45-602*), respectively. The laser beam trajectory that is used for the Doppler cooling laser is depicted in figure 3.2. A second laser beam can be sent into the system co-propagating but with a displacement of 6 mm between the beams. This second beam is then deflected by the other pair of mirrors and crosses the trap centre in the same radial direction as the first beam but counterpropagating with respect to the axial direction. This wavevector difference is necessary for the implementation of sideband cooling using Raman transitions and therefore to achieve ground-state cooling. In this trap, beryllium ions can be detected via fluorescence detection. Towards this end, a custom aspheric lens that collects the fluorescence light is attached to the trap stack (for details see section 4 and appendix A. The lens is electrically shielded from the trap with a gold mesh (*precision eforming, MG9*) clamped between two electrodes at a distance of 1 mm from the lens. The mesh has a wire line width of 61 µm and an opening width of 785 µm, which leads to a maximum transmission of 86 %. This gold mesh replaced the previous finer mesh that has led to diffraction of the fluorescence light [Niemann19a]. The ring electrode of the beryllium trap is segmented into four segments of equal size. This allows for applying an RF dipole potential for exciting the radial motion of the ion as well as an RF quadrupole potential for implementing axialisation.

The **coupling trap** (marked in blue) has an inner diameter of 8 mm. It consists of ten relatively thin electrodes with a thickness of 2.25 mm and an electrode spacing of 0.14 mm that allow creating a double-well potential, which is needed for Coulomb coupling of two beryllium ions.

Two **precision traps** (marked in red) with an inner diameter of 9 mm are implemented in the trap stack. They are compensated and orthogonal and adapted from [Schneider14]. One of the traps (the lower one in the figure) is connected to two resonators for measuring radial and axial trap frequencies, respectively, using image current detection. The resonators were built at BASE CERN. Detailed information about the design and measurement principle can be found in [Borchert17] and [Smorra15b]. The precision traps can also be used for storing beryllium ions and protons.

A **proton source** (marked in yellow) is attached at the end of the trap stack. It contains an electron gun and a poly-ethylen target for proton production. Details can be found in [Pick17] and [Pulido19].

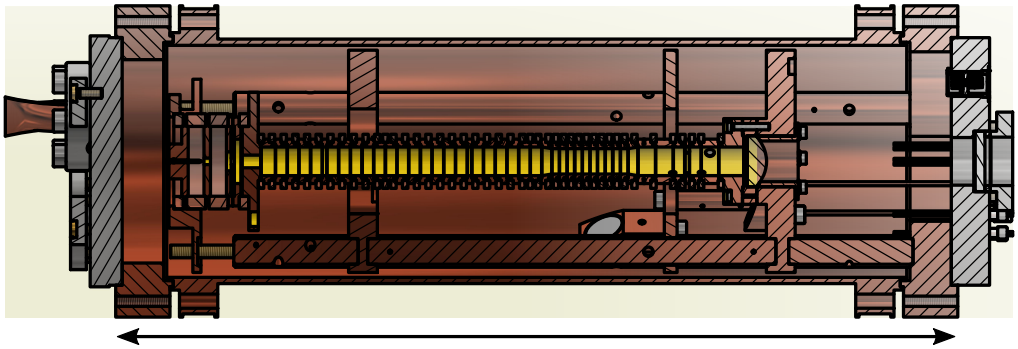

Figure 3.3: Trap stack mounted in the trap can. Cut section view. For details see text.

3.2. Trap can

The trap stack is mounted in an inner vacuum chamber called "trap can". This chamber is pumped out[1] by a turbo molecular pump and a scroll pump and closed before it is mounted to the support structure. Its purpose is to achieve extremely low pressures of down to the low 10^{-18} mbar regime [Sellner17] at the trap stack to increase the lifetime of antiprotons that will be injected into the system in the future. Another effect of the trap can is that it blocks stray light that could otherwise disturb the imaging.

The trap can consists of a cylinder made from OFHC copper and two lids. The trap can is sealed with indium wire. A cut section view of the trap can with the trap stack inside is shown in figure 3.3. The basic design of our trap can was taken from [Ulmer11]. However, we had to modify it for our purposes; especially, windows had to be implemented to allow optical access for the laser beams and fluorescence light.

The lids for the trap can are shown in figure 3.4. They consist of a ring made of OFHC copper and a steel plate vacuum-soldered on top of it. Electric feedthroughs for applying voltage signals to the trap electrodes are welded into one of the steel plates (right side in the figure). This lid also contains a window to allow the light from fluorescence detection to leave the trap can. The other lid (shown on the left) has a pinch-off tube for sealing the trap can after vacuum pumping as well as three windows: two for sending in and out the cooling and repumping laser beams and one for sending in the ablation laser. All the windows are anti-reflection (AR) coated for wavelengths of 313 nm and 235 nm (*Laseroptik, B-14996*) and indium sealed.

Before installing the trap stack, the empty trap can was sealed and a leak test

[1] The pressure values are discussed further below in this section.

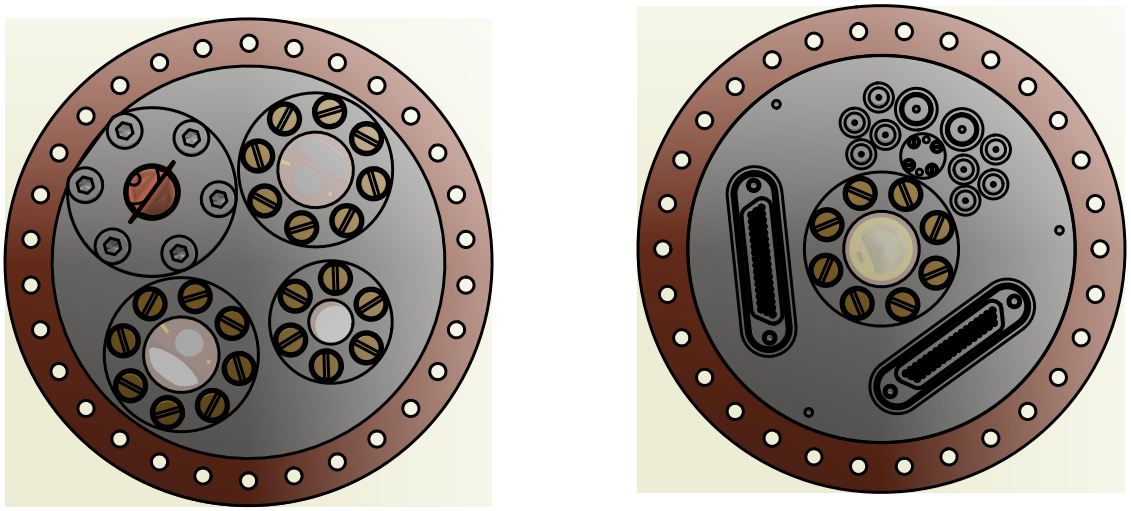

Figure 3.4: Trap can lids. The lid on the left contains two windows (15 mm effective diameter) for the cooling laser beams and one window (8.7 mm effective diameter) for ablation beam access. The lid on the right contains a window for fluorescence light (15 mm effective diameter) as well as electric feedthroughs for supply of DC and RF signals for the traps as well as high voltage signals for the proton source.

was carried out. Pressures lower than $5 \cdot 10^{-4}$ mbar at the trap can could not be reached while pumping and it was found that some of the electric feedthroughs were leaking. For sealing the feedthroughs a sprayable silicon resin (*Kurt J. Lesker, KL-5-16A*) was applied from the outside of the trap can. After sealing, the empty trap can was pumped again to a pressure of $3 \cdot 10^{-7}$ mbar. When pumping was stopped, the pressure rose to the low 10^{-3} mbar regime within about half an hour and then continued rising at a rate of rise of $2 \cdot 10^{-8}$ mbar/s. After installing the trap stack inside the trap can, the measurements were repeated. The trap can was pumped down to a pressure of $2 \cdot 10^{-7}$ mbar. When stopping the pump, the pressure rose to the low 10^{-3} mbar regime within about 15 minutes. Afterwards, it rose more slowly at a rate of $4.1 \cdot 10^{-7}$ mbar/s. The trap can was pinched off just before it was installed on the support structure. The surrounding vacuum system was closed on the same day and the vacuum pumps were started. After pumping for one week, the cryostat was turned on. The trap can passed the boiling point of nitrogen after 18 hours.

3.3. Optics setup

The optics for sending the laser beams to the trap as well as the imaging optics need to be placed as close to the Penning trap stack as possible. Since the size of

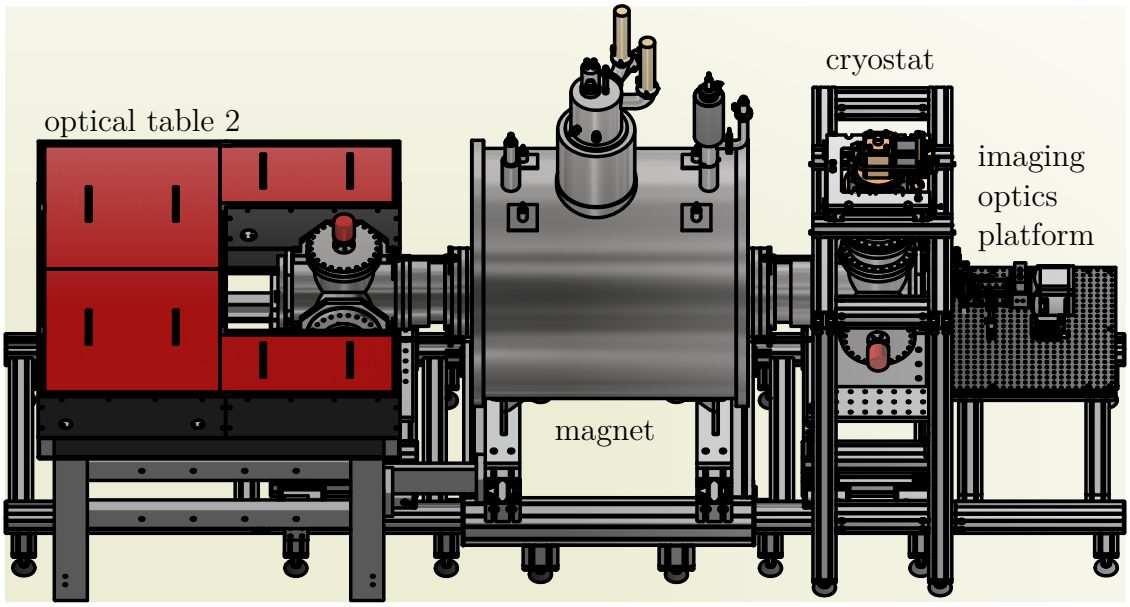

Figure 3.5: CAD drawing of the apparatus. For details see text.

our laboratory does not allow placing optical tables next to the apparatus, movable platforms are installed close to the vacuum chamber. Those platforms can be removed for opening the vacuum system. Figure 3.5 shows a Computer-Aided Design (CAD) drawing of the complete apparatus. On the left side, the optical table (called "(optical) table 2" throughout this chapter, which carries the optical components for laser beam delivery, is depicted. It is a custom non-magnetic steel construction from *Ametec*. The table is equipped with anodised aluminium walls and lids for laser safety and to protect the optical components from fast temperature fluctuations as well as air currents. On the right side, a platform carrying optical elements, a photon multiplier tube (PMT), and an electron-multiplying charge-coupled device (EMCCD) camera is mounted to the apparatus' support structure. It is a self-built platform consisting of an 60 cm by 60 cm aluminium breadbord (*Radiant Dyes, 600x600x12mm anodised aluminium*) bolted onto aluminium profiles.

3.3.1. Laser beam delivery

For laser manipulation of $^{9}Be^{+}$ ions lasers at a wavelength of 313 nm are required. We use self-built laser systems, where light at a wavelength of 626 nm is produced via sum frequency generation from 1050 nm and 1550 nm. This light is subsequently frequency doubled to 313 nm. A full description of the laser systems can be found in [Idel16].

Two of these laser systems, one for Doppler cooling and one for repumping, have been set up on a floating optical table. In the following, the beam delivery will

be described for the Doppler cooling laser shown in figure 3.6. The setup for the repumping laser is identical. The light is sent through an acousto-optic modulator (AOM) (*Gouch & Housego, I-M110-3C10BB-3-GH27*) in double-pass configuration for laser power stabilisation, laser switching, and fast frequency shifting. After passing the AOM, the light is delivered to a second static optical table (optical table 2), which is situated at the vacuum chamber, via a hydrogen loaded and cured photonic crystal fibre (*NKT Photonics, LMA-10-PM*) [Marciniak17]. On this table, the light passes a telescope that increases the diameter of the collimated laser beam to 6 mm. This is necessary to achieve a focus size as small as possible in the trap centre. Behind the telescope the laser beam passes a half-wave plate that rotates the polarisation direction of the linearly polarised beam for maximising the power behind the last beam splitter. A quarter-wave plate is inserted for matching the polarisation for the σ^+ Doppler cooling transition when crossing the trap centre at an angle of 45° with respect to the magnetic field. It was calculated that between 2 % and 75 % of the power contribute to driving the Doppler cooling transition in our setup depending on the polarisation of the laser beam. Before entering the vacuum system, the light passes a lens (*CVI Laser Optics, PLCX-25.4-772.6-UV-248*) with a radius of curvature of 772.6 mm that focuses the laser beam in the trap centre at a distance of about 1.5 m. The lens is mounted on motorised piezo stages (*Physikinstrumente, Q-545.240*) that can move the lens perpendicularly to the beam's travelling direction for moving the focus position at the trap centre. A 50/50 beamsplitter (*Thorlabs, BSW20*) is used for overlapping the Doppler and the repumping beam. At the remaining port of the beamsplitter a power head (*Thorlabs, S130VC*) is installed to monitor the laser powers. All laser power levels given in this thesis are measured at that position.

The laser for ablation is a frequency-doubled Nd:YAG pulsed laser (532 nm) with a pulse length of 5 ns to 7 ns and an energy of up to 14 mJ (*Continuum, Minilite I*). Its laser head is located on table 2 (not shown in the drawing). For not ablating material during alignment, it is overlapped with a low-power continuous-wave laser at the same wavelength.

3.3.2. Imaging setup

The imaging optics consist of an aspheric lens attached to the trap stack (see fig 3.2) for collecting the ion's fluorescence light, optical elements outside the vacuum for focusing the fluorescence light, ultraviolet (UV) filters, a PMT, and an EMCCD camera. The optical elements outside the vacuum can either be a single plano-convex lens or an aspheric lens and a focusing objective. For more details see chapter 4. The imaging setup outside the vacuum system is shown in figure 3.7. Outside the vacuum system, the fluorescence light is collected by a lens that can be moved in x-, y-, and z-direction and tilted around the x-, and y-axis to compensate misalignment of the lens attached to the trap stack. The lens directs the light onto a motorised flip mirror that either deflects it onto the PMT (*Hamamatsu, H8259-01*) or lets it pass onto the EMCCD camera (*Andor, iXon A-885-KCS-VP*) mounted on a 3-axes

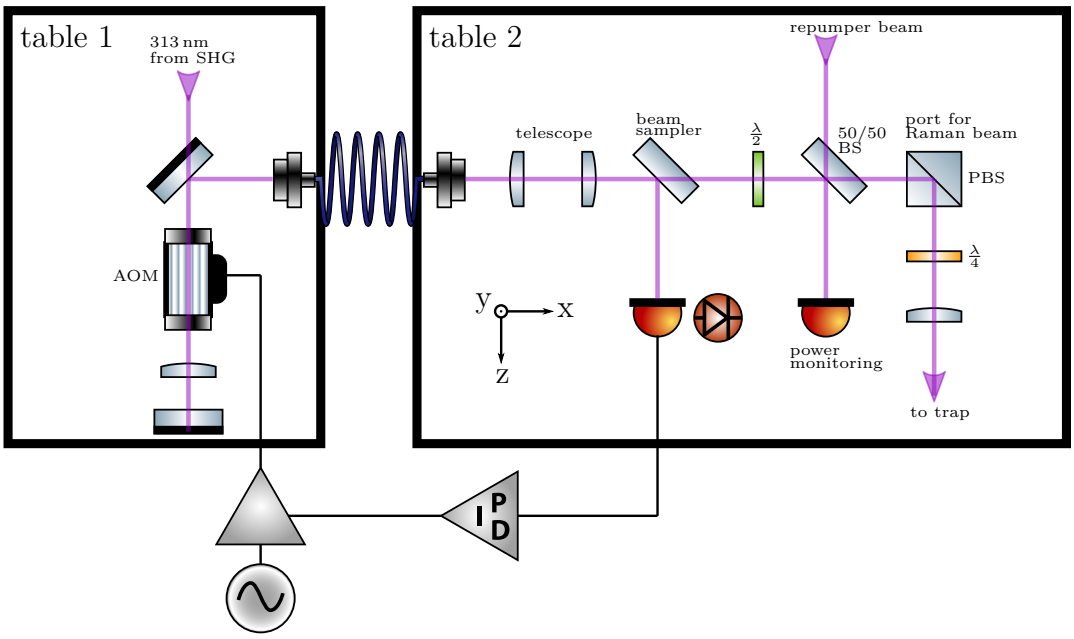

Figure 3.6: Setup for beam delivery. For details see text. Most of the components for creating this drawing were taken from [Franzen].

translation stage. The flip mirror is rigidly connected to the camera and the PMT and it is mounted in a light tight housing to protect the PMT from stray light. Therefore, it is not possible to align the flip mirror once the imaging optics have been setup. When aligning the imaging optics, the EMCCD camera is used as a reference for good alignment. The PMT can only be aligned by moving the EMCCD camera. This can lead to the case that either the PMT or the EMCCD camera is not hit centrally. This can lead to parts of the fluorescence light missing the detectors, because the image size for an ion cloud is on the order of the detectors' chip sizes. Since this occured in our case, the imaging setup was optimised for photon count numbers with the PMT. To further protect the PMT, a UV bandpass filter (*Thorlabs, FGUV11-UV*) was placed between the flip mirror box and the PMT. If a focusing objective and an aperture are used, they are rigidly attached to the flip mirror box to mitigate misalignment between the components. However, the aperture can be slightly moved in x-, y-, and z-direction to align it with respect to the fluorescence light. Since the focusing objective is heavy, it is supported by a construction with two teflon plates. This avoids bending of the objective due to its weight but still allows for alignment due to the teflon plates sliding on each other. A second UV bandpass filter was mounted either before the aperture or before the single lens, if no aperture and focusing objective are used (not shown in the cut section view) to protect the camera from stray light. This filter can be removed for alignment of the ablation laser beam. For details on the characteristics and design of the imaging optics see sections 4 and A.

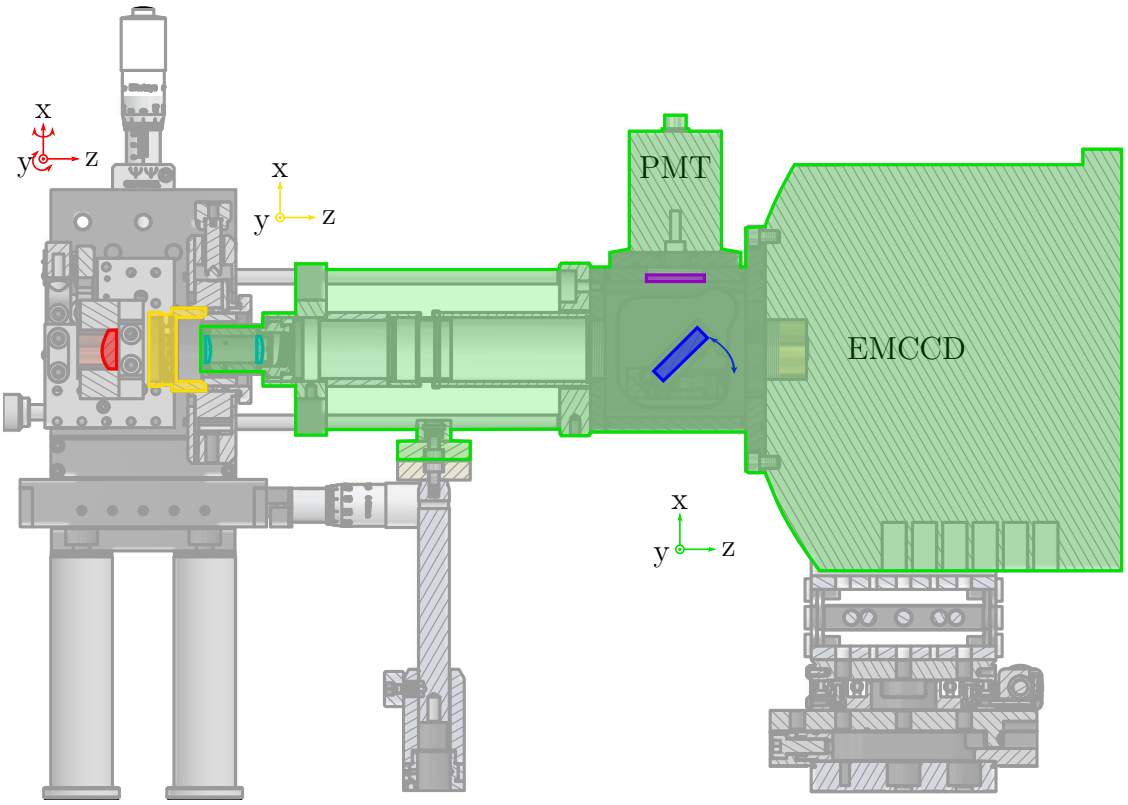

Figure 3.7: Imaging optics setup. Cut section view of the imaging components outside the vacuum. The lens (red) that directs the fluoresence light coming out of the vacuum system onto the detectors is attached to a five-axes alignment stage. Optionally, a movable aperture (yellow) as well as a focusing objective (turquoise) can be implemented. Using the flip mirror (blue) the light can either be directed onto the EMCCD or the PMT, which is protected by a UV bandpass filter (purple). The PMT, the EMCCD, the flip mirror box and, optimally, the focusing objective are rigidly attached to each other and are mounted on a three-axes translation stage. For details see text.

3.4. Trap wiring and electronic infrastructure

Figure 3.4 shows the wiring of the beryllium trap and the coupling trap. The DC signals are filtered by three identical low-pass filters, each placed at a different temperature stage. The filters consist of a resistor with a resistance of 5 kΩ and a capacitor with a capacitance of 4.7 nF. This leads to a cut-off frequency of 1.3 kHz, which is a trade-off between supressing noise and allowing fast adiabatic ion transport. The DC voltages are generated by a self-built programmable arbitrary waveform generator (AWG) named "PDQ" [Bowler13]. The PDQ generates DC voltages in the range of ±10 V at an update rate of 50 MHz and a resolution of 16 bit. Electrodes

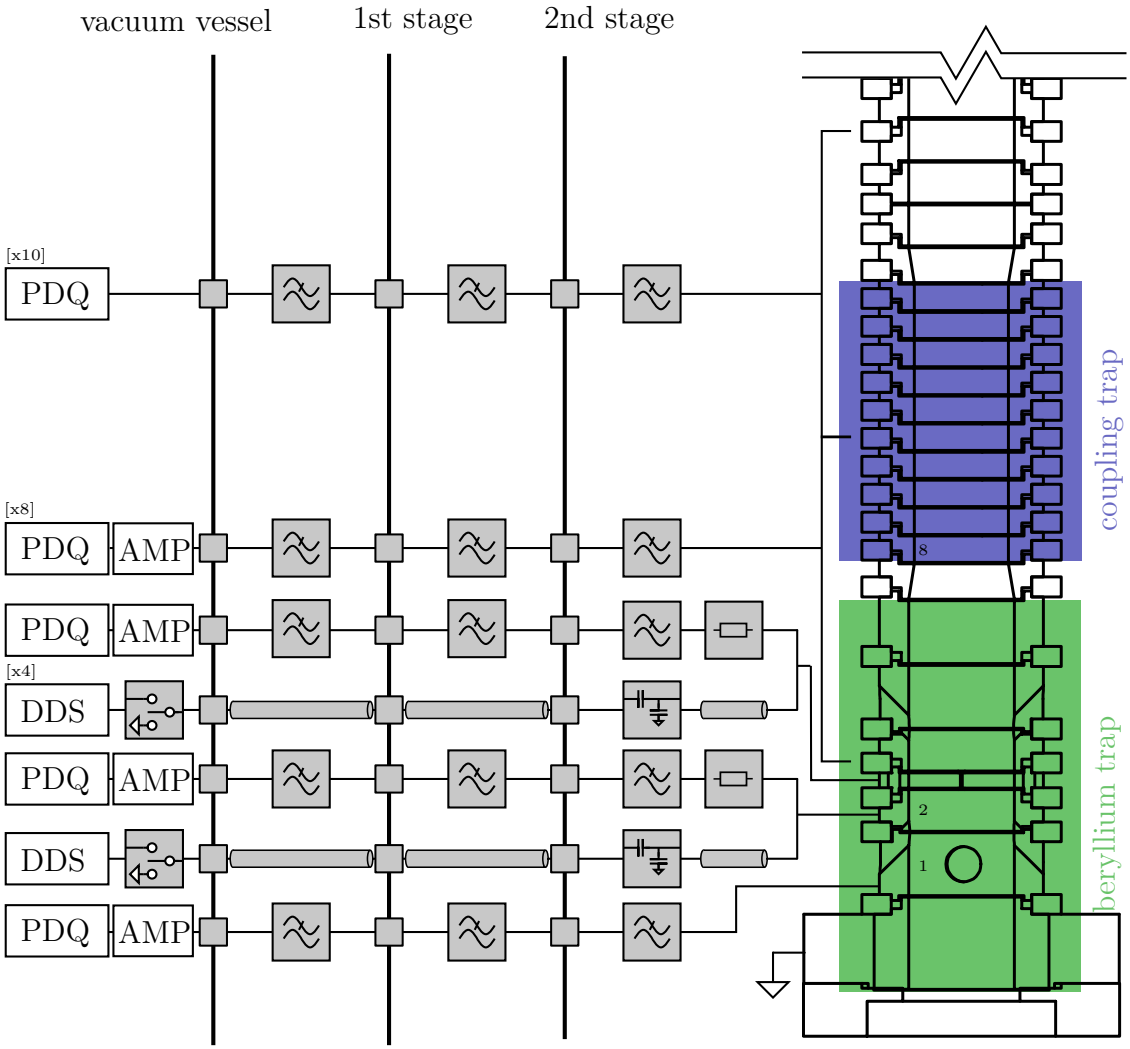

Figure 3.8: Electronics for the beryllium trap and the coupling trap. The numbers on the electrodes denote how the electrodes are counted throughout this thesis. Figure taken from [Niemann19a] and adapted.

1 to 11 are amplified by a self-built amplifier to ±30 V.

In the beryllium trap the four segments of the ring electrode as well as one of the correction electrodes are equipped with RF lines for exciting the axial and radial motion of the ion and for applying axialisation. The RF signal is generated by an amplitude tunable direct digital synthesis (DDS) (*m-Labs, Sinara 4410 DDS "Urukul"*), which provides an output power between -21.5 dBm and 10 dBm. Fixed attenuators are included in the lines to reduce the power level by 40 dB for the axial line and 60 dB for the radial line. These values were determined experimentally. For these electrodes, the cut-off frequency of the direct current (DC) lines changes to 1.2 kHz due to an additional resistor with a resistance of 1 MΩ and a capacitor

with a capacitance of 33 pF, which is part of a capacitive voltage divider in the excitation line with capacities of 150 pF as well as the above mentioned 33 pF to ground.

The wiring for the precision trap was adapted from [Schneider14]. The details for wiring these traps are omitted, since all measurements for this thesis were conducted in the beryllium or coupling trap.

3.5. Experiment control

For controlling the experiment, the control system *ARTIQ (Advanced Real-Time Infrastructure for Quantum physics)* from *m-Labs* [mLabs] is used. It is a modular experiment control system that allows executing experimental sequences in real time, once the experiment code is compiled. It provides several hardware modules as well as a software. In this thesis the hardware modules DDS (*Sinara 4410/4412 DDS "Urukul"*), digital-to-analog converter (DAC) (*Sinara 5432 DAC "Zotino"*), and transistor-transistor logic (TTL) (*Sinara 2118 TTL cards*) were used. The interface between the software and the hardware is the field programmable gate array (FPGA) based module *Sinara 1123 Carrier "Kasli"*. The software *Artiq Master* communicates with *Kasli* via network. Besides compiling code for *Kasli* that is executed in real time, any *Python*-controllable non-proprietary device can be implemented e.g. via network or serial interface. The PDQ takes a special role being no *ARTIQ* hardware module but nevertheless operating in real time. For timing *Kasli*, an internal clock is used.

An overview over the experiment control infrastructure is given in figure 3.9. The *Artiq Master* controls a wavelength meter (*Highfinesse, WSU-2*) that is used for stabilising the fundamental frequencies of the cooling and repumping lasers with respect to a helium-neon laser with an accuracy of 2 MHz. The RF signal for running the AOMs is generated by *Urukul* and amplified by an adjustable 10W RF amplifier developed at Physikalisch-Technische Bundesanstalt (PTB). The proportional-integral-derivative (PID) controller for power stabilisation of the AOM is a 2-level sample and hold (S&H) regulator built at PTB. Its setpoint is controlled by *Zotino*. TTLs are used for steering the flip mirror in the imaging setup (output mode) as well as for registrating PMT counts (input mode). The excitation signals for the beryllium trap are generated by *Urukul* and the DC signals as well as the waveforms for ion transport by the PDQ.

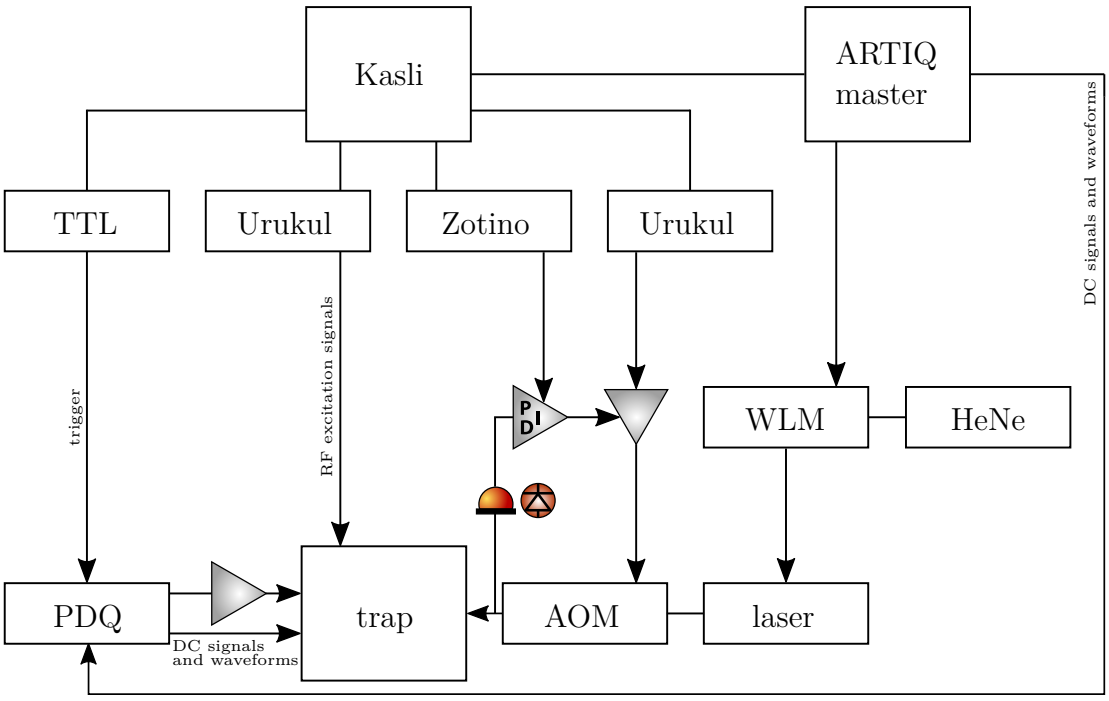

Figure 3.9: Experiment control infrastructures. Some components for creating this drawing were taken from [Franzen].

Chapter 4
Imaging optics

For cylindrical Penning traps, there are two common ways of implementing fluorescence detection: The ions can either be detected in the radial direction or in the axial direction. In the case of the radial direction, some of the fluorescence light travels through a hole in the ring electrode and is then collimated or focused by a lens. It must be deflected about 90° outside the trap to guide it parallel to the trap axis out of the magnet as has been done by [Mavadia13]. Radial imaging is not applicable to our system. Even though our magnet has a bore with a diameter of 160 mm implementing this approach is technically challenging since the bore is filled with support structure to provide a good thermal contact between the trap and the cryostat (see chapter 3). Furthermore our ring electrode only has a length of 1.3 mm. That means only a small fraction of 0.3% of the fluorescence light would travel through a hole of 1 mm diameter in this electrode. Therefore we collect the ion's fluorescence along the axial direction. In this case the light leaves the trap in the axial direction and is then collimated or focused with a lens. In this direction we can collect a fraction of 1.6% of the light scattered by the ion.[1] The design of the imaging optics is described in section 4.1.

4.1. Design

Designing the imaging optics, two goals were pursued: The primary goal was to guide as much light from the ion as possible onto a PMT. The secondary goal was to optimise the imaging quality to image the ion on a CCD chip in order to be able

[1] Please note that the given fractions are only rough estimates: Sphere segments were approximated by disks. Furthermore, the spatial intensity distribution of the fluorescence light was approximated to be spheroidal. However, for σ^+ polarised light $I(\theta, \phi) \propto \frac{1+\cos^2\theta}{2}$ where ϕ is the angle in the plane perpendicular to the magnetic field lines and θ the azimuthal angle with respect to the magnetic field [Hertel17]. So along the axial directions more light is emitted than along any axis in the radial plane.

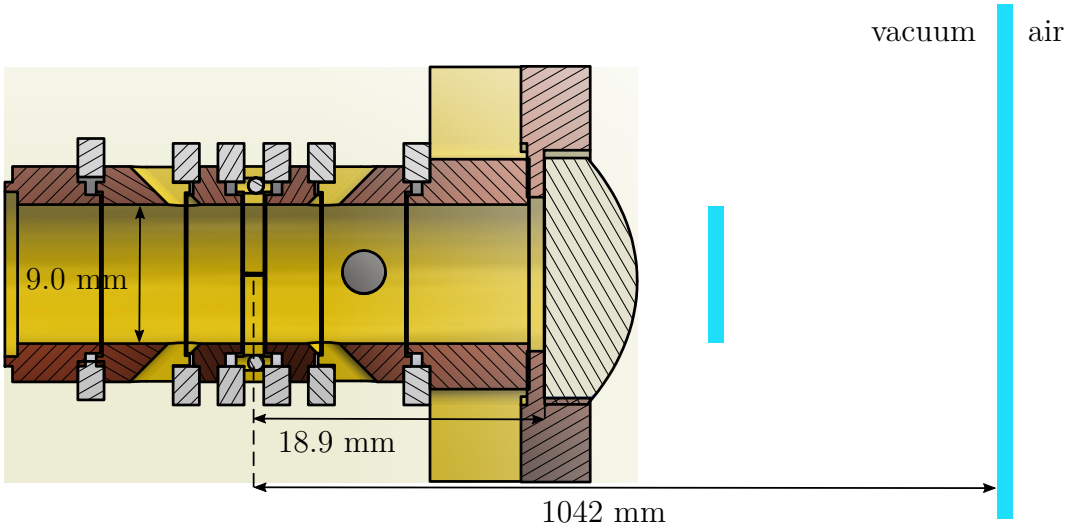

Figure 4.1: Beryllium trap with focusing lens. Cut section view of the beryllium trap. The aspheric lens (shown in beige) is attached to the trap stack and guides the light through the cold stage to the outside. An intermediate focus can be found at a distance of 548 mm from the lens. The trapcan window as well as the vacuum window position are indicated by the lines in light blue (not to scale). The trap electrodes are shown in yellow, their cut surfaces in brown. Sapphire rings and balls are depicted in light grey. For details see text and figure 4.2.

to determine not only the amount of light but also the radial distribution of the light at the trap centre. Therefore a focusing lens was placed as close as possible to the trap centre, namely directly attached to the trap stack at a distance of 18.9 mm from the trap centre as shown in figure 4.1. The limiting aperture is the inner diameter of the beryllium trap, which is 9 mm and extends along the trap axis to the end of the endcap which is at a distance of 17.8 mm from the trap centre. This corresponds to a numerical aperture of 0.25, a solid angle of 0.2 sr, and an opening angle of 28.7° in any plane along the trap axis, respectively. From the trap centre the light has to travel a distance of 1042 mm before it leaves the vacuum system (see chapter 3).

Optical elements for imaging that are placed inside the vacuum system must be attached to the trap stack or the 4 K-stage. They could be misaligned by machining tolerances of the trap stack and the stage, respectively, or due to material contraction while cooling the system from room temperature down to 4 K. Therefore, we refrained from placing additional lenses inside the vacuum system, since we cannot align elements inside the system once it is closed. Although motorised stages that work at cryogenic temperatures exist, they are very expensive and space consuming and would not fit inside the apparatus.

The focusing lens attached to the trap stack needs to guide the collected

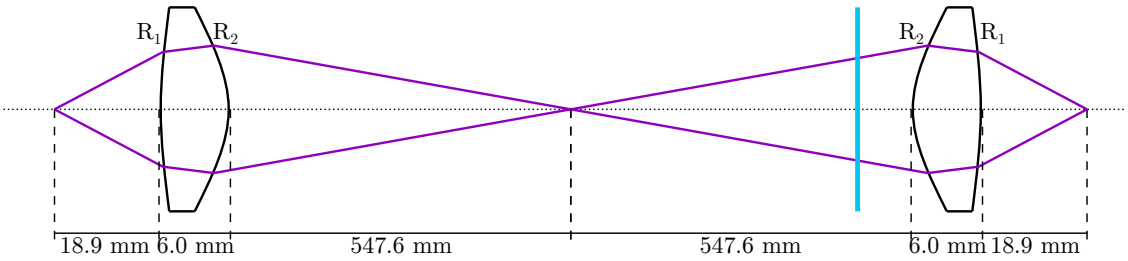

Figure 4.2: One-to-one imaging. The light scattered by the ion is projected to the image plane that lies outside the vacuum with a magnification of 1. This is achieved by two identical aspheric lenses that are placed in opposite orientation at a distance of $2d$ where d denotes the distance from the aspheric lens on the left side to the intermediate image of the ion. The aspheric lenses have radii of curvature of $R_1 = 54.8\,\text{mm}$ and $R_2 = 12.3\,\text{mm}$. Drawing not to scale.

fluorescence light out of the vacuum system. Besides, the imaging optics should be insensitive against tilting the focusing lens by 1° and displacing it by 0.1 mm radially from the optical axis to account for the possible misalignment mentioned above. Furthermore, the imaging quality should be as good as possible while keeping the total number of needed elements as small as possible to guarantee a robust system that is straight-forward to align.

To meet all these goals, the lens attached to the trap was self-designed in a way that it focuses the light from the trap centre at a distance of 548 mm which is slightly more than half way from the trap centre to the vacuum window. To reduce spherical aberrations, the lens's surfaces are aspheric. For the lens design, the software *OpticStudio* by *Zemax* was used. Details on the optimisation process and lens parameters can be found in appendix A.

By placing a copy of the lens in reversed orientation and identical distance to the focus, a one-to-one imaging of the ion outside the vacuum is achieved as shown in figure 4.2. This real image can be further imaged as described in section 4.1.1.

4.1.1. Application options

Although we aimed for one-to-one imaging when the aspheric lens was designed, there are several possibilities to image the light outside the vacuum. In this thesis two approaches are described and discussed that use as few optical elements as possible to reduce complications during alignment.

i Taking the one-to-one imaging shown in figure 4.2 as a starting point, a focusing objective can be used to magnify the image and focus the light onto the detector as depicted in figure 4.3 (a).

ii The aspheric lens outside the vacuum can be replaced by a spheric lens that

directly focuses the light onto the detector as shown in figure 4.3 (b) and (c).

Both application options exhibit advantages and disadvantages. The advantage of option (i) is that it has an intermediate focus outside the vacuum that allows for spatial filtering. By inserting a circular aperture in the focus, stray light not originating from the trap centre can be blocked. This leads to an increased signal to noise ratio on the detector. The downside of this system is that the distance between the aspheric lens outside the vacuum and the microscope objective is critical for imaging due to the large numerical apertures of both the aspheric lens and the focusing objective, which leads to a small depth of focus and depth of field, respectively. For a deviation of a few millimetres from the ideal distance, no image can be found on the EMCCD camera. Option (ii) is simple in alignment since it is robust with respect to the exact distance between the lenses. Even if the distance between the lens and the camera deviates by several millimetres, a defocused image will be created on the EMCCD camera which then can be optimised by adjusting the distance. Because of the lack of an intermediate focus outside the vacuum, spatial filtering is not possible in this setup. Both systems are relatively insensitive to the exact distance between the in-vacuum lens and the first component outside the vacuum, since deviations from the simulated distance cause only small shifts of the image position. For a deviation of x from the ideal distance, the image plane moves by $\frac{x}{5}$ for options (a) and (b) and $\frac{x}{20}$ for option (c). Issues only occur when the distance expands to the point where clipping occurs.

4.1.2. Testing

Before implementing in the experiment, the imaging optics shown in figure 4.2 (b) were experimentally tested in the laboratory in a test setup (see figure 4.4). Since for that purpose no light at a wavelength of 313 nm was available, a UV light-emitting diode (LED) irradiating light at a wavelength of 315 nm was used. This leads to deviations of up to 3 % in the ideal distances between the optical elements.

In the test setup the UV LED was mounted on an optical table and a USAF 1951 bar target was attached to it. This target simulates the ion, i.e. it is located in the object plane. At a distance of 18.9 mm the aspheric lens, which was mounted on a tiltable stage, was placed. The plano-convex lens and the EMCCD camera were aligned such that the image was centered on the camera and as focused as possible (see figure 4.5). The optical componentes were coarsely placed and deliberately without using an optical bench. This was done since the alignment of the aspheric lens might not be perfect due to machining imperfections of the trap stack or to cooling down the trap stack to 4 K.

The aspheric lens was tilted around an axis perpendicular to the optical axis by 2° in each direction although no tilts larger than 1° are expected in the apparatus. All other components were kept fixed. After tilting, the image of the centre of the bar target was still visible on the EMCCD chip. From figure 4.4 a magnification of

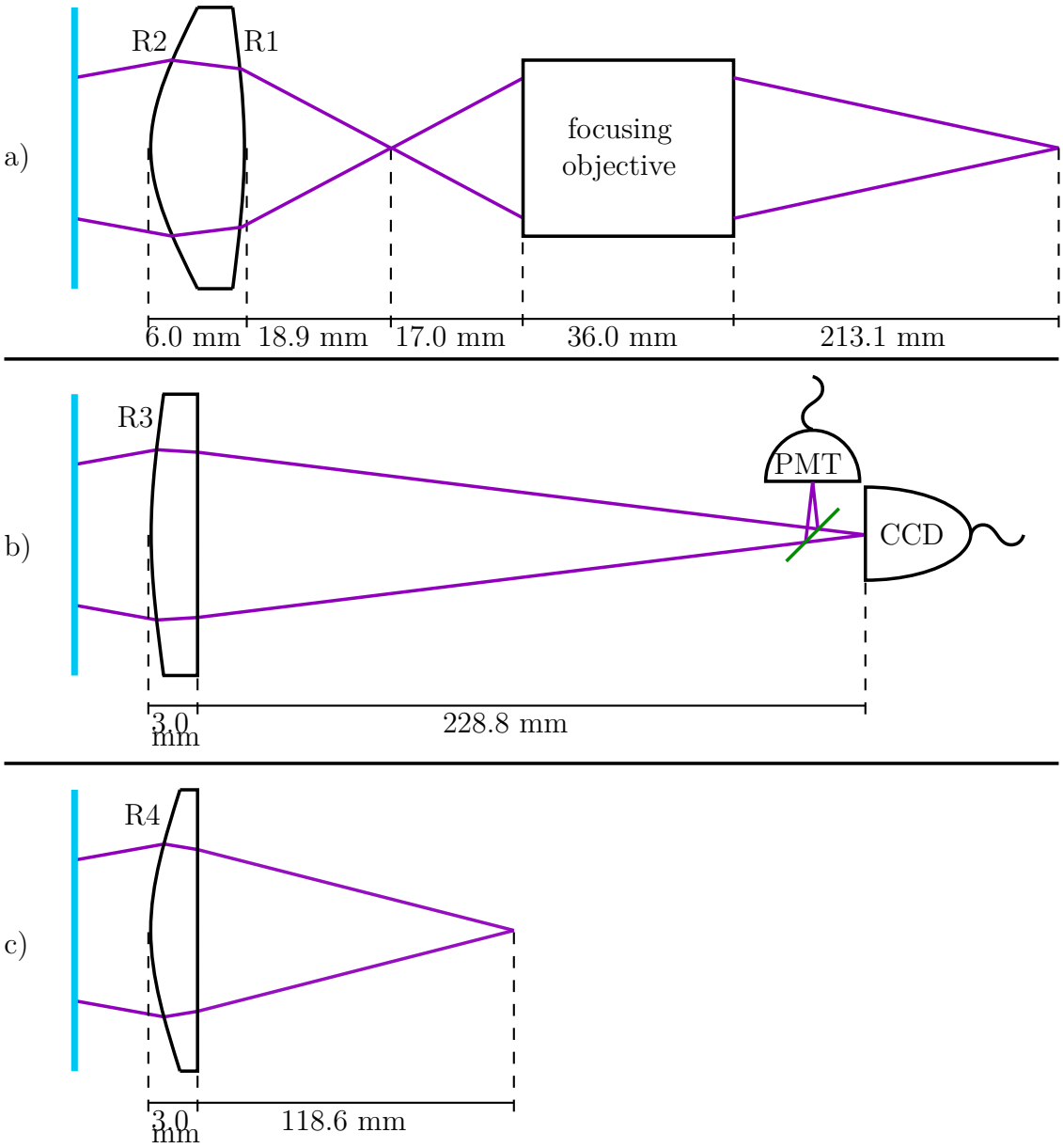

Figure 4.3: Imaging optics options. The blue line represents the vacuum window. Purple lines indicate the path of the fluorescence light. The CCD camera and PMT are implemented for all three systems as shown in (b). The green line represents a motorised flip mirror for switching between the CCD camera and the PMT. Option (a): An intermediate focus outside the vacuum is created using a copy of the aspheric lens attached to the trap stack (one-to-one imaging). Radii of curvature are $R_1 = 54.8\,\text{mm}$ and $R_2 = 12.3\,\text{mm}$. The focusing objective is the stock component number *LMU-10x-UV* from *Thorlabs*. Its exact composition is not specified. Option (b): Plano-convex lens number *#48-289* from *Edmund Optics*. $R_3 = 80.23\,\text{mm}$. Option (c): Plano-convex lens with custom AR coating from *Laseroptik Garbsen*. $R_4 = 50\,\text{mm}$. All lenses are made from fused silica and are coated with a dielectric coating that is suitable for light with a wavelength of 313 nm. The magnification of options (a) and (b) is 11. Option (c) has a magnification of 6.

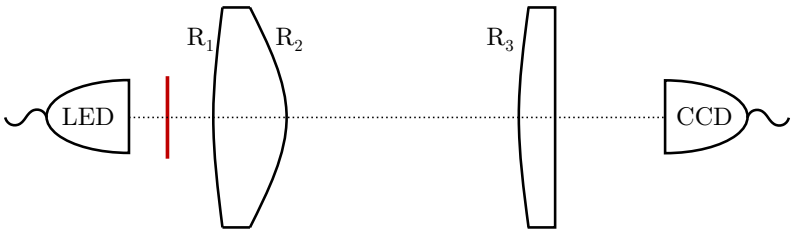

Figure 4.4: Imaging optics test setup. The bar target is represented by the red line. The radii of curvature are $R_1 = 54.8\,\text{mm}$, $R_2 = 12.3\,\text{mm}$, and $R_3 = 80.23\,\text{mm}$. Between the UV LED and the bar target, a diffuser *Thorlabs, DGUV10-1500* is placed (not shown in drawing) to reduce coherence of the light source to avoid interference effects at the bar target. Drawing not to scale.

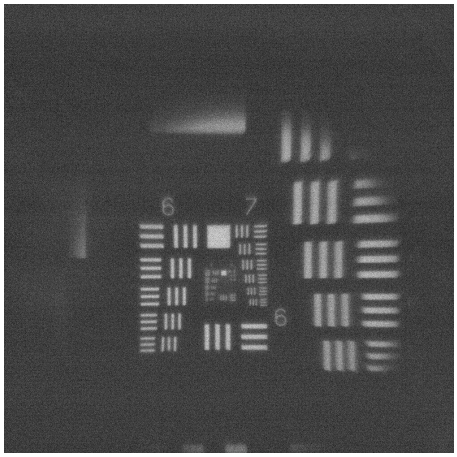

Figure 4.5: Optimised image of a bar chart. The test setup shown in figure 4.4 was used. For details see text.

12 was determined. Although the simulations predicted a magnification of 11, the results are in good agreement since reducing the distance between the ion or bar target and the aspheric lens by only 30 µm in the simulations leads to a change of the magnification from 11 to 12.

4.2. Implementation

All imaging systems shown in figure 4.3 were implemented in the experiment one after another. First, the setup creating a one-to-one image which is then magnified by a focusing objective (4.3 (a)) was implemented. With this system, clear images of the ions could be obtained. However, the magnification was different than expected. Although we cannot determine it since we do not know the radial spread of the

ion cloud in the trap, we could create situations where the ion cloud filled the complete chip area of the EMCCD camera. With a chip size of 8 mm by 8 mm and a magnification of 11, this would lead to a radial extent of the ion cloud of 0.7 mm. But from simulations, the imaging system can only image a circular area with a diameter of 0.3 mm in the radial plane due to the small entrance aperture of the focusing objective. This means that the imaging system has a larger magnification than expected. The first assumption was that the imaging optics were poorly aligned. Since this system is more complicated to align than the imaging systems that only use a plano-convex lens instead of an aspheric lens and a focusing objective (4.3 (b) and (c)), we decided to exchange the imaging system for the system with a plano-convex lens with a radius of curvature of 80.23 mm ($f \approx 175$ mm, 4.3 (b)) to evaluate whether we receive more meaningful results with this version since it worked well in our previous experiment setup [Niemann19a]. However, it was not possible to image the ions with that configuration. Therefore, we replaced the plano-convex lens by plano-convex lenses with radii of curvature of 50 mm ($f \approx 100$ mm) and 25 mm ($f \approx 50$ mm), respectively. For both configurations imaging of the ions was possible. Finally, the lens with a radius of curvature of 50 mm was implemented in the experiment.

A possible explanation for this behaviour is that the distance between the ion and the lens attached to the trap is smaller than designed. This would cause a shift of the intermediate focus towards the vacuum window. For a reduction of 300 µm of the ion-lens distance, the distance between the $R = 50$ mm plano-convex lens and the EMCCD camera increases by 21 cm. Since the space on our imaging platform is limited (see section 3.3) it was not possible to compensate such shifts. If the distance between the ion and the aspheric lens was reduced by 400 µm, the intermediate focus would lie in the focal length of the plano-convex lens. Thus, no real image can be formed. However, when using a plano-convex lens with a smaller focal length or the aspheric lens and the microscope objective, the ions can be imaged. This leads to the assumption that either the distance between the aspheric lens attached to the trap and the trap centre is smaller than expected due to machining tolerances, or that the potential minimum of the electric field is not located in the geometrical trap centre. Since the electrodes have been machined to a precision of 10 µm and only four electrodes are placed between the aspheric lens and the trap centre, the first assumption can be excluded. Furthermore, the electrodes are gold-plated which would rather lead to a larger than to a smaller electrode thickness. A hint for the latter assumption is given by the observation that the image is defocused when the tuning ratio is changed. Figure 4.6 shows that the image is focused on the EMCCD chip for a tuning ratio of 0.9, which is the tuning ratio that was applied to the trap when the imaging optics were aligned. When changing the tuning ratio in either direction, the image is defocused, even though this should not affect the ions' position. This leads to the assumption that the electric potentials created by the correction electrodes are not exactly the same so a change of the tuning ratio leads to an axial displacement of the ions.

Besides the defocus the image moves in the radial plane. A movement along the

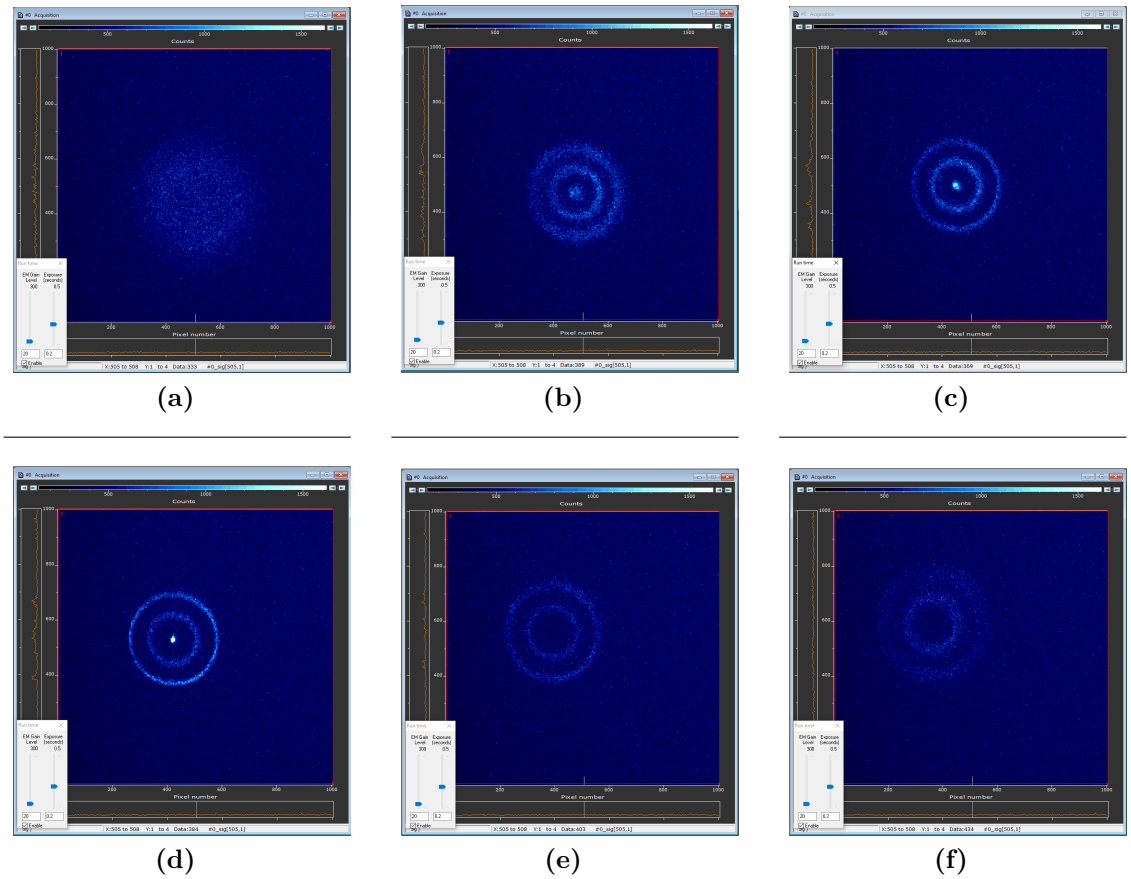

Figure 4.6: Ion cloud for different tuning ratios. Tuning ratios are: 0.87 (a), 0.88 (b), 0.89 (c), 0.90 (d), 0.91 (e), and 0.92 (f).

trap axis is translated into a radial movement of the image on the camera when the trap axis is not parallel to the optical axis of the imaging optics. But this radial displacement cannot be fully explained by a misalignment of the imaging optics: When the trap depth was varied at a fixed tuning ratio, the image moved in the radial plane but no defocus could be observed (figure 6.7). Furthermore, one segment of the ring electrode seems not to be correctly connected (for more details see 6.2). Therefore we conclude that the electric field is not radially symmetric at the centre of the beryllium trap.

Chapter 5

Particle preparation and trap characterisation

The aim for the current experimental apparatus is to sympathetically cool a single beryllium ion using a second co-trapped beryllium ion. The two ions shall exchange their motional energy via Coulomb coupling of their motional modes in the coupling trap. To reach this goal the following ingredients are needed: Two single $^{9}Be^{+}$ ions, one of them being in a low state of motional energy (cold) or at least in a lower motional state than the other one. This colder ion must initially be stored in the coupling trap and the hotter ion in the beryllium trap. Furthermore, adiabatic transport of single ions through the trap stack must be realised to allow shuttling single ions from the beryllium trap, where they are produced, to the coupling trap and back without motional heating (for details on adiabatic transport see chapter 6). Finally, one needs a method to determine the particle number in the beryllium trap as well as the ion temperature (even though it is not indispensable to know the exact temperature it is necessary to be able to distinguish whether the particle's motional energy has increased or decreased after the motional energy exchange with the other ion).

There are basically two ways to produce single beryllium ions in a trap. One could either load the trap with a single ion or load several ions and then remove ions from the trap until only one is left. For directly producing single ions, one needs a process that produces a vapour of neutral beryllium atoms (this could either be achieved by using an oven [Brewer88], [Marciniak20] or by laser ablation [Wahnschaffe16]) and a photoionisation laser that ionises individual atoms from that vapour. Since our system does not have the technical prerequisites for photoionisation and it is a large technical overhead to maintain and introduce the required laser system at a wavelength of 235 nm, we pursue the second approach, namely to load a cloud of several ions and then reduce the particle number. Following this approach, there are again two different ways to end up with a single "cold" ion in the coupling trap and a single "hot" ion in the beryllium trap. The first way is to load a cloud of ions, reduce the number of particle to one, cool it, move it to the coupling trap, and store it there while repeating the procedure to gain a second ion in the beryllium trap.

The second way is to load a cloud of ions, reduce the number of particles until two ions are left, cool these two, move one of them to the coupling trap and heat the remaining particle in a controlled manner. Our loading procedure will be discussed in section 5.1 and the particle number reduction in 5.2. The topics cooling and temperature determination are treated in section 5.3.

Another mandatory prerequisite for adiabatic transport and Coulomb coupling is the knowledge of the trap frequencies. These will be determined in section 5.4.

Please note:

- All detunings in this chapter are given relative to the calculated atomic transition (see section 2.2.4).
- Although there is some evidence of formation of ion Coulomb crystals throughout this thesis the term "cloud" is used, no matter whether the ions form a Coulomb crystal or not. The ion Coulomb crystals in our trap have not been characterised, since the experimental goal is to work with single ions.
- In our case all ion cooling is achieved via Doppler cooling on the closed transition $S_{\frac{1}{2}} |m_J = \frac{1}{2}, m_I = \frac{3}{2}\rangle \rightarrow P_{\frac{3}{2}} |m_J = \frac{3}{2}, m_I = \frac{3}{2}\rangle$.
- The term "heating of the magnetron mode" is referring to an increase of the mode's *kinetic* energy.
- All laser powers given throughout this chapter have been measured at a fixed position (1) on the laser platform (see section 3.3.1 for the exact position). From this point the beam passes different optical elements and a vacuum window before it arrives at the trap centre. Behind the trap centre it passes another two mirrors (UV enhanced aluminum coating) and a vacuum window before it leaves the vacuum system. 54 % of the power at position (1) arrive at this point. We expect the power in the trap centre to be around 75 % of the power measured at position (1) but an accurate number cannot be given. Hence the powers given in this chapter must be understood as relative measures.
- The beam waist radius in the trap centre is estimated to be 75 µm. Since this value is only estimated and we do not know the exact laser power and laser beam position in the trap centre, the intensity cannot be determined.

5.1. Trap loading

Our attempt for loading is to produce a cloud of beryllium ions in the trap centre by hitting a solid beryllium target with a ns pulse laser at a wavelength of 532 nm (see section 3.1). The laser beam is focused onto the target and directly produces beryllium ions. The exact physical process how the ions are created is not clear. Previous

attempts of creating a neutral beryllium vapour by running the ablation laser at a lower power and subsequent ionisation via a 2-photon process using a second laser at 235 nm were unsuccessful. For details see [Niemann19a].

The ns-pulsed ablation laser used for loading our traps is operated in single shot mode by manually triggering its Q-switch. The laser is focused onto a beryllium target located in one of the endcap electrodes (section 3.1) where it produces beryllium ions.

The following steps are taken to capture an ion cloud in the trap centre:

i **A trapping potential of −1 V at the ring electrode and a tuning ratio of 0.88 is applied to the trap.** This voltage was experimentally found: For higher voltages more particles are trapped, for lower voltages reliable loading was not possible.

ii **The Doppler laser is turned on and its frequency is repeatedly swept with a sawtooth function ramping from −700 MHz to −60 MHz relative to the calculated transition frequency within 20 s.** This ramp allows for fast and efficient cooling of the initally hot ion cloud.

iii **The ablation laser is triggered and a single pulse with an energy between 80 µJ and 90 µJ is sent to the beryllium target.** This energy is the lowest that allows reliable ion production even though ion production could be observed for energies as low as 40 µJ in our former setup with the same geometry [Niemann19a]. Since initial cooling of the ion cloud needs several minutes, it is not necessary to fire the ablation laser at a specific point of the cooling laser frequency ramp.

iv **About 3 s after firing[1] the ablation laser, the trap voltages are changed to −20 V at the ring electrode and a tuning ratio of 0.88.**

v **After waiting until the ions' fluorescence signal is visible and bright on the EMCCD camera[2], the particle number is reduced applying the scheme described in section 5.2.** At this point, the ions are cold enough for being confined in the trap centre and thus detectable by the imaging system (see chapter 4).

5.2. Particle number reduction

Regardless of whether we implement a photoionisation laser for trap loading or not, there will most probably be more than one ion in the trap. But since the aim

[1] At the time where one person pushes the single shot button of the ablation laser, a second person submits the Artiq script that sets the trap voltages to the new values. This script contains a fixed delay of 3 s, which is executed in real time. Additional time is consumed by Artiq to process the information.

[2] The waiting time varies between a few seconds and several minutes.

of the experiment is to work with single $^9Be^+$ ions, the particle number must be reduced after loading the trap. There are several ways how to achieve this. One way is to pulse the endcaps to cause the loss of ions that move on a large orbit [Goodwin15]. Another way is to divide the ion cloud into two parts by converting the trap potential to a double-well potential [Smorra15b]. While one half of the ions is kept, the other half is ejected from the trap.

We pursued the second approach. Therefore a particle number reduction scheme based on the scheme described in [Smorra15b] has been developed and implemented in our former experiment control hfGUI [Niemann19a]. In this work, the scheme was further developed and implemented in our new experiment control Artiq.

In total the sequence has a duration of 1 s that is split in four parts of equal length. During each part distinct electrodes' DC voltages are ramped linearly in time from an initial value at time 0 ms to a final value at time 250 ms. First, starting from a harmonic trap potential with −20 V at the ring electrode and a tuning ratio of 0.88, which are the final trap parameter from the loading sequence, the endcaps are ramped from ground to −30 V. This leads to a double-well potential along the trap axis with a shallow barrier that allows the ions to spread in this direction (figure 5.1(b)). Second, the ring electrode is ramped up to 25 V to act as a wedge that strongly separates the wells and thus divides the ion cloud into two parts (figure 5.1(c)). Third, one of the end cap electrodes is ramped to ground to eject the ions from the respective well (figure 5.1(d)). Finally, all electrode voltages are ramped back to their initial voltages (figure 5.1(a)).

This particle number reduction scheme is applied to the ions several times while sweeping the Doppler laser frequency with a sawtooth function ramping from −700 MHz to −60 MHz within 20 s (the same as for loading the trap). It is usually applied twice with a waiting time of 99 s between the separations. Afterwards, the ion fluorescence is monitored with the EMCCD camera. The reduction scheme is repeated until the fluorescence image looks similar to figure 5.2.

In principle, this scheme is capable of reducing the ion number until only one single ion is left in the trap. However, for low ion numbers (about one to three ions), the fluorescence signal gets very unstable. The system suffers from fluorescence dropouts of seemingly random length and frequency [Niemann19a]. One possible reason for this behaviour could be that the ion undergoes a transition to the $S_{\frac{1}{2}} |m_J = -\frac{1}{2}, m_I = \frac{3}{2}\rangle$ state. It could quickly be brought back to the $S_{\frac{1}{2}} |m_J = \frac{1}{2}, m_I = \frac{3}{2}\rangle$ state by applying a repumping laser at the correct frequency that needs to be experimentally determined. Repumping has not been implemented so far but is planned for the near future. Another reason could be that the ions are heated and the radius of the magnetron orbit suddenly increases to a size where the ions cannot be detected by the imaging optics anymore. This heating of the magnetron mode could be caused by position fluctuations of the cooling laser beam with respect to the ion cloud. Since the apparatus stands directly on the floor and not on an optical table, the whole system is most probably vibrating. The beam

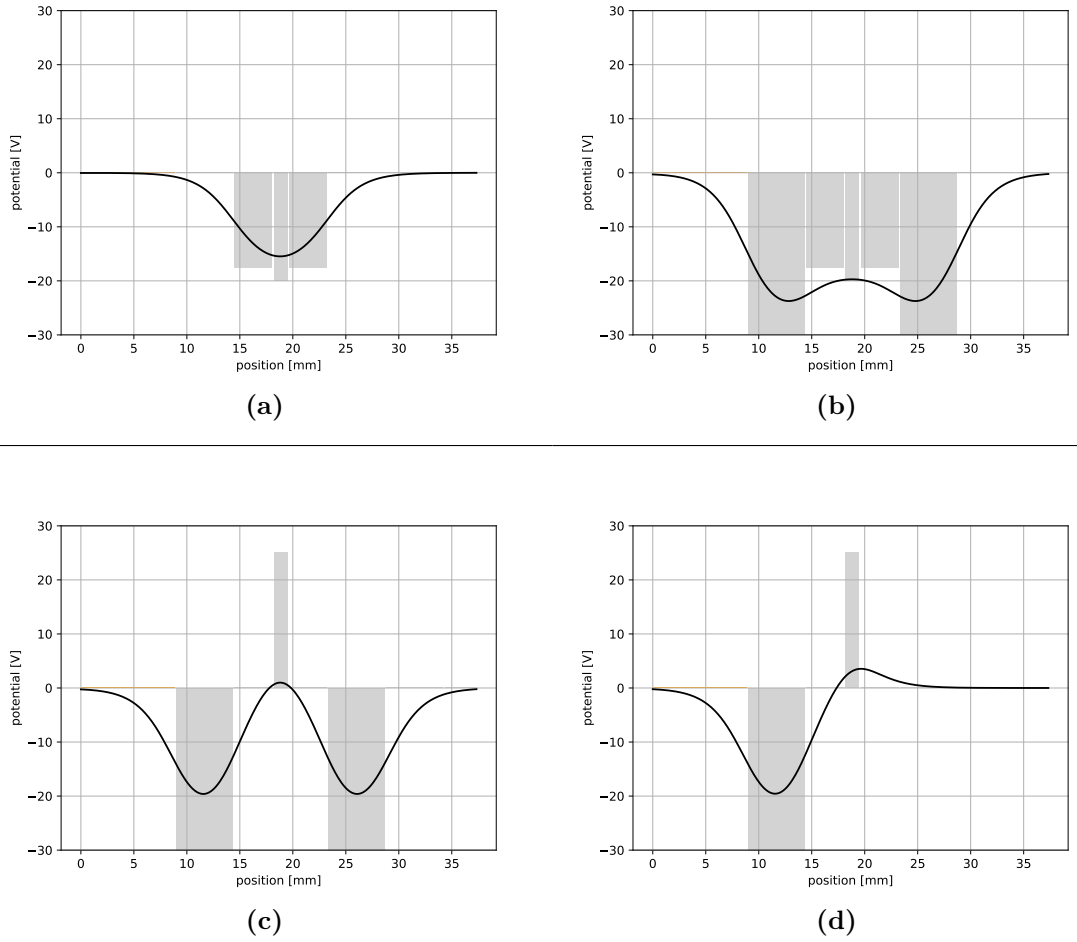

Figure 5.1: Cloud size reduction scheme. The electric potential along the trap axis is shown in black. The voltage applied to the single electrodes and their width is represented by the grey bars. The electrode functions from left to right are: endcap, correction electrode, ring electrode, correction electrode, endcap. All other electrodes are held at 0 V for the whole sequence. Starting from the harmonic trap potential with the ring electrode at −20 V (a) the end cap electrodes are ramped from ground to −30 V (b). Then, the correction electrodes are ramped to 0 V and the ring electrode to 25 V simultaneously to separate the cloud and store the residuals in the two wells of a double-well potential (c). Afterwards, one correction electrode is ramped to 0 V to release the ions in the right hand side potential well from the trap (d). Finally, all electrodes are ramped back to their initial values (a). The duration of each step is 250 ms, so the total duration of the sequence is 1 s. All voltage ramping is performed linearly in time.

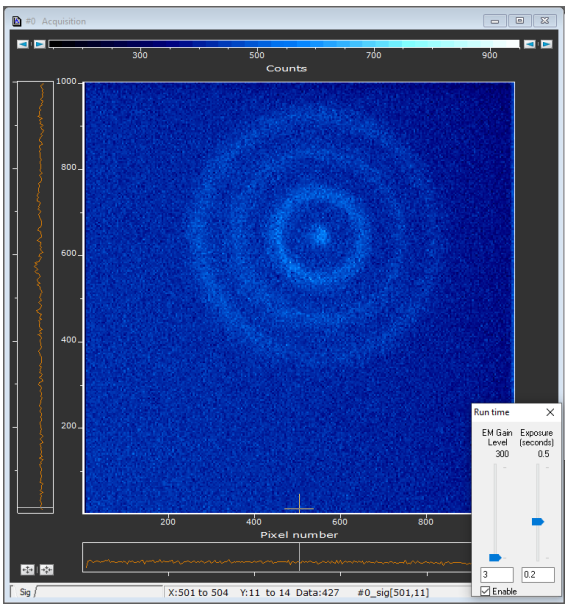

Figure 5.2: Cloud after applying the reduction scheme. The fluorescence has been recorded along the trap axis with the EMCCD camera (binning: 4x4, electron multiplier gain: 3, exposure time: 0.2 s).

pointing stability could be improved by implementing a beam pointing stabilisation for the cooling laser which is planned for the near future. When the fluorescence dropouts are reduced and a single ion is obtained, axialisation could be implemented to reduce the influence of the cooling laser position on the magnetron radius (see section 2.2.3).

Due to these problems, we currently stop reducing the ion number at a point where we know from experience that the ion fluorescence level is still stable in our trap. Further investigation on that issue is planned.

5.3. Doppler cooling

As discussed in section 2.2.1, it is crucial to radially displace the cooling laser from the trap centre to achieve efficient laser cooling in a Penning trap. In our setup, we can control the position of the cooling laser beam using motorised piezo translation stages that move the lens for focusing the laser beam in the trap centre transversally (see section 3.3.1). While cooling, the ions' fluorescence is monitored on the EMCCD camera and the piezo stages are aligned on the fly in a way that leads to the most efficient cooling achievable. This alignment of the laser beam with respect to the ions is necessary since our laser position is drifting. For describing the criteria for good beam alignment we must distinguish two cases: scanning the laser frequency and keeping the laser frequency at a fixed detuning.

Whenever we want to cool a hot cloud of ions we first scan the cooling laser frequency over a range from −700 MHz to −60 MHz to achieve fast cooling of hot particles and later set the laser to a fixed frequency red detuned (ideally by half the natural linewidth) from the transition frequency to keep the ions cold. For this we set the laser frequency to a value between −60 MHz and −70 MHz.

In the case of scanning, a diagram is considered where the fluorescence intensity (y-axis) is shown as a function of time (x-axis). The laser beam is aligned in a way that the fluorescence peaks increase over time. At some point the fluorescence starts decreasing and cannot be increased by changing the laser beam position any more. At that time, the laser is set to a fixed frequency detuning at a frequency below resonance.

In case of a fixed laser frequency detuning, the spatial spread of the ion cloud is monitored. The laser position is aligned in a way that the ion fluorescence signal has a constant intensity and spatial spreading i.e. the laser is not heating the magnetron mode (for details see section 2.2.1).

Since the system is vibrating and we have no beam pointing stabilisation, the fluorescence signal must be inspected on the EMCCD camera every few minutes and the focusing lens must eventually be realigned by repeating the procedure described above.

5.3.1. Temperature determination

The ion temperature was determined by spectroscopy of the cooling transition. The resulting lineshape is a Voigt profile i.e. a convolution of a Lorentzian function describing the natural lineshape of the transition and a Gaussian function describing broadening effects:

$$I(\nu) = A\Re(e^{-(\frac{\nu-\nu_0+i\frac{\Gamma}{2}}{\sigma\sqrt{2}})^2}\mathrm{erfc}(-i\frac{\nu-\nu_0+i\frac{\Gamma}{2}}{\sigma\sqrt{2}}))\frac{1}{\sqrt{2\pi}\sigma} \tag{5.1}$$

Here Γ denotes the natural linewidth and σ the Doppler width, A is a proportionality constant and erfc the complementary errorfuntion. The Doppler width can be associated with a temperature [Foot05]

$$T = \frac{c^2 m\sigma^2}{k_B\nu_0} \tag{5.2}$$

where c is the speed of light, m the paticle's mass, k_B Boltzmann's constant, and ν_0 the transition frequency.

The ion cloud's temperature has been determined using the Doppler cooling laser. While the laser was held at a fixed position, its frequency was scanned and the fluorescence detected with the PMT. The result of this measurement is depicted in figure 5.3. From the Voigt fit a temperature of 1.7(1) mK was determined. This is about three times the Doppler cooling limit which is 0.5 mK. It includes contributions from Doppler broadening and from the finite width of the laser beam in the trap centre [Brewer88]. Further it must be mentioned that the temperature

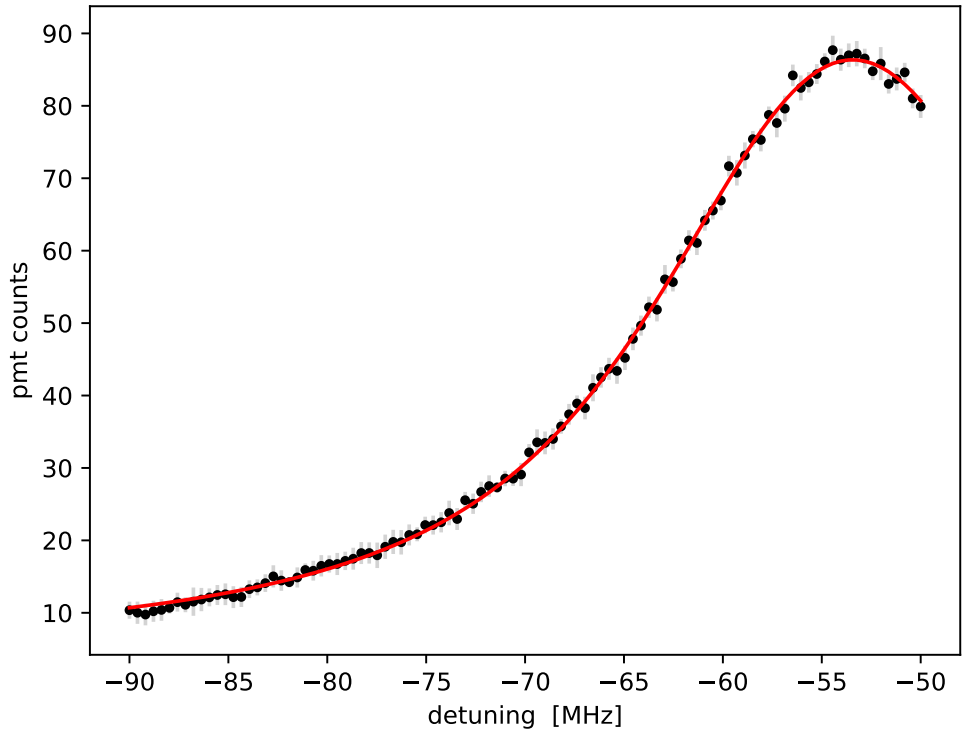

Figure 5.3: Fluorescence signal of a frequency scan of the cooling transition. At each frequency the laser was applied for 15 ms at a power of 49 µW. The detuning is given relative to the theoretically calculated transition frequency. The blue detuned side of the peak was not scanned because scanning is only possible over a range of 40 MHz due to technical limitations. A Voigt profile was fitted to the data resulting in a temperature of 1.7(1) mK.

contains contributions of the axial and the radial temperature. The temperatures might vary for different modes but since the cooling beam travels through the trap centre at an angle of 45° with respect to the magnetic field we cannot distinguish between the contributions of either mode.

A pitfall of the applied method is that we used the same laser for spectroscopy as for cooling. The lowest temperature in Doppler cooling can be reached when the cooling laser is red detuned by $\frac{\Gamma}{2}$ from the cooling transition where Γ is 19.6 MHz for beryllium. However in our measurement the Doppler laser deviates from this ideal point while scanning. We moderate this effect by first cooling the ions at a fixed laser detuning at powers between 0.5 mW and 1.5 mW before scanning the transition at a laser power of 49 µW.

The systematic effects mentioned above could be ruled out by keeping the

cooling laser at a fixed frequency and scanning the $S_{\frac{1}{2}} |m_J = \frac{1}{2}, m_I = \frac{3}{2}\rangle$ $\rightarrow P_{\frac{3}{2}} |m_J = -\frac{1}{2}, m_I = \frac{3}{2}\rangle$ transition with an additional probe laser. Driving the probe transition leads to a decay to the $S_{\frac{1}{2}} |m_J = \frac{1}{2}, m_I = \frac{3}{2}\rangle$ state at probability one third and to the $S_{\frac{1}{2}} |m_J = -\frac{1}{2}, m_I = \frac{3}{2}\rangle$ dark state with probability two thirds, which leads to a decrease in fluorescence of the cooling transition [Jensen04]. However, we had no additional laser available when the temperature was measured. Furthermore, this method is only applicable to ion clouds. Since we aim for single ions, this method would not be useful for us any more as soon as we work at the single ion level. Another method for temperature determination, which is applicable to single ions, would be using sideband spectroscopy [Mavadia14]. However, for beryllium Raman lasers are necessary to implement sideband spectroscopy. The Raman lasers were still under development [Pick20] when these measurements were taken. There are also non-optical methods to determine the ion temperature in a Penning trap [Djekic04] that are not applicable for us since they require a resonant circuit that we do not have in the beryllium trap.

5.3.2. Saturation intensity

Saturation of the cooling transition leads to power broadening of the spectrum and thus to a seemingly higher ion temperature. To exclude saturation effects in our measurements, the ions' fluorescence was determined for different laser powers.

The Doppler cooling transition was driven at different laser power levels at a fixed frequency detuning of −70 MHz and a fixed beam position with respect to the trap centre. For each laser power, photon counts were detected during 20 µs. The diagram (figure 5.4) shows the average of 1000 measurements for the respective power.

As can be seen from the plot, the PMT counts increased linearly with the laser power and no flattening of the curve for raising laser powers could be observed for laser powers up to 729 µW. Since we used a laser power of 49 µW for the temperature determination (figure 5.3), no saturation effects are expected.

It was not possible to determine the actual saturation intensity, as the laser did not provide enough power to see saturation effects in the fluorescence signal.

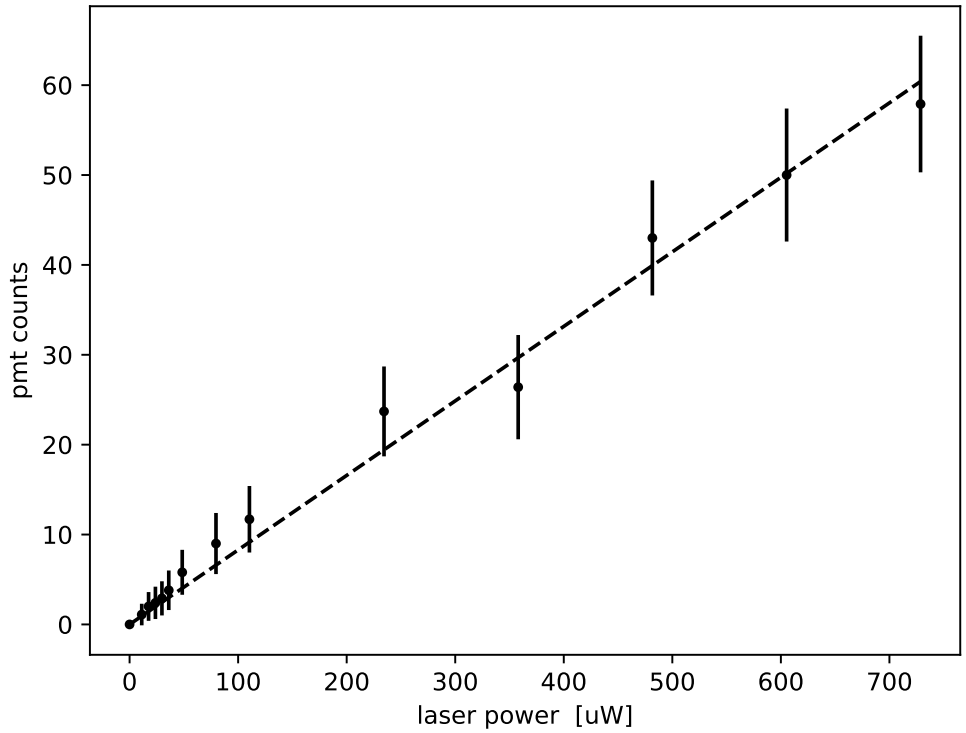

Figure 5.4: Fluorescence with respect to cooling laser power. The laser powers depicted on the x-axis have been measured at the reference point. Each data point represents the average of 1000 meausurements and the respective standard deviation.

5.4. Trap frequencies

Knowing the trap frequencies is crucial for the characterisation of an ion trap. From the trap frequencies the free cyclotron frequency and therefore the magnetic field at the trap centre can be calculated (see section 2.1.1). The free cyclotron frequency must be known in order to apply axialisation (see section 2.2.3). Furthermore the knowledge of the axial frequency is critical for adiabatic ion transport (see chapter 6).

Experimental determination of the axial and modified cyclotron frequencies is carried out as follows. RF pulses with a duration of 32 ms and varying frequency are applied to one of the correction electrodes of the beryllium trap. The smaller the difference between the RF frequency and the trap frequency the higher is the probability that the ions' motion is excited. This behaviour can be compared to a resonantly driven harmonic oscillator. An increased ion motion leads to a

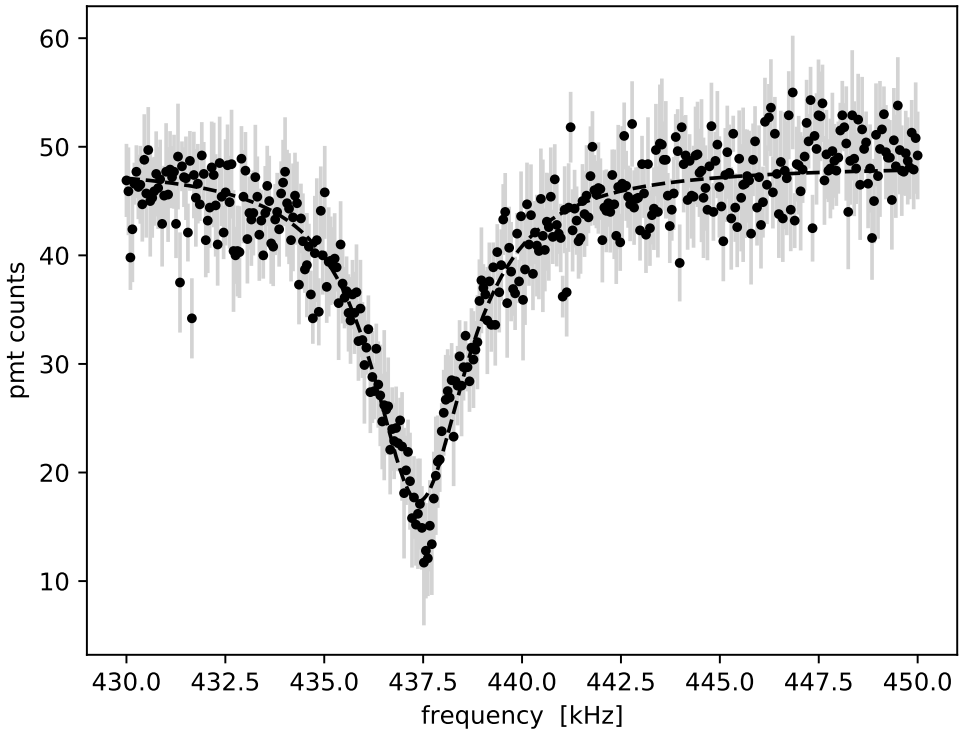

Figure 5.5: Axial trap frequency. Fluorescence signal versus RF frequency for a ring electrode voltage of −20 V. The data shown is an average of ten measurements. The error bars depict the standard error. The dashed line is a Lorentzian curve that was fit to the data as a guide to the eye and to determine the centre of the fluorescence dip. In this case the axial trap frequency is 437.4 kHz.

reduction of the ions' fluorescence signal due to Doppler shift. So after applying the RF pulse, the cooling laser is turned on to detect the ions at the same time as photon readout is performed with the PMT for a duration of 20 µs. After photon counting, the cooling laser is kept on for 15 ms more to recool the ions to their initial temperature in case they were severely heated by the RF. In this manner, a defined RF frequency range is scanned. Although the ions are recooled after each excitation pulse, the order of RF pulses can influence the measurement. If the ion motion was severely excited by one pulse the subsequent measurement might lead to a lower fluorescence level since the ion was not fully recooled to its initial temperature. This effect can become more pronounced if the RF frequency is swept from low to high frequencies or the other way round. This could in the worst case lead to an apparent shift of the trap frequency to a higher or respectively lower frequency. Therefore the measurement is repeated ten times, each time using a different random

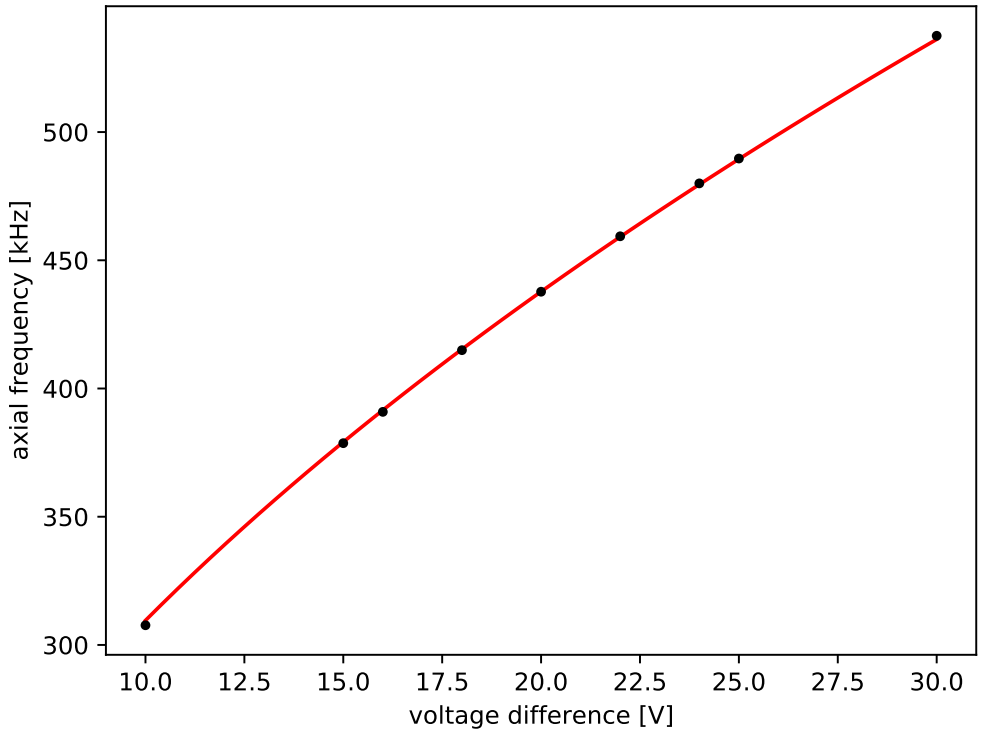

Figure 5.6: Axial trap frequencies as a function of potential depth. The voltage difference denotes the absolute value of the difference between the ring voltage and the endcap voltage. The axial frequencies have been determined using the method described in the text. Error bars are not shown since they are smaller than the spread of the points in the plot. The function for the axial frequency given in equation 5.3 was fitted to the data.

ordering of the RF frequencies being applied. For these measurements relatively high laser powers are applied to ensure fast cooling. It is important to keep the laser power constant during a measurement sequence to maintain the same cooling conditions for every measurement point. However, it is not crucial to use the exact same laser power for different frequency measurements as long as the power is high enough to ensure fast cooling, since the trap frequencies do not depend on laser power. The same is true for the RF power as long as the transition is not saturated.

For the determination of the axial frequency shown in figure 5.5, a laser power of 0.9 mW and an RF power of -55 dBm was used.

The axial frequencies have been measured for different ring voltages between −10 V and −30 V. In figure 5.6 they are depicted as a function of the absolute value

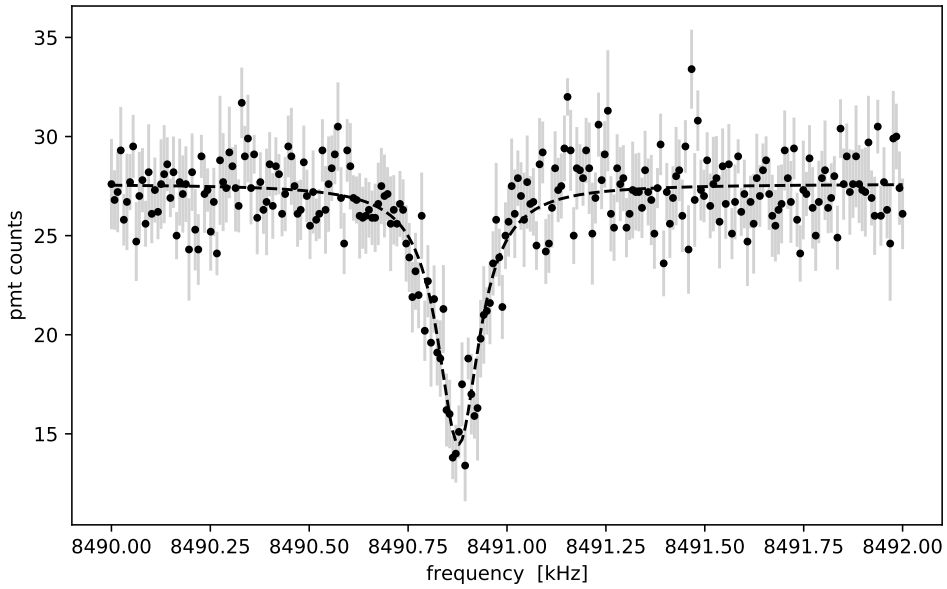

Figure 5.7: Modified cyclotron frequency. Fluorescence signal versus RF frequency for a ring electrode voltage of −20 V. The data shown is an average of ten measurements. The error bars depict the standard error. The dashed line is a Lorentzian curve that was fitted to the data as a guide to the eye and to determine the centre of the fluorescence dip. In this case the modified cyclotron trap frequency is 8490.9 kHz.

of voltage difference between the ring electrode and the endcaps, which were held at 0 V for all the measurements. Equation 5.3 where q and m denote the charge and mass of a beryllium ion, V the voltage difference and C_2 a proportionality constant that depends on the geometry of the trap, was fitted to the data resulting in a C_2 of 17 639 m^{-2} for our beryllium trap.

$$\nu_z = \sqrt{\frac{qV}{2\pi^2 m} C_2} \tag{5.3}$$

The fit is in good agreement with the measured frequencies. That allows to calculate the axial frequency for other ring voltages to a good approximation.

The modified cyclotron frequency for a ring voltage of −20 V was found to be 8490.9 kHz. Together with the axial frequency this leads to a free cyclotron frequency of 8502.2 kHz and a magnetic field of 4.98974 T if one assumes an ideal Penning trap (equations 2.10 and 2.8).

Chapter 6
Towards adiabatic transport of single ions

To determine the spin state of the proton via QLS (see section 1.1) the beryllium ion must be transported from the beryllium trap to the coupling trap and back without heating the axial motional mode, i.e. adiabatically. This is also true for the proof-of-principle aim of sympathetically cooling a beryllium ion by using another co-trapped beryllium ion and coupling their motional modes via Coulomb coupling. To achieve adiabatic transport, the electrode voltages must be changed as a function of time in a way that the harmonic potential, which confines the ion along the axial direction, moves through the trap stack. Therefore the electrode voltages that generate harmonic trapping potentials at any position along the trap stack axis must be known. This is accomplished by calculating the trap voltages for discrete positions and then applying third-order interpolation between the resulting voltages. One then receives smooth voltage waveforms that can be applied to the electrodes.

In section 6.1 the calculation of the electrode voltages is described. Section 6.2 reports on the experimental implementation of transport waveforms and depicts and discusses the results from testing adiabatic transport with ion clouds.

6.1. Transport simulations

For the calculation of the electrode voltages the following assumptions were made:

i The trap stack is perfectly rotationally symmetric with respect to the trap axis.

ii The radial spread of the ion is negligible i.e. the ion is located on the trap axis.

It must be determined which voltages have to be applied to which electrodes to create the desired potentials at the corresponding positions on the trap axis. Electric

potentials can be expressed as a linear combination of other electric potentials. If the electric potential that is caused by an electrode at 1 V is known for every electrode in the stack, the necessary electrode voltages can be determined by solving the linear system of equations $Ax = b$ at each desired position. The $m \times n$ matrix A contains the first m derivatives of the electric potential for n electrodes, x is the solution vector for the n electrode voltages, and b denotes the constraints for the desired potential. Throughout this chapter, the solution vector x is called "voltage vector".

At the centre of a harmonic potential, its first derivative, the electric field, must vanish. The second derivative, the field's curvature, must be $\frac{m}{q}(2\pi\nu_z)^2$ where m and q denote the mass and the charge of the ion and ν_z the axial trap frequency (see section 2.1.1). The third and forth derivative must vanish to avoid anharmonicities. This results in the target vector

$$b = (0, \frac{m}{q}(2\pi\nu_z)^2, 0, 0). \tag{6.1}$$

Determination of the electrode potentials. For the construction of the matrix A the electric potential on the trap axis caused by each electrode at 1 V and their derivatives must be found. This was numerically done with the software Comsol Multiphysics, which uses the finite element method. For the simulation the following simplifications were made:

i The electrodes' geometry was approximated by hollow cylinders.[1]

ii The holes for laser access and the ablation target were neglected.

iii The gold plating was neglected.

iv The proton source was neglected since it is far away from the coupling trap.

The electrodes 1 (endcap of the beryllium trap) to 33 (transition electrode between the two precision traps, see 3.1) were subsequently set to a potential of 1 V while all other electrodes were set to 0 V. In this way the potential caused by each electrode on the trap axis was determined.

The potentials were imported into Wolfram Mathematica where the derivatives were calculated numerically. Further the potentials as well as the derivatives were interpolated using Wolfram Mathematica's built-in interpolation function that fits polynomials to the data for each electrode, resulting in five functions per electrode (one for the potential and one for each of the first four derivatives).

[1] For the two electrodes connecting the coupling trap with an inner diameter of 8 mm with the adjacent traps of 9 mm inner diameter, cylinders with hollow truncated cones were used.

Calculating the voltage vector. Now, we have all ingredients to solve the linear system which reads:

$$\begin{pmatrix} \frac{\partial\phi_1}{\partial z} & \frac{\partial\phi_2}{\partial z} & \cdots & \frac{\partial\phi_n}{\partial z} \\ \frac{\partial^2\phi_1}{\partial z^2} & \frac{\partial^2\phi_2}{\partial z^2} & \cdots & \frac{\partial^2\phi_n}{\partial z^2} \\ \frac{\partial^3\phi_1}{\partial z^3} & \frac{\partial^3\phi_2}{\partial z^3} & \cdots & \frac{\partial^3\phi_n}{\partial z^3} \\ \frac{\partial^4\phi_1}{\partial z^4} & \frac{\partial^4\phi_2}{\partial z^4} & \cdots & \frac{\partial^4\phi_n}{\partial z^4} \end{pmatrix} \begin{pmatrix} x_1 \\ x_2 \\ \cdots \\ x_n \end{pmatrix} = \begin{pmatrix} 0 \\ \frac{m}{q}(2\pi\nu_z)^2 \\ 0 \\ 0 \end{pmatrix} \tag{6.2}$$

where ϕ_n denotes the electric potential of the n-th electrode and x_1 to x_n the voltage vector for the respective electrodes. Since we have more electrodes than constraints, the system of equations is underdetermined. Solving it using the Moore-Penrose inverse of A leads to the voltage vector with the smallest euclidean norm (least squares). This algorithm was chosen, because it leads to smallest possible voltages which is important from an experimental point of view.

Taking time into account. For implementing transport in the experiment, from such voltage vectors we need to build time-dependent waveforms for each electrode that can be applied to the electrodes via the experiment control system. Therefore the positions along the trap axis for which the equation system is solved have been made time-dependent. The function

$$z(t) = \int_0^{\pi} \sin^2(t)dt \tag{6.3}$$

was chosen because the shifting of the potential should start and end smoothly to avoid heating of the ion by a sudden acceleration. For the variable t, a set of discrete times was used.

Waveforms for transport to the coupling trap. For calculating waveforms for the transport of an ion from the centre of electrode 3 (ring electrode of the beryllium trap) to electrode 12 (centre of the coupling trap), electrodes 1 to 23 were taken into account. Figure 6.1 shows the resulting voltages for an axial frequency of 440 kHz. The voltages for electrodes 2 to 8 stand out at around 0.4 ms (see figure 6.1). This is due to the fact that electrodes 5 and 6 are relatively thick with respect to their diameter (see section 3.1). Therefore, compared to the other electrodes, high voltages must be applied to maintain a harmonic potential when the ion passes these electrodes. This effect could be mitigated if several thin electrodes were used instead of one thick electrode. Electrode 7 could be replaced by several thinner electrodes. However, this is not possible for electrode 6 because this endcap electrode contains bores for the cooling laser beam. If replaced by several thinner electrodes laser access would not be possible any more.

The resulting voltages are still discrete values. Continuous waveforms are generated when sending them to the experiment (see 6.2).

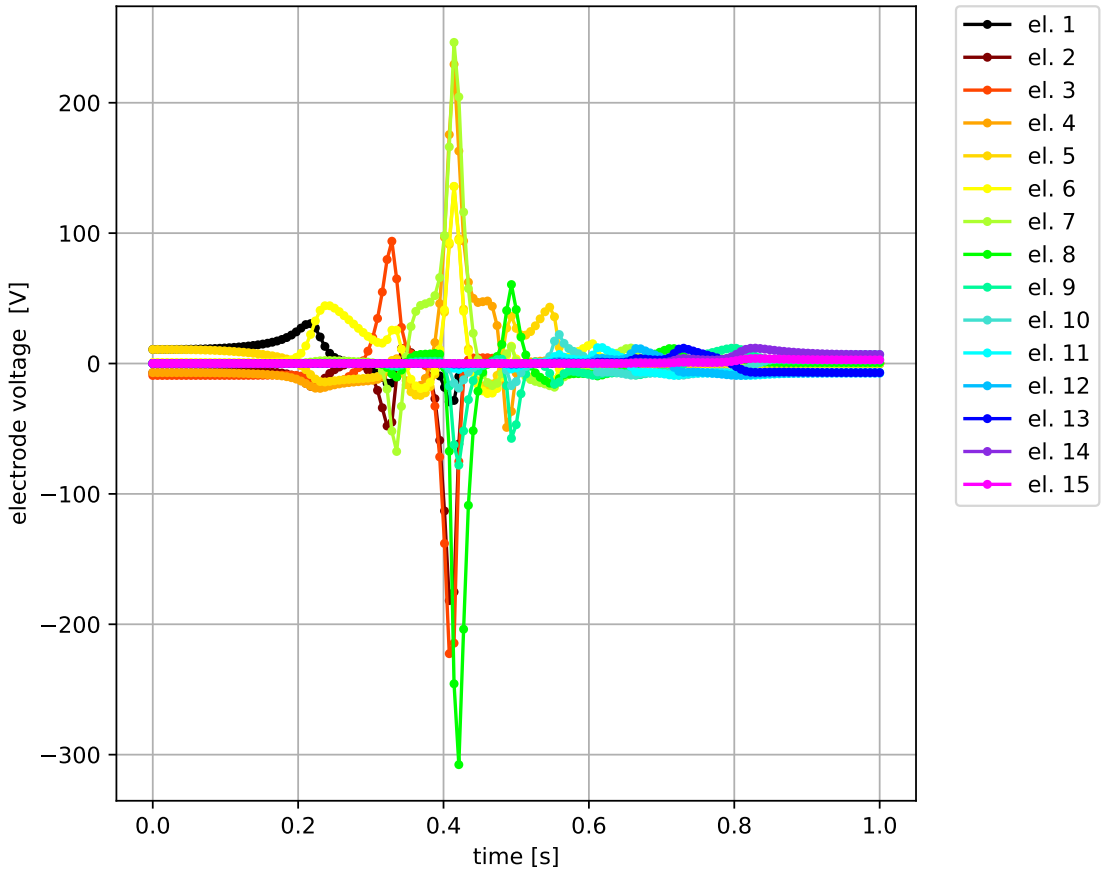

Figure 6.1: Transport waveforms for transport from the beryllium to the coupling trap for a harmonic trap potential. Electrode voltages at discrete times for an axial frequency of 440 kHz. Although electrodes 1 to 23 were used electrodes 16 to 23 are not shown in the plot since their voltages are close to 0 V during the whole transport sequence. The lines serve as a guide to the eye. For details see text.

6.2. Experimental implementation

It would have been desirable to apply the waveforms shown in figure 6.1 to the ion trap, but this was not possible since our current voltage supplies only deliver ±30 V for electrodes 1 to 11 and ±10 V for the remaining electrodes (For details about the voltage sources see section 3.4). So it was necessary to reduce the voltage range of the waveforms. There are two possibilities to achieve this:

i Lower the axial trap frequency.

ii Reduce the number of constraints in equation 6.2.

Both leads to lower electrode voltages. If following the first approach, the axial trap frequency must not exceed 144.8 kHz to succeed with the available voltages.

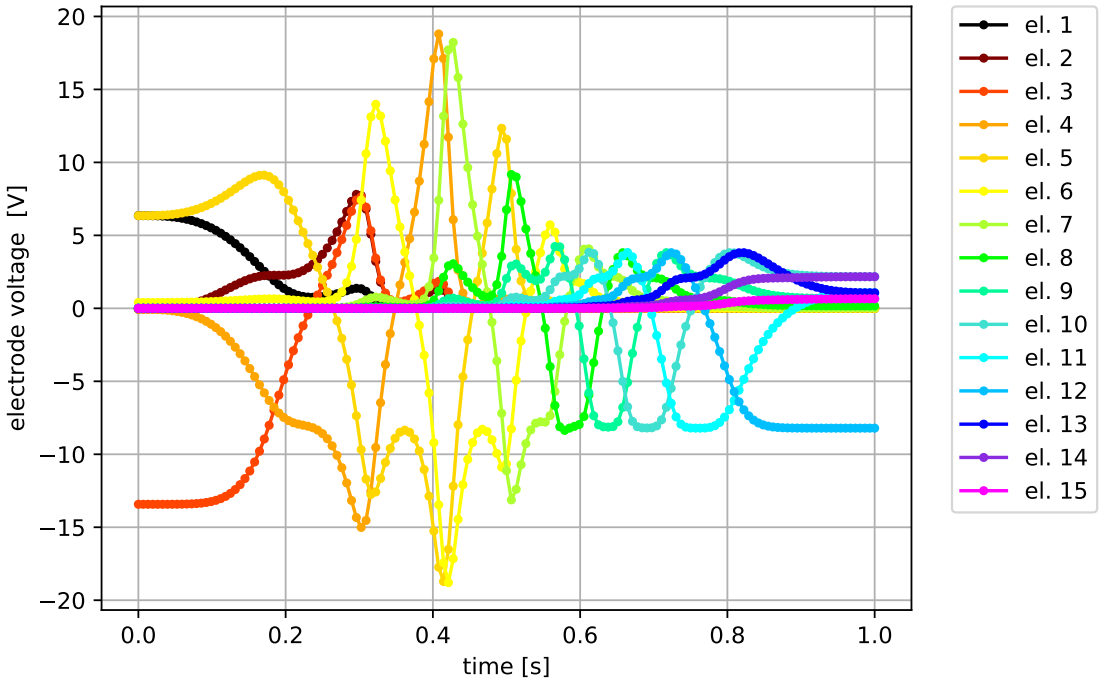

Figure 6.2: Transport waveforms for transport from the beryllium to the coupling trap for a harmonic trap potential dismissing the suppression of trap anharmonicities. Electrode voltages at discrete times for an axial frequency of 440 kHz. Although electrodes 1 to 23 were used electrodes 16 to 23 are not shown in the plot since their voltages are close to 0 V during the whole transport sequence. The lines serve as a guide to the eye.

In our trap this axial frequency corresponds to a magnetron frequency of 1.2 kHz which is lower than or equal to the cutoff frequencies of the low-pass filters in the DC lines (1.3 kHz and 1.2 kHz respectively, for more information on the electronics see section 3.4). Thus the magnetron mode would most probably be heated by electric noise travelling through the filters. So, we followed the second approach and dismissed accounting for trap anharmonicities by reducing the number of constraints from four to two, namely the electric field vanishing and the trap frequency being constant throughout the whole transport sequence. This reduction of constraints leads to the waveforms depicted in figure 6.2 for an axial trap frequency of 440 kHz.

The low-pass filters bear a second risk: The waveforms might be considerably changed due to the filtering. To treat this, one would usually determine the filter functions for each single electrode channel and then calculate new waveforms that account for the filtering. Since our transport sequences have durations on the order of hundreds of milliseconds to seconds and our DC lines a cutoff frequency of 1.3 kHz and 1.2 kHz respectively which corresponds to time constants of 122 µs and 133 µs

repectively, filter functions were not taken into account.

Another experimental restriction is the limited memory of the arbitrary waveform generator (see section 3.4) that produces continuous waveforms from the discrete simulation results. The AWG has a 16 bit resolution and accepts a maximum of 16 or 12 KiB per channel (this number differs for the different channels, for details see [Jördens18]). Therefore, we restricted the number of voltages per electrode for a waveform to 508. This number is not tied to the duration of a waveform. The discrete voltages from the simulation are interpolated with third order b-splines[2]. The resulting interpolation coefficients are handed over to the AWG where the actual waveforms are generated with a resolution of 20 ns.

Before interpolating, the discrete voltages were rounded to the level of 1×10^{-4} V since our AWG has a resolution of 16 bit which correspond to 0.6 mV.

6.2.1. Testing with ions

The transport waveforms could not be tested with a single ion due to the lack of stable fluorescence signals for low ion numbers (see chapter 5). Therefore, a cloud of several ions was used for testing.

Since two constraints were abandoned when calculating the voltages, the resulting potentials do not have a tuning ratio of 0.88 anymore. Therefore the shape of the potential in the beryllium trap has to be carefully changed before transport not to heat the particle by a sudden change of voltages. Furthermore, all electrode voltages need to be increased by a common offset voltage since the voltages for transport are equally distributed around 0 V (to exploit the full range of available voltages) and not $\leq$0 V as is usually the case in our trap. For the ramping for each electrode voltage values between the static trap potential with tuning ratio (TR) 0.88 and the first set of voltages from the transport sequence were calculated such that the voltage changes as

$$\dot{V}(t) \propto \sin^2(t) \tag{6.4}$$

in the range between 0 and π.

The transport sequences that were tested on the ions have a total duration of t_0, consisting of ramping up the potential during $0.3t_0$, moving the potential well along the trap axis to the target position during $0.2t_0$, moving back during $0.2t_0$, and finally ramping the potential down again during $0.3t_0$. Transport was evaluated for durations of $t_0 = 0.7$ s, 1.75 s, and 3.5 s. Transport was either carried out from electrode 3 (ring electrode of the beryllium trap) to electrode 5 and back or from eletrode 3 to electrode 12 (centre of the coupling trap) and back. Transport was evaluated for different axial frequencies: $\nu_z = 308$ kHz, 379 kHz, 440 kHz, 490 kHz and 537 kHz. For all measurements presented in this section, a laser power of 905(2) µW at the pickoff mirror (see 3.3.1) was used.

To evaluate how well the transport works, it is necessary to determine how much the particles were heated during transport, i.e. determine the particles' temperature

[2]The third order was chosen to avoid kinks in the waveform as well as undesired oscillations.

before and after transport and compare them. For a quantitative temperature determination either optical sideband spectroscopy or a resonator for image-charge detection are necessary (for more details on temperature determination see section 5.3.1). While construction of a setup for optical sideband spectroscopy is under way, at the time of this writing the capability was not in place yet. We therefore had to find other measures for evaluating transport in our trap system by only using the Doppler laser. The number of photons detected during fluorescence detection depends on the temperature of the ions. For cold ions many photons are scattered. We use this effect to determine how long it takes to recool the particles after they have been moved through the trap stack by pulsing the cooling laser 3000 times at a fixed detuning of −60 MHz relative to the calculated transition frequency and detecting the fluorescence at the end of each pulse. This method leads to data as exemplarily depicted in figure 6.3. In postprocessing the position of the fluorescence "jump" is determined and used as a relative measure on how much the ions have been heated or respectively how long it takes to recool them. Over the course of this chapter the term "mean cooling duration" is used. It refers to the mean position of the fluorescence jump averaged over several datasets. One could wonder why the cooling laser is not irradiated continuously for recooling the ions. Doing this would lead to fast and efficient recooling such that no difference between different "temperatures" could be observed.

The following experimental sequence was devised:

i Apply Doppler cooling for 1 s.

ii Pulse the Doppler laser 3000 times for 150 µs and read out the PMT for 10 µs at the end each pulse.[3]

iii Turn the laser off for the duration of transport. Apply the transport waveforms while the laser is turned off.

iv Repeat step (ii).

For every set of parameters (transport duration, axial trap frequency, target electrode) the sequence was executed twice: The first time as stated above and the second time without applying waveforms in step (iii). This is for evaluating whether heating during the transport sequence occurs from shaping and moving the trap potential or from the absence of the cooling laser (the measurement cannot distinguish between the latter two cases). In detail step (i) makes sure that the ions are initially cold. Step (ii) is necessary to evaluate whether the fluorescence level for the ions confined in the beryllium trap is stable. If the fluorescence level is unstable this is a hint that either the laser position or power is fluctuating. In this case, the measurement is discarded. Step (iv) produces the data that is actually utilzed to

[3]Using a pulsed readout scheme instead of a continuous one has technical reasons: When the readout pulse was extended an overflow in the experiment control system occured and with that the measurement was automatically aborted.

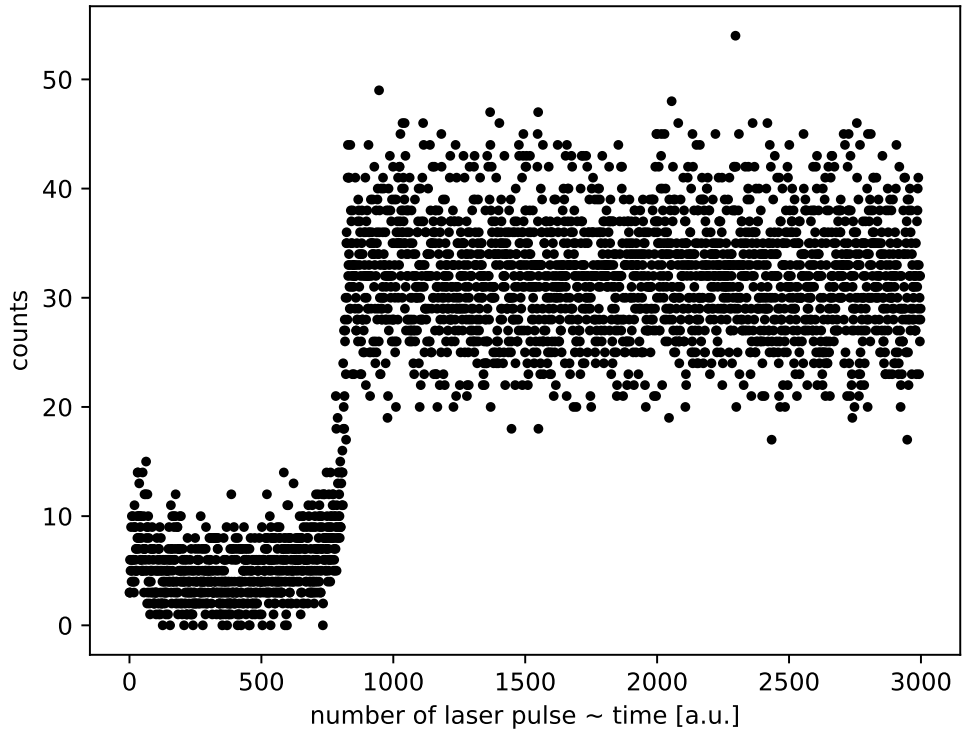

Figure 6.3: Photon counts after transport. The fluorescence level is first low since the ions have been heated. When the ions are recooled it suddenly jumps up. The x-axis is proportional to the elapsed time. For details see text.

evaluate how strongly the ions have been heated. During the whole sequence, the Doppler laser PID ontroller was held in hold mode to allow for fast switching of the AOM while maintaining a constant laser power.

For each set of parameters, between 30 and 150 measurements were taken. From this data the mean cooling duration and its standard error were calculated. In the plots below the mean values are depicted as coloured bars and the standard error as black lines.

To evaluate whether the amount of heating depends on the transport velocity, several waveform durations have been compared for a fixed axial frequency of 379 kHz (figure 6.4). We found a significant amount of heating due to absence of the cooling laser. Furthermore, it can be seen that additional heating during transport occured, which does not show a significant dependence on the transport velocity.

Further it has been evaluated whether heating depends on the axial frequency. Therefore the measurement was repeated for several frequencies, while the transport

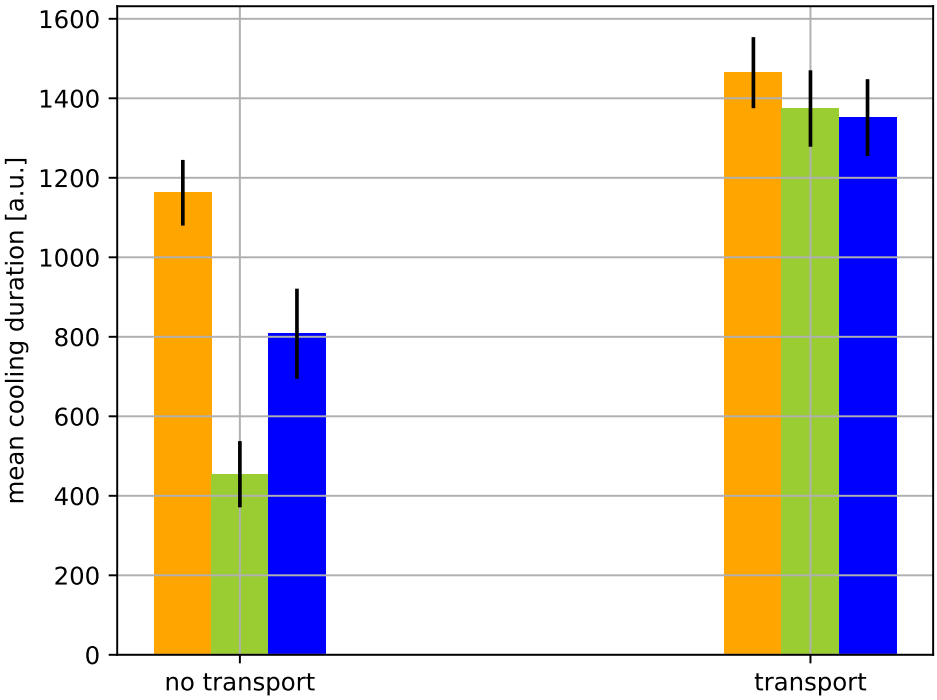

Figure 6.4: Heating for different transport velocities. A trap frequency of 379 kHz was used. Different colours denote different transport durations i.e. different velocities. Orange: duration of 0.7 s, green: 1.75 s, blue: 3.5 s. On the left mean cooling durations after having the laser turned off for the respective transport duration are shown. On the right mean cooling durations after transport are depicted. The black bars represent the standard error. They are only indicative since the data is not normally distributed. It can be seen that the transport velocity has no significant influence on the mean cooling duration.

velocity was kept at a fixed value (figure 6.5). From the data presented, no significant difference in heating could be found for different axial frequencies. But, again, it is obvious that there are heating effects that are not caused by laser-ion-interaction.

Finally, heating for two different transport distances was evaluated, namely transport to electrode 5 (like in the plots above) and transport to electrode 12 in the centre of the coupling trap (figure 6.6). It must be taken into account here that since every waveform consists of 508 voltage values (for details see above) the transport to electrode 12 is not only faster due to the longer distance but also has a lower "resolution" i.e. the potential positions along the trap axis for which the voltage

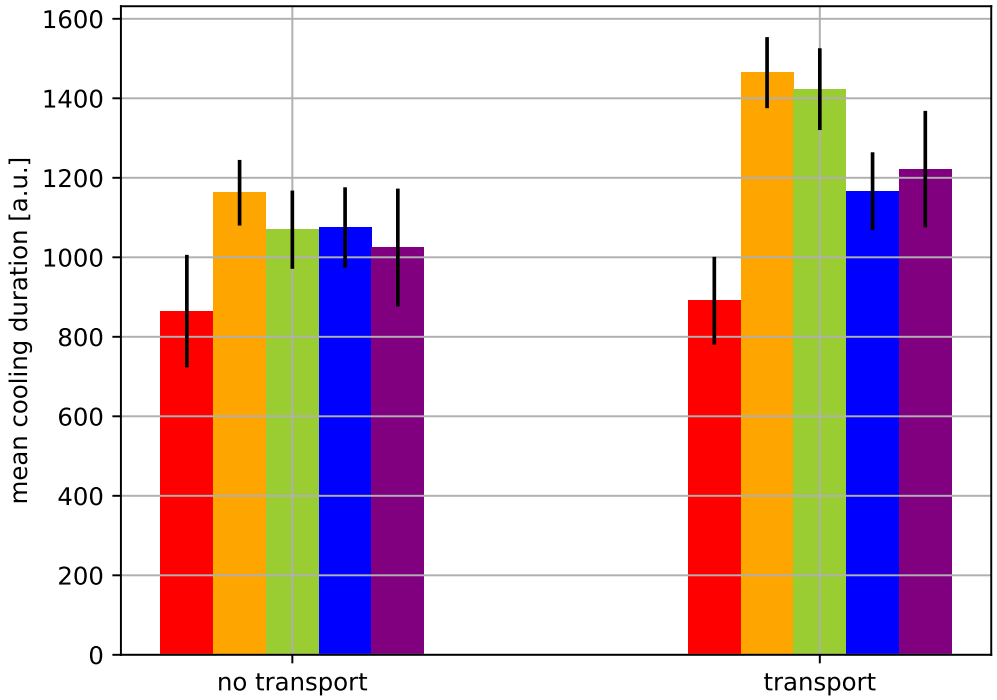

Figure 6.5: Heating for different axial frequencies. A transport duration of 0.7 s was used. Different colours denote different axial frequencies. Red: 308 kHz, orange: 379 kHz, green: 440 kHz, blue: 490 kHz, purple: 537 kHz. On the left mean cooling durations after having the laser turned off for the respective transport duration are shown. On the right mean cooling durations after transport are depicted. The black bars represent the standard error. They are only indicative since the data is not normally distributed. It can be seen that the axial frequency has no significant influence on the mean cooling duration.

vectors have been calculated are further apart from each other than for shorter transport distances. It seems that heating for transport to more distant electrodes does not result in significantly more heating. That indicates that heating that is not associated with laser-ion-interaction probably happens in the beryllium trap whether due to changing the shape of the trapping potential or due to imperfections of the electric field.

Discussion. This chapter presents the prerequisites for adiabatic transport in our Penning trap setup. Electrode voltages and waveforms for adiabatic transport have been derived. The waveforms have been optimised for implementation within the range of the available voltage span of the AWG. The transport waveforms have been

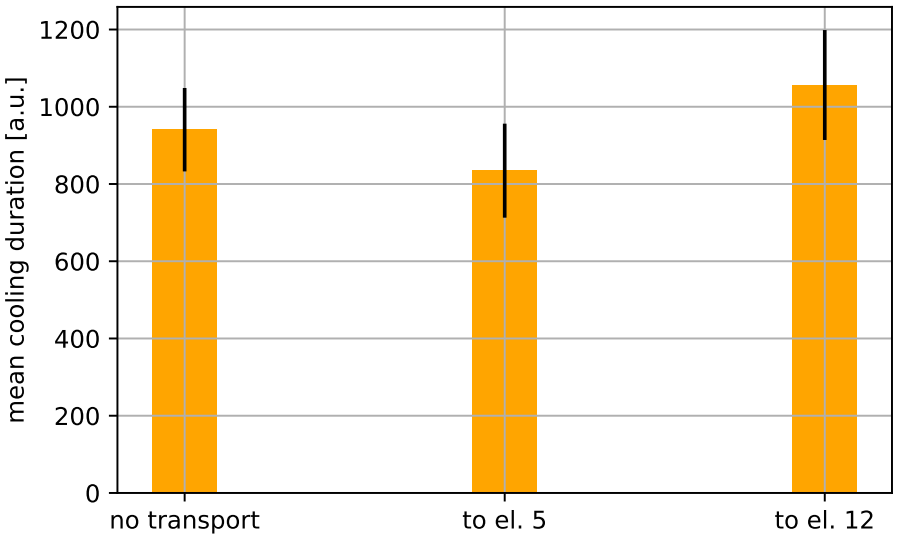

Figure 6.6: Heating for different transport distances. A trap frequency of 440 kHz and a transport duration of 0.7 s was used. The black bars represent the standard error. They are only indicative since the data is not normally distributed. Transport over a larger distance does not lead to significantly more heating. It seems like transport to electrode 5 was cooling, this behaviour is attributed to measurement uncertainties.

implemented in the experiment and successful transport of ion clouds over 29 mm without detectable ion loss has been implemented. A Doppler-recooling approach has been implemented to look for effects of the transport on cloud temperature. It was shown that the recooling approach is able to detect energy gains in the cloud and that at the level of sensitivity of the method, for a wide range of axial frequencies and transport velocities, no influence of transport parameters on the cloud temperature can be observed. The main influence on the cloud temperature seems to originate from the absence of the cooling laser, which indicates that the complicated dynamics of ion clouds have a major impact. This chapter paves the way for measurements with single ions with optical sideband thermometry as the logical next step, once Raman beams and an axial cooling and detection beam become available.

The absence of a connection between relative heating and transport velocity is in good agreement with our expectations: The low-pass filters in the voltage lines set an upper limit to the transport velocity. For fast transport heating could occur due to the voltage waveforms containing frequencies above the low-pass filters' cutoff frequency. Since in our case all evaluated transport velocities are small compared to the cutoff frequency, no difference in heating is expected and no need for taking

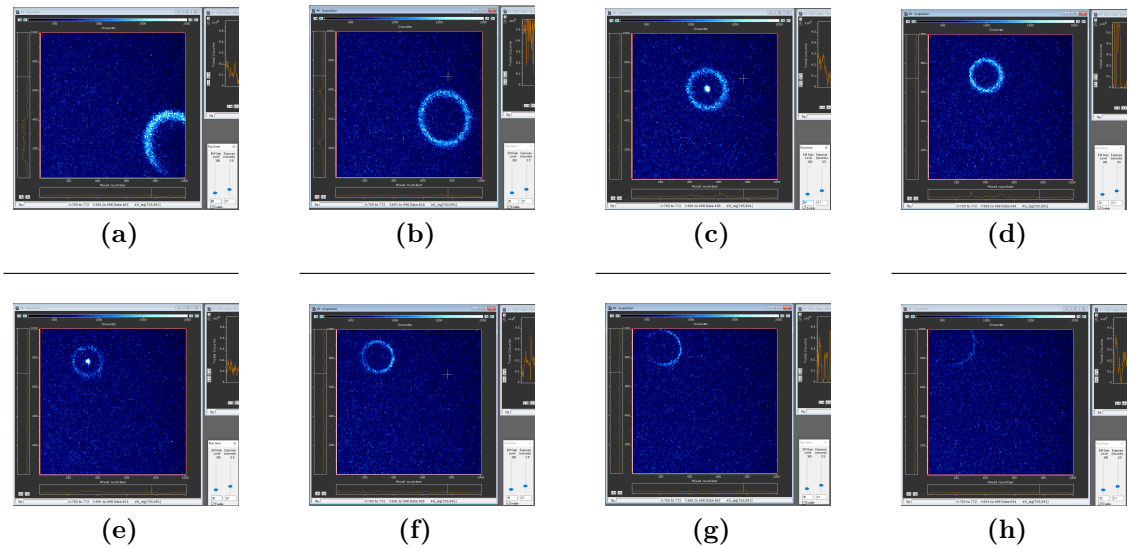

Figure 6.7: Radial position of the ion cloud for different ring voltages. Ring voltages are: 8 V (a), 10 V (b), 15 V (c), 20 V (d), 25 V (e), 30 V (f), 40 V (g), and 60 V (h). The displacement cannot be explained by misalignment of the imaging optics.

filtering into account is given.

In the future the distance of anchor points along the trap axis for which the electrode voltages have been calculated could cause issues since the electrode voltages are interpolated by a third-order b-spline inbetween. That means that the potential is not necessarily harmonic at every position between the anchor points. For a high density of calculated voltages along the trap axis this effect is reduced but due to limited memory of the AWG it might be necessary to store the ion at some intermediate position and move it to the target electrode using a second waveform.

Besides the spatial spread of the ions along the radial direction another effect could cause heating that cannot be explained by laser-ion interaction. There might be disturbances of the electric field affecting the symmetry with respect to the geometric trap axis. This assumption evolves from the fact that when the trap depth is changed the fluorescence image on the EMCCD camera moves radially in a way that cannot be explained by misalignment of the imaging optics (figure 6.7). Furthermore, when RF frequencies that should heat the ions were subsequently applied to the four segments, for one segment no effect in the ion fluorescence could be seen. When the RF amplitudes of these signals were detected with our axial resonator, the amplitude for this one segment was 25 dB lower than for the three other segments. Therefore, we suspect that the cable of one of the four ring electrode segments in the beryllium trap has no proper electric contact with the

segment.

All in all, further investigation is necessary for a quantitative chracterisation of transport in our system. The number of measurements must be increased to receive statistically more meaningful results, the ion number must be reduced to one, the ion must ideally be cooled to its motional ground state, and potential issues concerning wiring of the ring electrode must be solved.

Chapter 7
Conclusion and outlook

In this thesis, a Penning trap system was presented that offers the mechanical prerequisites for ground state cooling of $^9Be^+$ ions using Raman transitions. Furthermore, a coupling trap for motional coupling of two beryllium ions as well as a proton source have been installed. The DC voltages for the trap operation are generated by an AWG that also allows the application of time-varying voltage waveforms for transporting single ions or ion clouds between the individual Penning traps of the trap stack along the trap stack axis. The ions are detected with an imaging system that allows intensity sensitive detection using a PMT as well as spatial resolution in the radial plane using an EMCCD camera.

We have shown reproducible ion loading and particle number reduction in our apparatus. Furthermore, we have implemented trap frequency scan routines. These routines are applicable to a wide range of ion numbers.

Ion clouds can be Doppler cooled to a temperature of 1.7 mK, which is about three times the Doppler limit of 0.5 mK.

Simulations for adiabatic transport have been done and transport of ion clouds to the coupling trap was succesfully demonstrated. A routine for generating voltage waveforms for transport has been developed that is also directly applicable to single ions. These results pave the way for future precision experiments using sympathetic cooling and QLS of single (anti-)protons.

7.1. Outlook

To achieve g-factor measurements using quantum logic spectroscopy (see section 1.1) the following steps are necessary:

Production of single ions with stable fluorescence. For taking the next steps, it is crucial to reproducibly produce single ions with a stable fluorescence signal for detection. With the particle reduction scheme described in section 5.2,

single ions can in principle be achieved. However, we suffer from fluorescence dropouts (see section 5.2). Several measures described in section 7.1.1 will be adopted to mitigate these fluorescence dropouts.

Furthermore, it could be evaluated whether smaller ion numbers can be loaded using a photoionisation laser and a reduced ablation laser power, so the ablation laser produces a neutral beryllium vapour that is subsequently ionised by the photoionisation laser. Besides, the ion number could be reduced by pulsing the endcaps of the beryllium trap to lose particles as has been done in [Goodwin15] as an alternative to dividing the cloud in two parts and ejecting one of them from the trap as is currently done (see section 5.2). Implementing one or both of these concepts could possibly lead to shorter preparation times.

Adiabatic transport of single ions. Transport of ion clouds has been implemented. The method will also be applied to single ions. For this case we expect less heating due to the absence of cloud dynamics. Furthermore, issues concerning the wiring of the electrodes that may cause heating (see section 6.2.1) must be solved. This will involve opening and disassembling the whole apparatus. Several proposals have been made that are described in section 7.1.4.

Sympathetic cooling of single protons. After having implemented adiabatic transport of a single beryllium ion as well as motional coupling of two beryllium ions, sympathetic cooling of a single proton using a single beryllium ion will be implemented. For this, protons must be loaded and a new coupling trap is needed. Preparatory work has been done for both: A proton source was implemented in the current apparatus and needs to be tested. Details on the new coupling trap are described in section 7.1.3.

Ground state cooling of a single $^9Be^+$ ion. Ground state cooling of beryllium ions can be achieved using sideband cooling (see section 2.2.2). For beryllium at a magnetic field of 5 T, this requires Raman beams that bridge the qubit splitting of 140 GHz. Preparatory work has been done by implementing the mirrors needed for sending both Raman beams on different trajectories through the trap centre (see section 3.1) as well as by setting up the Raman laser systems which has been done in the course of a MSc thesis [Pick20]. Those contain a digital phase-locked loop that locks the lasers at an offset frequency of 70 GHz in the infrared. The frequency splitting becomes 140 GHz in the UV due to second harmonic generation [Pick20]. With these ingredients, Raman spectroscopy of the qubit transition will be shown and eventually ground state cooling will be implemented.

Ground state cooling of a single proton. When sympathetic cooling of a single proton as well as ground state cooling of a single beryllium ion have been implemented, ground state cooling of a single proton can be achieved.

Implementation of quantum logic spectroscopy with a single proton and a single $^9Be^+$ ion. Ultimately, QLS can be implemented. This will provide a fast and robust scheme for determining the proton's spin state and therefore facilitate g-factor determinations.

7.1.1. Single ions with stable fluorescence

Several measures will be adopted to mitigate fluorescence dropouts:

- The repumper laser will be implemented to pump back the ion from the $S_{\frac{1}{2}} |m_J = -\frac{1}{2}, m_I = \frac{3}{2}\rangle$ state to the $S_{\frac{1}{2}} |m_J = \frac{1}{2}, m_I = \frac{3}{2}\rangle$ state, which is the lower level of the closed cycle Doppler cooling transition (see section 2.2.4). This will supress fluorescence dropouts caused by the ion decaying to a dark state.

- A beam pointing stabilisation will be set up to reduce heating of the magnetron mode due to beam position instabilities.

- Axialisation (see section 2.2.3) will be applied for coupling the magnetron mode to the modified cyclotron mode. This should reduce the sensitivity of the ion to laser beam positioning fluctuations, since the laser beam position will cause less heating of the magnetron mode.

- An additional laser beam for Doppler cooling will be sent into the system along the trap axis. This additional cooling beam would allow cooling of the axial motional mode without affecting the radial modes, especially without heating the magnetron mode directly. Cooling of all three modes could be achieved by cooling with the cooling beam crossing the trap centre at an angle of 45° and the axial cooling beam in an alternating manner as well as by cooling the magnetron mode via axialisation through the axial mode. More details on the axial cooling beam are given in section 7.1.2

7.1.2. Axial cooling beam

Axial cooling beams are commonly used in Penning traps. Examples can be found in [Mavadia13] and [Ball19]. However, in our experimental setup the axial access is blocked by the proton source or needs to be kept open for antiproton injection on one end and on the other end by the imaging optics (see section 3.1). Therefore, the axial cooling beam will be delivered through the imaging optics as shown in figure 7.1.

In order to achieve that, two challenges must be tackled: First, it must be avoided that reflected light from the axial cooling beam hits the EMCCD camera or the PMT. This would in the best case lower the signal-to-noise ratio of the fluorescence light and in the worst case destroy the devices. Second, the axial cooling beam must be shaped in such a way that it is focused in the trap centre.

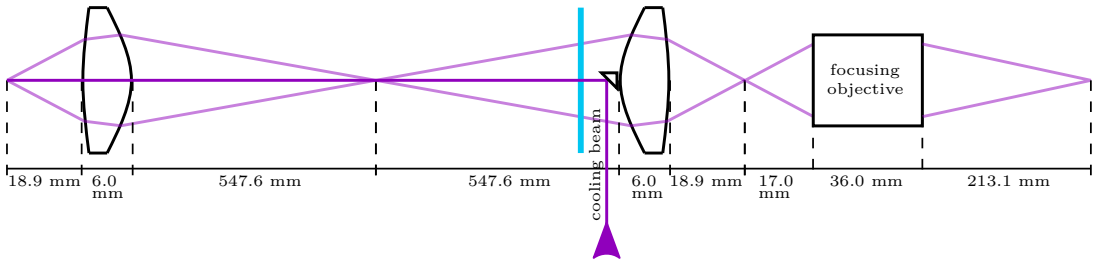

Figure 7.1: Basic concept for introducing a cooling beam through the imaging optics. Not to scale. For details see text.

In the best case the focus size is adjustable to achieve efficient Doppler cooling for different ion cloud sizes.

Preparatory work on the subject has been done in the context of a MSc thesis [Jacobs21]. In the frame of that thesis, different optical components for deflecting the laser beam, namely polarising and non-polarising beam splitters as well as reflective prisms, were evaluated (for the position of the components see figure 7.1). The most promising solution, which was inspired by [Marciniak20], is a prism that is glued onto a fused-silica substrate, which is AR coated to guarantee good transmission of the fluorescence light. A silicon wafer is placed between the prism and the substrate to prevent light that is internally reflected inside the prism from travelling towards the imaging detector. The prism would be placed close to the vacuum window where the diameter of the fluorescence light is maximal to block as little fluorescence light as possible. The laser beam has to pass the vacuum window, which will cause reflections. To avoid them hitting the detectors, a wedged flange reducer was manufactured that deflects reflected light away from the imaging optics. In combination with an axial cooling beam, imaging optics with an intermediate focus to cut possible stray light from the laser beam are favourable such as the system shown in figure 4.3 (a).

The laser beam will be delivered to the imaging platform (see section 3.3) through a fibre. It will be shaped by stock lenses before deflecting it, to achieve a focus in the trap centre. For this, the laser beam must be almost collimated since the aspheric lens attached to the trap stack (see section 3.1) has a short focal length. A perfectly collimated beam would be focused 19.1 mm behind the aspheric lens, i.e. 0.2 mm behind the trap centre (seen from the lens).

7.1.3. Micro coupling trap

For motional coupling of a proton with a beryllium ion the particles need to be brought closely together to achieve a reasonable coupling strength (see section 2.3). Therefore, thin electrodes are needed since the distance between the ions in a double-well potential scales with the electrode thickness. For an inner trap radius of 400 µm and an electrode thickness of 200 µm, the distance between a

beryllium ion in one well and a proton in the other well was calculated to be 300 µm [Smorra15a]. A trap with these dimensions requires a microfabrication process. Therefore, microfabrication techniques have been evaluated in [Fenske19]. Electrode samples have been produced that are currently being examined.

7.1.4. Electrodes

As stated in section 6.2.1, there are strong hints that one of the wires soldered to the individual segments of the ring electrode is broken. Furthermore, some electrode cables broke while assembling the trap stack and copper wires had to be wrapped around these electrodes for DC connection. To solve the issue of breaking cables several alternative methods for connecting the electrodes are currently under investigation:

- An electrode with an integrated soldering tag has been designed. Its machineability is currently investigated.
- As a test, cables have been welded to the electrodes instead of soldering them. Its resilience against thermal cycling and mechanical stress is currently being investigated.
- The electrodes shall either be plated with gold instead of hardgold or the wires shall be coated with removable rubber before plating the electrodes with hardgold, to make the wires less brittle.

7.1.5. Roadmap

The steps described in section 7.1 do not need to be executed in the exact given order. Starting with a single beryllium ion adiabatic transport or ground state cooling can be implemented, since these two steps are independent from each other. The flow chart in figure 7.2 shows the possible orders. Gradual improvement of the measurement speed and accuracy of proton and antiproton g-factor measurements is expected for protons that are sympathetically cooled by beryllium ions at their Doppler limit, protons cooled to their motional ground state, and finally for implementing QLS to transfer the proton's spin state to a beryllium ion. That would greatly reduce the cycle time of the g-factor measurements, allowing for better statistics and the observation of sidereal effects [Cornejo].

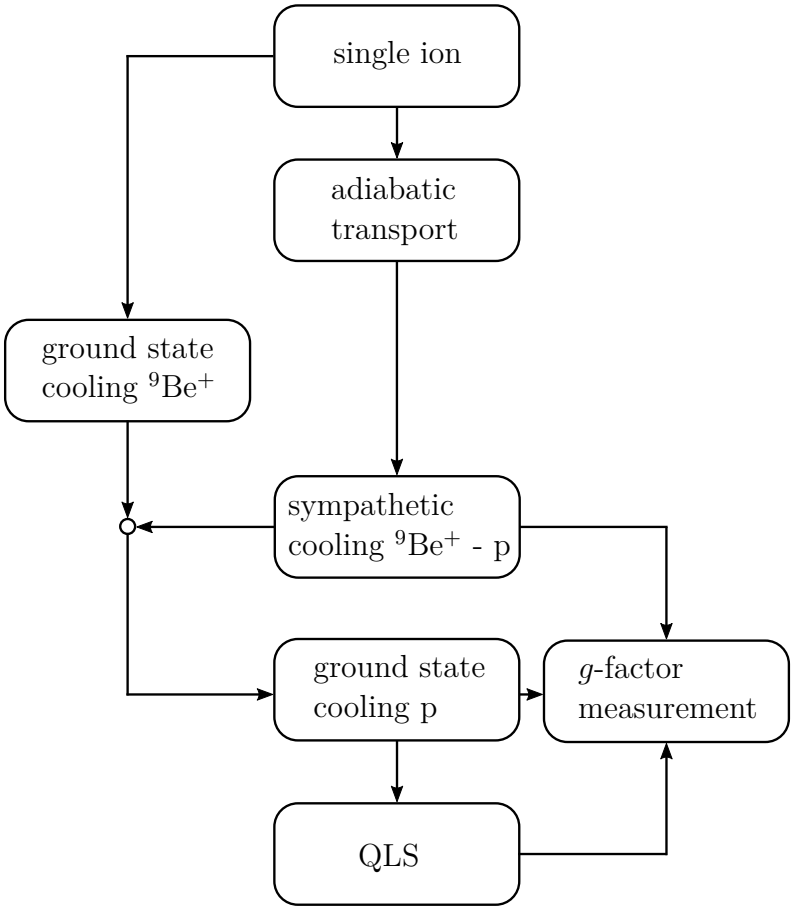

Figure 7.2: Roadmap towards improved g-factor measurements. For details see text.

Appendices

Appendix A

Design of the aspheric lens

The aspheric lens for imaging the ion's fluorescence (see chapter 4) was designed with the help of the optic design software *Zemax12*, which is the predecessor of the software *OpticStudio*, from the company *Zemax*. It is a software for the design, optimisation and tolerancing of imaging and other optical systems. The algorithm behind the programme's standard version, which I used, is sequential ray tracing which is based on geometrical optics. In ray tracing, light is approximated as rays that are traced through an optical system from surface to surface. The details of ray tracing are treated in textbooks e.g. in [Smith08].

In the beginning of the design process, start parameters must be chosen. Those are the wavelength of the light to be used and the shape and position of the light source(s) (collimated beam or point source, radial distance from the optical axis), which are fixed parameters, as well as the position and shape of the optical element(s) i.e. lens parameters such as the radius of curvature and the centre thickness, which can also be set up as variable parameters that are varied in the optimisation process. Some of those paramaters are defined by external constraints, the others need to be guessed.

This first setup is then optimised. Conditions, so called operands, are defined that build the merit function

$$M = \sqrt{\frac{\sum W_i (V_i - T_i)^2}{\sum W_i}}. \tag{A.1}$$

Here, W_i is the weight of the i-th operand, V_i its current value, and T_i its target value [Zemax12]. In the optimisation process, the optimisation algorithm tries to minimise the merit function. The resulting parameters are not necessarily the optimal solution to the problem, since optimisation is a local process that might end in a local minimum of the merit function's parameter space. Therefore, the results from the optimisation process must be examined carefully and the optimisation process must possibly be repeated with different starting values.

Besides fulfilling the boundary conditions, it is important that the optical

R [mm]	k	A_4
54.76751	-40.50485	0
12.34263	-1.065655	3.1180782e-5

Table A.1: Design parameters of the aspheric surfaces. R denotes the radius of curvature, k the conic constant, and A_4 the fourth-order coefficient (see equation A.2) Higher order terms are zero.

system is insensitive to machining tolerances and, possibly, to a misplacement of optical components. To examine how sensitive an optical system is to certain tolerances, a tolerance analysis is performed. It gives evidence on how much the design is affected by predefined tolerances of a certain size. These tolerances can be machining tolerances, e.g. element thickness, centering, and radius of curvature, as well as position tolerances, e.g. a displacement from the optical axis or a tilt of the element. For finding a trade-off between imaging quality and tolerance sensitivity, the tolerance analysis is implemented in the merit function and therefore becomes a part of the optimisation process.

For the design of the aspheric lens, beside *Zemax*' default merit function, operands for the reduction of spherical abberation (SPHA), the y-coordinate of the real ray in the image plane (REAY), the paraxial magnification (PMAG), and the minimum and maximum thickness of the lens (MNCG, MXCG) were taken into account. For the optimisation including tolerances, the thickness (TTHI), tilt (TETX, TETY), and radius (TRAD) of the aspheric lens were taken into account. Furthermore, compensators were used. They allow the system to vary defined parameters in the optimisation process to compensate the effects caused by the tolerances. In this case, compensators were chosen that allow for a change of the distances (COMP) between the optical elements as well as a tilt and decentre (CPAR) of the elements outside the vacuum. A detailed description of the operands' usage can be found in [Zemax12].

The design process was started with spherical surfaces for the lens that should collect the ion's fluorescence light and focus it at a predefined distance. The lens was iteratively optimised and manually reshaped starting from a spheric lens and adding more and more aspheric parameters within the design process roughly following [Smith05]. A second identical aspheric lens was added to the system in reversed orientation as well as a focusing objective (*Thorlabs, LMU-40X-UVB*). After optimising the whole system, a tolerance analysis was performed and the system was optimised again, taking the tolerances into account. After all, the design parameters shown in table A.1 were chosen. They describe the aspheric surfaces given by equation A.2.

$$z(h) = \frac{h^2}{R(1+\sqrt{1-(1+k)\frac{h^2}{R^2}})} + \sum_{i=2}^{n} A_{2i} h^{2i} \tag{A.2}$$

Even though the aspheric lens was designed for use with the *LMU-40X-UBV* focusing objective, which has a magnification of 40, the aspheric lens can also be used with other optical elements. This was finally done, since we aimed for a smaller magnification to allow imaging of a larger area in the radial plane on the EMCCD chip.

List of Figures

List of Tables

Bibliography

[Ball19] **Ball, H., Marciniak, C.D., Wolf, R.N., Hung, A.T.H., Pyka, K., and Biercuk, M.J.** *Site-resolved imaging of beryllium ion crystals in a high-optical-access Penning trap with inbore optomechanics.* Review of Scientific Instruments, **90** (5): 053103 (2019). URL http://dx.doi.org/10.1063/1.5049506. 69

[Bohman18] **Bohman, M., Mooser, A., Schneider, G., Schön, N., Wiesinger, M., Harrington, J., Higuchi, T., Nagahama, H., Smorra, C., Sellner, S., Blaum, K., Matsuda, Y., Quint, W., Walz, J., and Ulmer, S.** *Sympathetic cooling of protons and antiprotons with a common endcap Penning trap.* Journal of Modern Optics, **65** (5-6): 568–576 (2018). URL http://dx.doi.org/10.1080/09500340.2017.1404656. 3

[Bohman20] **Bohman, M.** *Sympathetic Cooling of a Proton with Resonant Image Current Coupling.* PhD thesis, Heidelberg University, Heidelberg (2020). 3

[Borchert17] **Borchert, M.** *Developments for the high precision measurement of the antiproton magnetic moment.* Master's thesis, Leibniz Universität Hannover (2017). 20

[Bowler13] **Bowler, R., Warring, U., Britton, J.W., Sawyer, B.C., and Amini, J.** *Arbitrary waveform generator for quantum information processing with trapped ions.* Review of Scientific Instruments, **84** (3): 033108–033108–6 (2013). URL http://dx.doi.org/doi:10.1063/1.4795552. 26

[Brewer88] **Brewer, L.R., Prestage, J.D., Bollinger, J.J., Itano,**

W.M., Larson, D.J., and Wineland, D.J. *Static properties of a non-neutral $^9Be^+$-ion plasma.* Physical Review A, **38** (2): 859–873 (1988). URL http://dx.doi.org/10.1103/PhysRevA.38.859. 39, 45

[Brown82] **Brown, L.S. and Gabrielse, G.** *Precision spectroscopy of a charged particle in an imperfect Penning trap.* Physical Review A, **25** (4): 2423–2425 (1982). URL http://dx.doi.org/10.1103/PhysRevA.25.2423. 7

[Brown11] **Brown, K.R., Ospelkaus, C., Colombe, Y., Wilson, A.C., Leibfried, D., and Wineland, D.J.** *Coupled quantized mechanical oscillators.* Nature, **471** (7337): 196–199 (2011). URL http://dx.doi.org/10.1038/nature09721. 3, 14

[Cerchiari19] **Cerchiari, G., Yzombard, P., and Kellerbauer, A.** *Laser-Assisted Evaporative Cooling of Anions.* PRL, **123** (103201) (2019). URL http://dx.doi.org/10.1103/PhysRevLett.123.103201. 3

[Christenson64] **Christenson, J.H., Cronin, J.W., Fitch, V.L., and Turlay, R.** *Evidence for the 2π Decay of the $K_2$⁰ Meson.* Physical Review Letters, **13** (4): 138–140 (1964). URL http://dx.doi.org/10.1103/PhysRevLett.13.138. 1

[Cornejo] **Cornejo, J.M., Mielke, J., Meiners, T., Nitzschke, D., Schulte, M., Borchert, M.J., Niemann, M., Bautista-Salvador, A., Lehnert, R., Hammerer, K., Ulmer, S., and Ospelkaus, C.** *Quantum logic inspired techniques for spacetime-symmetry tests with (anti-)protons.* in preparation. 71

[Cornejo16] **Cornejo, J.M., Gutiérrez, M.J., Ruiz, E., Bautista-Salvador, A., Ospelkaus, C., Stahl, S., and Rodríguez, D.** *An optimized geometry for a micro Penning-trap mass spectrometer based on interconnected ions.* International Journal of Mass Spectrometry, **410**: 22–30 (2016). URL http://dx.doi.org/10.1016/j.ijms.2016.10.010. 3

[Cornell90] **Cornell, E.A., Weisskoff, R.M., Boyce, K.R., and Pritchard, D.E.** *Mode coupling in a Penning trap: π pulses and a classical avoided crossing.* Physical Review A,

41 (1): 312–315 (1990). URL http://dx.doi.org/10.1103/PhysRevA.41.312. 12

[Dehmelt73] **Dehmelt, H. and Ekström, P.** *Proposed g-2/$\delta \omega$$_z experiment on stored single electron or positron.* Bull. Am. Phys. Soc., **18**: 727 (1973). 2

[Dehmelt86] **Dehmelt, H.** *Continuous Stern-Gerlach effect: Principle and idealized apparatus.* Proceedings of the National Academy of Sciences of the United States of America, **83** (8): 2291–2294 (1986). URL https://www.ncbi.nlm.nih.gov/pmc/articles/PMC323282/. 2

[Diedrich89] **Diedrich, F., Bergquist, J.C., Itano, W.M., and Wineland, D.J.** *Laser Cooling to the Zero-Point Energy of Motion.* Physical Review Letters, **62** (4): 403 (1989). URL http://dx.doi.org/10.1103/PhysRevLett.62.403. 2

[Djekic04] **Djekic, S., Alonso, J., Kluge, H.J., Quint, W., Stahl, S., Valenzuela, T., Verdú, J., Vogel, M., and Werth, G.** *Temperature measurement of a single ion in a Penning trap.* The European Physical Journal D - Atomic, Molecular, Optical and Plasma Physics, **31** (3): 451–457 (2004). URL http://dx.doi.org/10.1140/epjd/e2004-00168-1. 47

[Earnshaw42] **Earnshaw, S.** *On the nature of the molecular forces which regulate the constitution of the luminiferous ether.* Trans. Camb. Phil. Soc, **7**: 97–112 (1842). URL http://www.citeulike.org/group/744/article/1180343. 5

[Feld15] **Feld, T.** *Ein optischer Aufbau für die Manipulation und Detektion einzelner $^9Be^+$-Ionen für Präzisionsmessungen in kryogenen Penningfallen.* Master's thesis, Leibniz Universität Hannover (2015). 6

[Fenske19] **Fenske, J.A.** *Prozessierung von Komponenten mikro- strukturierter Penning-Ionenfallen.* Master's thesis, Technische Universität Braunschweig, Braunschweig (2019). 71

[Foot05] **Foot, C.J.** *Atomic Physics.* Oxford Master Series in Atomic, Optical and Laser Physics (Oxford University Press, Oxford, 2005). ISBN 0-19-850696-1. 10, 45

[Franzen] **Franzen, A.** *ComponentLibrary*. URL http://www.gwoptics.org/ComponentLibrary/. 25, 29

[Gabrielse83] **Gabrielse, G.** *Relaxation calculation of the electrostatic properties of compensated Penning traps with hyperbolic electrodes*. Phys. Rev. A, **27** (5): 2277 (1983). 8

[Gabrielse89] **Gabrielse, G., Haarsma, L., and Rolston, S.L.** *Open-endcap Penning traps for high precision experiments*. International Journal of Mass Spectrometry and Ion Processes, **88** (2): 319–332 (1989). URL http://dx.doi.org/10.1016/0168-1176(89)85027-X. 8, 10

[Ghosh95] **Ghosh, P.K.** *Ion Traps* (Clarendon, Oxford, UK, Oxford, 1995). 5

[Goodwin15] **Goodwin, J.F.** *Sideband Cooling to the Quantum Ground State in a Penning Trap*. PhD thesis, Imperial College, London (2015). 42, 68

[Goodwin16] **Goodwin, J.F., Stutter, G., Thompson, R., and Segal, D.** *Resolved-Sideband Laser Cooling in a Penning Trap*. Physical Review Letters, **116** (14): 143002 (2016). URL http://dx.doi.org/10.1103/PhysRevLett.116.143002. 2

[Harlander11] **Harlander, M., Lechner, R., Brownnutt, M., Blatt, R., and Hansel, W.** *Trapped-ion antennae for the transmission of quantum information*. Nature, **471** (7337): 200–203 (2011). URL http://dx.doi.org/10.1038/nature09800. 3

[Heinzen90] **Heinzen, D.J. and Wineland, D.J.** *Quantum-limited cooling and detection of radio-frequency oscillations by laser-cooled ions*. Physical Review A, **42** (5): 2977 (1990). URL http://dx.doi.org/10.1103/PhysRevA.42.2977. 3

[Hertel17] **Hertel, I.V. and Schulz, C.P.** *Atome, Moleküle und optische Physik 1* (Springer, 2017), 2nd edition. 31

[Hrmo19] **Hrmo, P., Joshi, M.K., Jarlaud, V., Corfield, O., and Thompson, R.C.** *Sideband cooling of the radial modes of motion of a single ion in a Penning trap*. Physical Review A, **100** (4): 043414 (2019). Publisher: American Physical Society, URL http://dx.doi.org/10.1103/PhysRevA.100.043414. 12

[Idel16] **Idel, A.** *Ein kompaktes Lasersystem zum sympathetischen Kühlen einzelner (Anti-) Protonen durch $^9Be^+$ Ionen.* Master's thesis, Leibniz Universität Hannover, Hannover (2016). 23

[Itano82] **Itano, W.M. and Wineland, D.J.** *Laser cooling of ions stored in harmonic and Penning traps.* Physical Review A, **25** (1): 35–54 (1982). URL http://dx.doi.org/10.1103/PhysRevA.25.35. 11

[Jackson99] **Jackson, J.D.** *Classical electrodynamics* (Wiley, New York, 1999), 3rd ed edition. ISBN 978-0-471-30932-1. 8

[Jacobs21] **Jacobs, F.** *Axiale Laserkühlung und Detektion für eine kryogene Penningfallenapparatur.* Master's thesis, Leibniz Universität Hannover, Hannover (2021). 70

[Jensen04] **Jensen, M.J., Hasegawa, T., and Bollinger, J.J.** *Temperature and heating rate of ion crystals in Penning traps.* Physical Review A, **70** (3): 033401 (2004). URL http://dx.doi.org/10.1103/PhysRevA.70.033401. 47

[Jördens18] **Jördens, R.** *pdq Documentation Release 3.0.dev* (2018). URL https://readthedocs.org/projects/pdq/downloads/pdf/latest/. 58

[Kellerbauer15] **Kellerbauer, A., Cerchiari, G., Jordan, E., and Walter, C.W.** *High-resolution laser spectroscopy on bound-bound transitions in La-.* Phys. Scr., **90** (054014) (2015). URL https://iopscience.iop.org/article/10.1088/0031-8949/90/5/054014/pdf. 3

[Lüders57] **Lüders, G.** *Proof of the TCP theorem.* Annals of Physics, **2** (1): 1–15 (1957). URL http://dx.doi.org/10.1016/0003-4916(57)90032-5. 1

[Lees12] **Lees, J.P., Poireau, V., Tisserand, V., Garra Tico, J., Grauges, E., Palano, A., Eigen, G., Stugu, B., Brown, D.N., Kerth, L.T., Kolomensky, Y.G., Lynch, G., Koch, H., Schroeder, T., Asgeirsson, D.J., Hearty, C., Mattison, T.S., McKenna, J.A., So, R.Y., Khan, A., Blinov, V.E., Buzykaev, A.R., Druzhinin, V.P., Golubev, V.B., Kravchenko, E.A., Onuchin, A.P., Serednyakov, S.I., Skovpen, Y.I., Solodov, E.P., Todyshev, K.Y., Yushkov, A.N., Bondioli, M., Kirkby, D.,**

Lankford, A.J., Mandelkern, M., Atmacan, H., Gary, J.W., Liu, F., Long, O., Vitug, G.M., Campagnari, C., Hong, T.M., Kovalskyi, D., Richman, J.D., West, C.A., Eisner, A.M., Kroseberg, J., Lockman, W.S., Martinez, A.J., Schumm, B.A., Seiden, A., Chao, D.S., Cheng, C.H., Echenard, B., Flood, K.T., Hitlin, D.G., Ongmongkolkul, P., Porter, F.C., Rakitin, A.Y., Andreassen, R., Huard, Z., Meadows, B.T., Sokoloff, M.D., Sun, L., Bloom, P.C., Ford, W.T., Gaz, A., Nauenberg, U., Smith, J.G., Wagner, S.R., Ayad, R., Toki, W.H., Spaan, B., Schubert, K.R., Schwierz, R., Bernard, D., Verderi, M., Clark, P.J., Playfer, S., Bettoni, D., Bozzi, C., Calabrese, R., Cibinetto, G., Fioravanti, E., Garzia, I., Luppi, E., Munerato, M., Piemontese, L., Santoro, V., Baldini-Ferroli, R., Calcaterra, A., de Sangro, R., Finocchiaro, G., Patteri, P., Peruzzi, I.M., Piccolo, M., Rama, M., Zallo, A., Contri, R., Guido, E., Lo Vetere, M., Monge, M.R., Passaggio, S., Patrignani, C., Robutti, E., Bhuyan, B., Prasad, V., Lee, C.L., Morii, M., Edwards, A.J., Adametz, A., Uwer, U., Lacker, H.M., Lueck, T., Dauncey, P.D., Mallik, U., Chen, C., Cochran, J., Meyer, W.T., Prell, S., Rubin, A.E., Gritsan, A.V., Guo, Z.J., Arnaud, N., Davier, M., Derkach, D., Grosdidier, G., Le Diberder, F., Lutz, A.M., Malaescu, B., Roudeau, P., Schune, M.H., Stocchi, A., Wormser, G., Lange, D.J., Wright, D.M., Chavez, C.A., Coleman, J.P., Fry, J.R., Gabathuler, E., Hutchcroft, D.E., Payne, D.J., Touramanis, C., Bevan, A.J., Di Lodovico, F., Sacco, R., Sigamani, M., Cowan, G., Brown, D.N., Davis, C.L., Denig, A.G., Fritsch, M., Gradl, W., Griessinger, K., Hafner, A., Prencipe, E., Barlow, R.J., Jackson, G., Lafferty, G.D., Behn, E., Cenci, R., Hamilton, B., Jawahery, A., Roberts, D.A., Dallapiccola, C., Cowan, R., Dujmic, D., Sciolla, G., Cheaib, R., Lindemann, D., Patel, P.M., Robertson, S.H., Biassoni, P., Neri, N., Palombo, F., Stracka, S., Cremaldi, L., Godang, R., Kroeger, R., Sonnek, P., Summers, D.J., Nguyen, X., Simard, M., Taras, P., De Nardo, G., Monorchio, D., Onorato, G., Sciacca, C., Martinelli, M., Raven, G., Jessop, C.P., LoSecco, J.M., Wang, W.F., Honscheid, K., Kass, R., Brau, J., Frey, R., Sinev, N.B., Strom, D., Torrence, E., Feltresi, E., Gagliardi, N., Margoni, M., Morandin, M., Pompili, A., Posocco,

M., Rotondo, M., Simi, G., Simonetto, F., Stroili, R., Akar, S., Ben-Haim, E., Bomben, M., Bonneaud, G.R., Briand, H., Calderini, G., Chauveau, J., Hamon, O., Leruste, P., Marchiori, G., Ocariz, J., Sitt, S., Biasini, M., Manoni, E., Pacetti, S., Rossi, A., Angelini, C., Batignani, G., Bettarini, S., Carpinelli, M., Casarosa, G., Cervelli, A., Forti, F., Giorgi, M.A., Lusiani, A., Oberhof, B., Paoloni, E., Perez, A., Rizzo, G., Walsh, J.J., Lopes Pegna, D., Olsen, J., Smith, A.J.S., Telnov, A.V., Anulli, F., Faccini, R., Ferrarotto, F., Ferroni, F., Gaspero, M., Li Gioi, L., Mazzoni, M.A., Piredda, G., Bünger, C., Grünberg, O., Hartmann, T., Leddig, T., Schröder, H., Voss, C., Waldi, R., Adye, T., Olaiya, E.O., Wilson, F.F., Emery, S., Hamel de Monchenault, G., Vasseur, G., Yèche, C., Aston, D., Bard, D.J., Bartoldus, R., Benitez, J.F., Cartaro, C., Convery, M.R., Dorfan, J., Dubois-Felsmann, G.P., Dunwoodie, W., Ebert, M., Field, R.C., Franco Sevilla, M., Fulsom, B.G., Gabareen, A.M., Graham, M.T., Grenier, P., Hast, C., Innes, W.R., Kelsey, M.H., Kim, P., Kocian, M.L., Leith, D.W.G.S., Lewis, P., Lindquist, B., Luitz, S., Luth, V., Lynch, H.L., MacFarlane, D.B., Muller, D.R., Neal, H., Nelson, S., Perl, M., Pulliam, T., Ratcliff, B.N., Roodman, A., Salnikov, A.A., Schindler, R.H., Snyder, A., Su, D., Sullivan, M.K., Va'vra, J., Wagner, A.P., Wisniewski, W.J., Wittgen, M., Wright, D.H., Wulsin, H.W., Young, C.C., Ziegler, V., Park, W., Purohit, M.V., White, R.M., Wilson, J.R., Randle-Conde, A., Sekula, S.J., Bellis, M., Burchat, P.R., Miyashita, T.S., Puccio, E.M.T., Alam, M.S., Ernst, J.A., Gorodeisky, R., Guttman, N., Peimer, D.R., Soffer, A., Lund, P., Spanier, S.M., Ritchie, J.L., Ruland, A.M., Schwitters, R.F., Wray, B.C., Izen, J.M., Lou, X.C., Bianchi, F., Gamba, D., Zambito, S., Lanceri, L., Vitale, L., Bernabeu, J., Martinez-Vidal, F., Oyanguren, A., Villanueva-Perez, P., Ahmed, H., Albert, J., Banerjee, S., Bernlochner, F.U., Choi, H.H.F., King, G.J., Kowalewski, R., Lewczuk, M.J., Nugent, I.M., Roney, J.M., Sobie, R.J., Tasneem, N., Gershon, T.J., Harrison, P.F., Latham, T.E., Band, H.R., Dasu, S., Pan, Y., Prepost, R., and Wu, S.L. *Observation of Time-Reversal Violation in the B^0 Meson System.* Physical Review Letters, **109** (21): 211801 (2012). URL http://dx.doi.org/10.1103/PhysRevLett.109.211801. 1

[Marciniak17] **Marciniak, C.D., Ball, H.B., Hung, A.T.H., and Biercuk, M.J.** *Towards fully commercial, UV-compatible fiber patch cords.* Optics Express, **25** (14): 15643–15661 (2017). URL http://dx.doi.org/10.1364/OE.25.015643. 24

[Marciniak20] **Marciniak, C.D.** *Design and operation of a Penning ion trap for quantum simulation.* PhD thesis, The University of Sydney (2020). Accepted: 2020-02-10 Publisher: University of Sydney, URL https://ses.library.usyd.edu.au/handle/2123/21822. 39, 70

[Mavadia13] **Mavadia, S., Goodwin, J.F., Stutter, G., Bharadia, S., Crick, D.R., Segal, D.M., and Thompson, R.C.** *Control of the conformations of ion Coulomb crystals in a Penning trap.* Nature Communications, **4** (2013). URL http://dx.doi.org/10.1038/ncomms3571. 31, 69

[Mavadia14] **Mavadia, S., Stutter, G., Goodwin, J.F., Crick, D.R., Thompson, R.C., and Segal, D.M.** *Optical sideband spectroscopy of a single ion in a Penning trap.* Physical Review A, **89** (3): 032502 (2014). URL http://dx.doi.org/10.1103/PhysRevA.89.032502. 11, 47

[Meiners18] **Meiners, T., Niemann, M., Mielke, J., Borchert, M., Pulido, N., Cornejo, J.M., Ulmer, S., and Ospelkaus, C.** *Towards sympathetic cooling of single (anti-)protons.* Hyperfine Interactions, **239** (1): 26 (2018). URL http://dx.doi.org/10.1007/s10751-018-1502-6. 15

[mLabs] **m Labs**. URL https://m-labs.hk/. 28

[Monroe95] **Monroe, C., Meekhof, D.M., King, B.E., Itano, W.M., and Wineland, D.J.** *Demonstration of a Fundamental Quantum Logic Gate.* Physical Review Letters, **75** (25): 4714–4717 (1995). URL http://dx.doi.org/10.1103/PhysRevLett.75.4714. 4, 11

[Niemann19a] **Niemann, M.** *Design and commissioning of an experiment for sympathetic cooling and coupling of ions in a cryogenic Penning trap.* PhD thesis, Leibniz Universität Hannover, Hannover (2019). 4, 17, 18, 20, 27, 37, 41, 42

[Niemann19b] **Niemann, M., Meiners, T., Mielke, J., Borchert, M.J., Cornejo, J.M., Ulmer, S., and Ospelkaus, C.**

Cryogenic $^9Be^+$ Penning trap for precision measurements with (anti-)protons. Measurement Science and Technology, **31** (3): 035003 (2019). URL http://dx.doi.org/10.1088/1361-6501/ab5722. 18

[Nitzschke20] **Nitzschke, D., Schulte, M., Niemann, M., Cornejo, J.M., Ulmer, S., Lehnert, R., Ospelkaus, C., and Hammerer, K.** *Elementary Laser-Less Quantum Logic Operations with (Anti-)Protons in Penning Traps.* Advanced Quantum Technologies, **9** (11): 1900133 (2020). _eprint: https://onlinelibrary.wiley.com/doi/pdf/10.1002/qute.201900133, URL http://dx.doi.org/10.1002/qute.201900133. 4

[Ospelkaus11] **Ospelkaus, C., Warring, U., Colombe, Y., Brown, K.R., Amini, J.M., Leibfried, D., and Wineland, D.J.** *Microwave quantum logic gates for trapped ions.* Nature, **476** (7359): 181–184 (2011). URL http://dx.doi.org/10.1038/nature10290. 11

[Paschke17] **Paschke, A.G.** *$^9Be^+$ ion qubit control using an optical frequency comb.* PhD thesis, Leibniz Universität Hannover, Hannover (2017). 14

[Pick17] **Pick, J.** *Entwurf einer Quelle zum Laden von Protonen in eine kryogene Penningfalle.* BSc thesis, Leibniz Universität Hannover, Hannover (2017). 20

[Pick20] **Pick, J.** *140 GHz Raman laser system for quantum control in Penning traps.* Master's thesis, Leibniz Universität Hannover, Hannover (2020). 47, 68

[Powell02] **Powell, H.F., Segal, D.M., and Thompson, R.C.** *Axialization of Laser Cooled Magnesium Ions in a Penning Trap.* Physical Review Letters, **89** (9): 093003 (2002). URL http://dx.doi.org/10.1103/PhysRevLett.89.093003. 13

[Pulido19] **Pulido, N.** *A proton source for precision experiments in Penning traps.* Master's thesis, Leibniz Universität Hannover, Hannover (2019). 20

[Quint14] **Quint, W. and Vogel, M.** *Fundamental Physics in Particle Traps* (Springer, 2014). ISBN 978-3-642-45200-0 (Print) 978-3-642-45201-7 (Online). 1, 2

[Schmidt05] **Schmidt, P.O., Rosenband, T., Langer, C., Itano, W.M., Bergquist, J.C., and Wineland, D.J.** *Spectroscopy Using Quantum Logic.* Science, **309** (5735): 749–752 (2005). URL http://dx.doi.org/10.1126/science.1114375. 4

[Schneider14] **Schneider, G.** *Development of a Penning trap system for the high precision measurement of the antiproton's magnetic moment.* Master's thesis, Johannes Gutenberg-Universität, Mainz (2014). 20, 28

[Schneider17] **Schneider, G., Mooser, A., Bohman, M., Schön, N., Harrington, J., Higuchi, T., Nagahama, H., Sellner, S., Smorra, C., Blaum, K., Matsuda, Y., Quint, W., Walz, J., and Ulmer, S.** *Double-trap measurement of the proton magnetic moment at 0.3 parts per billion precision.* Science, **358** (6366): 1081–1084 (2017). URL http://dx.doi.org/10.1126/science.aan0207. 1, 2

[Schwingenheuer95] **Schwingenheuer, B., Briere, R.A., Barker, A.R., Cheu, E., Gibbons, L.K., Harris, D.A., Makoff, G., McFarland, K.S., Roodman, A., Wah, Y.W., Winstein, B., Winston, R., Swallow, E.C., Bock, G.J., Coleman, R., Crisler, M., Enagonio, J., Ford, R., Hsiung, Y.B., Jensen, D.A., Ramberg, E., Tschirhart, R., Yamanaka, T., Collins, E.M., Gollin, G.D., Gu, P., Haas, P., Hogan, W.P., Kim, S.K., Matthews, J.N., Myung, S.S., Schnetzer, S., Somalwar, S.V., Thomson, G.B., and Zou, Y.** *CPT Tests in the Neutral Kaon System.* Physical Review Letters, **74** (22): 4376–4379 (1995). Publisher: American Physical Society, URL http://dx.doi.org/10.1103/PhysRevLett.74.4376. 1

[Segal14] **Segal, D.M. and Wunderlich, C.** *Cooling Techniques for Trapped Ions.* arXiv:1409.6927 [physics, physics:quant-ph], pp. 43–81 (2014). ArXiv: 1409.6927, URL http://dx.doi.org/10.1142/9781783264063_0003. 10

[Sellner17] **Sellner, S., Besirli, M., Bohman, M., Borchert, M.J., Harrington, J., Higuchi, T., Mooser, A., Nagahama, H., Schneider, G., Smorra, C., Tanaka, T., Blaum, K., Matsuda, Y., Ospelkaus, C., Quint, W., Walz, J., Yamazaki, Y., and Ulmer, S.** *Improved limit on the directly measured antiproton lifetime.* New Journal of Physics,

19 (8): 083023 (2017). URL http://dx.doi.org/10.1088/1367-2630/aa7e73. 1, 21

[Smith05] **Smith, W.J.** *Modern Lens Design* (McGraw-Hill, 2005), second edition. 76

[Smith08] **Smith, W.J.** *Modern optical engineering : the design of optical systems*, volume 180 of *SPIE PM* (McGraw-Hill, New York, NY, Chicago, San Francisco, 2008), 4th edition. ISBN 0-07-147687-3 978-0-07-147687-4. 75

[Smorra15a] **Smorra, C., Blaum, K., Bojtar, L., Borchert, M., Franke, K., Higuchi, T., Leefer, N., Nagahama, H., Matsuda, Y., Mooser, A., Niemann, M., Ospelkaus, C., Quint, W., Schneider, G., Sellner, S., Tanaka, T., Van Gorp, S., Walz, J., Yamazaki, Y., and Ulmer, S.** *BASE – The Baryon Antibaryon Symmetry Experiment.* The European Physical Journal Special Topics, **224** (16): 3055 (2015). URL http://dx.doi.org/10.1140/epjst/e2015-02607-4. 2, 71

[Smorra15b] **Smorra, C., Mooser, A., Franke, K., Nagahama, H., Schneider, G., Higuchi, T., Gorp, S.V., Blaum, K., Matsuda, Y., Quint, W., Walz, J., Yamazaki, Y., and Ulmer, S.** *A reservoir trap for antiprotons.* International Journal of Mass Spectrometry, **389**: 10–13 (2015). URL http://dx.doi.org/10.1016/j.ijms.2015.08.007. 20, 42

[Smorra18] **Smorra, C., Blessing, P.E., Borchert, M.J., Devlin, J.A., Harrington, J.A., Higuchi, T., Morgner, J., Nagahama, H., Sellner, S., Bohman, M.A., Mooser, A.H., Schneider, G.L., Schön, N., Wiesinger, M., Blaum, K., Matsuda, Y., Ospelkaus, C., Quint, W., Walz, J., Yamazaki, Y., and Ulmer, S.** *350-fold improved measurement of the antiproton magnetic moment using a multi-trap method.* Hyperfine Interactions, **239** (1): 47 (2018). URL http://dx.doi.org/10.1007/s10751-018-1507-1. 2

[Ulmer11] **Ulmer, S.** *First Observation of Spin Flips with a Single Proton Stored in a Cryogenic Penning Trap.* PhD thesis, Universität Heidelberg, Heidelberg (2011). URL http://www.ub.uni-heidelberg.de/archiv/12306/. 8, 21

[Ulmer14] **Ulmer, S., Mooser, A., Blaum, K., Braeuninger, S.,**

Franke, K., Kracke, H., Leiteritz, C., Matsuda, Y., Nagahama, H., Ospelkaus, C., Rodegheri, C.C., Quint, W., Schneider, G., Smorra, C., Gorp, S.V., Walz, J., and Yamazaki, Y. *The magnetic moments of the proton and the antiproton.* Journal of Physics: Conference Series, **488** (1): 012033 (2014). URL http://dx.doi.org/10.1088/1742-6596/488/1/012033. 2

[Ulmer15] **Ulmer, S., Smorra, C., Mooser, A., Franke, K., Nagahama, H., Schneider, G., Higuchi, T., Van Gorp, S., Blaum, K., Matsuda, Y., Quint, W., Walz, J., and Yamazaki, Y.** *High-precision comparison of the antiproton-to-proton charge-to-mass ratio.* Nature, **524** (7564): 196–199 (2015). URL http://dx.doi.org/10.1038/nature14861. 1

[Van Dyck76] **Van Dyck, R.S., Wineland, D.J., Ekstrom, P., and Dehmelt, H.G.** *High mass resolution with a new variable-anharmonicity Penning trap.* Appl. Phys. Lett., (28): 446 (1976). 8

[Van Dyck87] **Van Dyck, R.S., Schwinberg, P.B., and Dehmelt, H.G.** *New high-precision comparison of electron and positron g factors.* Physical Review Letters, **59** (1): 26–29 (1987). URL http://dx.doi.org/10.1103/PhysRevLett.59.26. 1

[Wahnschaffe16] **Wahnschaffe, M.** *Engineered microwave control for trapped ions.* PhD thesis, Leibniz Universität Hannover, Hannover (2016). 39

[Wineland73] **Wineland, D., Ekstrom, P., and Dehmelt, H.** *Monoelectron Oscillator.* Physical Review Letters, **31** (21): 1279–1282 (1973). URL http://dx.doi.org/10.1103/PhysRevLett.31.1279. 2

[Wineland75] **Wineland, D. and Dehmelt, H.** *Line shifts and widths of axial, cyclotron and G-2 resonances in tailored, stored electron (ion) cloud.* International Journal of Mass Spectrometry and Ion Physics, **16** (3): 338–342 (1975). URL http://dx.doi.org/10.1016/0020-7381(75)87031-8. 12

[Wineland79] **Wineland, D.J. and Itano, W.M.** *Laser cooling of atoms.* Physical Review A, **20** (4): 1521–1540 (1979). URL http://dx.doi.org/10.1103/PhysRevA.20.1521. 10, 12

[Wineland98] **Wineland, D., Monroe, C., Itano, W., Leibfried, D., King, B., and Meekhof, D.** *Experimental issues in coherent quantum-state manipulation of trapped atomic ions.* Journal of Research of the National Institute of Standards and Technology, **103** (3): 259 (1998). URL http://dx.doi.org/10.6028/jres.103.019. 3

[Wu57] **Wu, C.S., Ambler, E., Hayward, R.W., Hoppes, D.D., and Hudson, R.P.** *Experimental Test of Parity Conservation in Beta Decay.* Physical Review, **105** (4): 1413 (1957). URL http://dx.doi.org/10.1103/PhysRev.105.1413. 1

[Zemax12] **Zemax**. *Zemax 12 Optical Design Program User's Manual* (2012). 75, 76

Acknowledgements

I would like to express my thanks to those who made this thesis possible and to those who accompanied and supported me during the last years.

Christian Ospelkaus for bringing the project into life and for supervising my thesis. I appreciate the freedom you gave me and that you always had time when problems occured or discussions were necessary.

Piet Schmidt for acting as a referee for this thesis, *Richard Thompson* for examining this thesis, and *Klemens Hammerer* for chairing my defence.

Stefan Ulmer, Matthias Borchert, Richard Thompson, Oliver Corfield, and *Christian Marciniak* who did not hesitate to help and give advice when questions and problems occured and from whom I learned a lot.

Jonas Peter, Alexander Vocino und *Emil Adamczyk* stellvertretend für das Team der Feinmechanikwerkstatt des IQ, die immer wieder Teile in weniger als keiner Zeit gefertigt und schneller als schnell modifiziert haben. *Herrn Metschke* und *Herrn Mai* stellvertretend für die Feinmechanikwerkstatt der PTB für die Fertigung der Falle und der kalten Stufe sowie *Herrn Engelke* stellvertretend für die Galvanik der PTB für die Vergoldung unserer Fallenelektroden.

Gunhild Faber, Elke Hünitzsch, Stephanie Kaisik, Madeleine Miltsch und *Birgit Ohlendorf* stellvertretend für die Sekretariate, die für jedes noch so bürokratische Problem eine Lösung gefunden haben.

A big thanks goes to my QLEDS mates *Juanma Cornejo, Johannes Mielke,* and *Malte Niemann*. Without you it would not have been possible to start and run this experiment. I also want to thank *Julia Coenders*. Even though the time we spent together at the experiment was short, you helped a lot asking the right questions and digging through the Artiq documentation with us.

My thanks also go to all former and current members of Christian Ospelkaus' group. It was a pleasure working and discussing with you. Special thanks go to *Timko Dubielzig* for providing endless amounts of peppermint chocolate and random stories, to *Sebastian Halama* for answering every question about electronics that I ever had, and to *Malte Niemann* for patiently explaining the experiment concept to me when I started to work with you and for letting me have the LaTeX template when I finished to work with you.

POMOs, *SLOMOs*, and *Erik, Wuying, and Julia* for discussions, advice, stuff from the *Horst-Keller*, and many enjoyable lunch breaks. Special thanks go to *Kai Voges* for the dinosaur.

Christian Meiners and *Malte Niemann* (again) for proof-reading and commenting this thesis.

Besonders möchte ich meinen Freunden für den Ausgleich zur Arbeit danken und meiner Familie für all die Unterstützung und die häufige Kinderbetreuung in den letzten Wochen.